NATIONAL TECHNICAL UNIVERSITY OF ATHENS

SCHOOL OF ELECTRICAL AND COMPUTER ENGINEERING

DIVISION OF COMMUNICATION, ELECTRONIC AND

AND INFORMATION ENGINEERING

Development of PLA-based triboelectric nanogenerators for harvesting the mechanical energy of the environment

DIPLOMA THESIS

of

Stefania Skorda

Academic Supervisor: Evangelos V. Hristoforou

Professor NTUA

Research Supervisor: Christos Tsamis

Director of Research NCSR “Demokritos”

Athens, March, 2024

NATIONAL TECHNICAL UNIVERSITY OF ATHENS

SCHOOL OF ELECTRICAL AND COMPUTER ENGINEERING

DIVISION OF COMMUNICATION, ELECTRONIC AND INFORMATION ENGINEERING

Development of PLA-based triboelectric nanogenerators for harvesting the mechanical energy of the environment

DIPLOMA THESIS

of

Stefania Skorda

Academic Supervisor: Evangelos V. Hristoforou

Professor NTUA

Research Supervisor: Christos Tsamis

Research Director NCSR “Demokritos”

Approved by the Examining Committee on the 29th of March, 2024.

.....	.....	.....
Evangelos V. Hristoforou	Christos Tsamis	Emmanouel Hourdakis
Professor NTUA	Director of Research NCSR “Demokritos”	Assistant Professor NTUA

Athens, March, 2024

.....

Στεφανία Σκόρδα

Διπλωματούχος Ηλεκτρολόγος Μηχανικός και Μηχανικός Υπολογιστών, Ε.Μ.Π.

Copyright © All rights reserved. Με επιφύλαξη παντός δικαιώματος.

Στεφανία Σκόρδα, 2024.

Απαγορεύεται η αντιγραφή, αποθήκευση και διανομή της παρούσας εργασίας, εξ' ολοκλήρου ή τμήματος αυτής, για εμπορικό σκοπό. Επιτρέπεται η ανατύπωση, αποθήκευση και διανομή για σκοπό μη κερδοσκοπικό, εκπαιδευτικής ή ερευνητικής φύσης, υπό την προϋπόθεση να αναφέρεται η πηγή προέλευσης και να διατηρείται το παρόν μήνυμα. Ερωτήματα που αφορούν τη χρήση της εργασίας για κερδοσκοπικό σκοπό πρέπει να απευθύνονται προς τον συγγραφέα.

Οι απόψεις και τα συμπεράσματα που περιέχονται σε αυτό το έγγραφο εκφράζουν τον συγγραφέα και δεν πρέπει να ερμηνευθεί ότι αντιπροσωπεύουν τις επίσημες θέσεις του Εθνικού Μετσόβιου Πολυτεχνείου.

στην οικογένειά μου

Περίληψη

Η παρούσα διπλωματική εργασία παρουσιάζει μια διεξοδική έρευνα για την ανάπτυξη τριβοηλεκτρικών γεννητριών, οι οποίες είναι διατάξεις που μετατρέπουν την μηχανική ενέργεια από το περιβάλλον σε ηλεκτρική ενέργεια, χρησιμοποιώντας σύνθετα υλικά όπως το πολυγαλακτικό οξύ (PLA) με πρόσμιξη οξειδίου του ψευδαργύρου (ZnO) και καρβιδίου του πυριτίου (SiC). Το PLA είναι ένας βιώσιμος, βιοδιασπώμενος θερμοπλαστικός πολυεστέρας που παράγεται από ανανεώσιμες πηγές, όπως το άμυλο καλαμποκιού ή το ζαχαροκάλαμο, και χρησιμοποιείται ευρέως στην τρισδιάστατη εκτύπωση FDM (Fused Deposition Modeling) λόγω του ελάχιστου περιβαλλοντικού αποτυπώματος και των πλεονεκτικών μηχανικών χαρακτηριστικών του. Η προσθήκη νανοσωματιδίων όπως το ZnO και το SiC στο PLA μελετάται για την ικανότητά τους να βελτιώσουν αυτές τις εγγενείς ιδιότητες και να ενισχύσουν σημαντικά την τριβοηλεκτρική απόδοση των νανογεννητριών με βάση το PLA. Η επιλογή του SiC ως προσθετικού υλικού βασίζεται στην αξιοσημείωτη σκληρότητά του και την ικανότητά του να ενισχύει τα μηχανικά χαρακτηριστικά του σύνθετου υλικού, ενώ το ZnO ενσωματώνεται για τα πολυλειτουργικά του οφέλη, συμπεριλαμβανομένης της θωράκισης από την υπεριώδη ακτινοβολία, των αντιμικροβιακών επιδράσεων και της ενισχυμένης θερμικής αγωγιμότητας. Η παρούσα μελέτη παρέχει μια ολοκληρωμένη ανάλυση των μηχανικών και ηλεκτρικών ιδιοτήτων των σύνθετων υλικών PLA με πρόσμιξη SiC και ZnO, προσφέροντας γνώσεις σχετικά με τις δυνατότητες αυτών των υλικών στην ενίσχυση της απόδοσης των τριβοηλεκτρικών γεννητριών για εφαρμογές συλλογής περιβαλλοντικής ενέργειας.

Λέξεις-κλειδιά

Τριβογεννήτριες, Συλλογή Ενέργειας, Πολυγαλακτικό Οξύ(PLA), Οξείδιο του Ψευδαργύρου (ZnO), Καρβίδιο του Πυριτίου (SiC), Τρισδιάστατη Εκτύπωση, Μηχανικές Ιδιότητες, Διηλεκτρική Σταθερά

Abstract

This thesis presents an in-depth investigation into the development of triboelectric generators, which are devices that convert mechanical energy from the environment into electrical energy, using Polylactic Acid (PLA) composites doped with Zinc Oxide (ZnO) and Silicon Carbide (SiC). PLA is a sustainable, biodegradable thermoplastic polyester made from renewable resources like corn starch or sugarcane, and it is extensively utilized in Fused Deposition Modeling (FDM) 3D printing for its minimal environmental footprint and advantageous mechanical characteristics. The strategic addition of nanofillers such as ZnO and SiC to PLA is studied for their ability to fine-tune these inherent properties and significantly boost the triboelectric output of PLA-based nanogenerators. The choice of SiC as a dopant is based on its remarkable hardness and ability to reinforce the mechanical attributes of the composite, while ZnO is incorporated for its multifunctional benefits, including UV shielding, antimicrobial effects, and enhanced thermal conductivity. This study provides a comprehensive analysis of the mechanical and electrical properties of PLA composites doped with SiC and ZnO, offering insights into the potential of these materials in enhancing the efficiency of triboelectric generators for environmental energy harvesting applications.

Keywords

Tribogenerators, Energy harvesting, Polylactic Acid (PLA), Zinc Oxide (ZnO), Silicon Carbide (SiC), 3D printing, Mechanical Properties, Dielectric Constant

Ευχαριστίες

Αρχικά, θα ήθελα να ευχαριστήσω θερμά τον Καθηγητή Ευάγγελο Χριστοφόρου και τον Διευθυντή Ερευνών του Ινστιτούτου Νανοεπιστήμης και Νανοτεχνολογίας (ΙΝΝ), ΕΚΕΦΕ «Δημόκριτος» Χρήστο Τσάμη, που μου έδωσαν την ευκαιρία να εκπονήσω την Διπλωματική μου εργασία στο Εργαστήριο Συλλογής Ενέργειας και Αυτόνομων Αισθητήρων του ΕΚΕΦΕ «Δημόκριτος» υπό την επίβλεψή τους. Χάρη στην καθοδήγησή και την εμπειρία του κου Τσάμη, δημιουργήθηκε ένα καινοτόμο ερευνητικό θέμα το οποίο συνέβαλε στην προσωπική μου και επιστημονική μου εξέλιξη. Οι χρήσιμες συμβουλές του αποτέλεσαν αρωγό για την ολοκλήρωση της παρούσας εργασίας.

Θα ήθελα να ευχαριστήσω επίσης μέσα από την καρδιά μου τον Διευθυντή Ερευνών του ΕΚΕΦΕ «Δημόκριτος» Γεώργιο Βεκίνη για την πολύτιμη βοήθειά του στην Διπλωματική μου εργασία. Κατά τη διάρκεια της συνεργασίας μας, μου μετέδωσε ένα μικρό κομμάτι από τις επιστημονικές και τεχνικές του γνώσεις, ενώ παράλληλα μου παρείχε ανεκτίμητη υποστήριξη. Ο κος Βεκίνης μαζί με τα υπόλοιπα μέλη του εργαστηρίου, αξίζουν ένα ιδιαίτερο ευχαριστώ που με φιλοξένησαν στο χώρο εργασίας τους, στο Εργαστήριο Προηγμένων Κεραμικών και Σύνθετων Υλικών του ΙΝΝ.

Επιπλέον, οφείλω ένα θερμό ευχαριστώ στον Επίκουρο Καθηγητή Εμμανουήλ Χουρδάκη και στον Δρ. Αχιλλέα Μπαρδάκα για την παραγωγική και ευχάριστη συνεργασία μας καθώς και για την βοήθεια να εξοικειωθώ με εργαστηριακές τεχνικές. Επίσης, ευχαριστώ τους προπτυχιακούς και μεταπτυχιακούς φοιτητές του ΙΝΝ που περάσαμε ευχάριστα καθ' όλη την διάρκεια της εργασίας.

Αυτή η εργασία, όπως και η ολοκλήρωση των σπουδών μου στο Πολυτεχνείο δεν θα ήταν δυνατές χωρίς την στήριξη της οικογένειάς μου. Τους γονείς μου, Δημητρία και Δημήτρη, που με στηρίζουν σε κάθε μου βήμα, και την αδελφή μου Γαρυφαλλιά που βρίσκεται πάντα στο πλευρό μου.

Κλείνοντας, ένα μεγάλο ευχαριστώ στους συνοδοιπόρους των φοιτητικών ετών, τους κολλητούς μου φίλους. Οι αμέτρητες ώρες που περάσαμε μαζί, διαβάζοντας, γελώντας, διασκεδάζοντας, με εφοδίασαν με αναμνήσεις για μια ζωή. Ένα ευχαριστώ είναι το ελάχιστο που μπορώ να πω.

Αθήνα, Μάρτιος 2024

Στεφανία Σκόρδα

Table of Contents

List of Figures

List of Tables

List of Abbreviations

Abbreviation	Definition
3DP	3D Printing
BNC	Bayonet Neill-Concelman
BNC	Bayonet Neill-Concelman
BSE	Back scattered electrons
BSE	Back scattered electrons
CMOS	Complementary Metal-Oxide-Semiconductor
CMOS	Complementary Metal-Oxide-Semiconductor
CTENG	Contact Triboelectric Nanogenerator
CTENG	Contact Triboelectric Nanogenerator
DMT	The Derjaguin, Muller, and Toporov
DMT	The Derjaguin, Muller, and Toporov
DUT	Device Under Test
DUT	Device Under Test
EDAX	Energy Dispersive X-ray Analysis
EDX	Energy Dispersive X-ray
FDM	Fused Deposition Modeling
FEI	Field Emission Ionization
FFF	Fused Filament Fabrication
GPIB	General Purpose Interface Bus
INN	Institute of Nanocience and Nanotechnology
Isc	Short Circuit Current
ISO	International Organization for Standardization
JKR	Johnson, Kendall, Roberts theory
LCR	Inductance, Capacitance, and Resistance
MEMS	Microelectromechanical systems
MIM	Metal-Insulator-Metal
MOSFET	Metal–Oxide–Semiconductor Field-Effect Transistor
NCSR	National Centre For Scientific Research
NTUA	National Technical University of Athens
PC	Personal Computer
PCB	Printed Circuit Board
PLA	Polylactic Acid
PMMA	Poly(methyl methacrylate)
PVD	Physical Vapor Deposition
PVDF	Polyvinylidene fluoride (PVDF)
RF	Radio Frequency
RFID	Radio-Frequency Identification
SEM	Scanning Electron Microscopy
SI	International System of Units
SiC	Silicon Carbide

SM	Surface Modification
TEHG	Triboelectric-Electromagnetic-Hybrid Generator
TENG	Triboelectric Nanogenerator
TEPG	Triboelectric-Electromagnetic- Piezoelectric Hybrid Generator
TES	Triboelectric Sensors
TIR	Transimpedance amplifier
UI	User Interface
ZnO	Zinc Oxide

Chapter I

Εκτεταμένη Περίληψη στα Ελληνικά

Εκτεταμένη Περίληψη στα Ελληνικά

1.1 Εισαγωγή

Η συλλογή της μηχανικής ενέργειας μέσω τριβοηλεκτρικού φαινομένου έχει προκύψει ως μια κρίσιμη εναλλακτική μέθοδος για την μετατροπή της άφθονης μηχανικής ενέργειας που περιβάλλει εμάς σε χρήσιμη ηλεκτρική ενέργεια, η οποία μπορεί να τροφοδοτήσει ηλεκτρονικές συσκευές και συστήματα. Ακολουθώντας την ανακάλυψη της τριβοηλεκτρικής νανογεννήτριας (TENG) από την ομάδα του Zhong Lin Wang [1], υπήρξε μια εκθετική αύξηση στην ερευνητική δραστηριότητα γύρω από την αποδοτική συλλογή τριβοηλεκτρικής ενέργειας, χρησιμοποιώντας διάφορα υλικά και τεχνολογίες [2], [3], [4]. Η δυνατότητα της ανταλλαγής φορτίων ανάμεσα σε δύο επιφάνειες που έρχονται σε επαφή (triboelectrification) και της ηλεκτροστατικής επαγωγής (electrostatic induction), όταν αυτές οι επιφάνειες βρίσκονται σε σχετική κίνηση μεταξύ τους, εμφανίζεται σε κάθε συνδυασμό υλικών ενώ ταυτόχρονα αναδεικνύεται η πρόκληση για την εύρεσης ιδανικών συνδυασμών υλικών για τη μεγιστοποίηση της απόδοσης των τριβογεννητριών. Η εμφάνιση της τρισδιάστατης εκτύπωσης (3D printing) [5] ως μιας οικονομικά αποδοτικής κατασκευαστικής διαδικασίας, η οποία επιτρέπει την παραγωγή ποικίλων δομών με ελάχιστη σπατάλη υλικών και συντομεύει τον χρόνο παραγωγής, καθιστά εύλογη την ανάπτυξη τριβοηλεκτρικών διατάξεων με βάση αυτήν την τεχνολογία για αυτοτροφοδοτούμενα ηλεκτρονικά συστήματα [6].

Το πολυγαλακτικό οξύ (PLA), ένα ανακυκλώσιμο, βιοσυμβατό και βιοδιασπώμενο φυσικό θερμοπλαστικό υλικό παραγόμενο από ανανεώσιμες πηγές, χρησιμοποιείται ευρέως στην κατασκευή τριβοηλεκτρικών διατάξεων. Στην εργασία αυτή, αναλύουμε τον αντίκτυπο των νανοσωματιδίων SiC και ZnO στην απόδοση των τριβοηλεκτρικών νανογεννητριών σε ανάμειξη με το PLA.

1.2 Θεωρητικό Υπόβαθρο

Ο τριβοηλεκτρισμός, ή τριβοηλεκτρική φόρτιση, αναφέρεται στη δημιουργία ηλεκτρικού φορτίου σε υλικά μέσω επαφής ή τριβής. Το τριβοηλεκτρικό φαινόμενο έχει αξιοποιηθεί στην ανάπτυξη τριβοηλεκτρικών νανογεννητριών (TENG), οι οποίες μετατρέπουν μηχανική ενέργεια από το περιβάλλον σε ηλεκτρική ενέργεια. Οι TENGs αντιπροσωπεύουν μια νέα προσέγγιση στη συγκομιδή ενέργειας, προσφέροντας μια βιώσιμη λύση για την τροφοδοσία ηλεκτρονικών συσκευών χωρίς να βασίζονται σε συμβατικές πηγές ενέργειας. Η τεχνολογία αυτή έχει εφαρμογές που κυμαίνονται από αυτοτροφοδοτούμενους αισθητήρες έως τη συγκομιδή ενέργειας από την ανθρώπινη κίνηση και τις περιβαλλοντικές δονήσεις.

1.2.1 Τριβοηλεκτρικό Φαινόμενο

Το τριβοηλεκτρικό φαινόμενο αποτελεί το συνηθέστερο λόγο εμφάνισης του στατικού ηλεκτρισμού. Το φαινόμενο βασίζεται στην επαφή δύο ανόμοιων επιφανειών, οι οποίες ανταλάσσουν μεταξύ τους φορτία.. Τη στιγμή που τα δύο υλικά έρχονται σε επαφή, φορτία μεταφέρονται από το ένα υλικό στο άλλο. Καθώς διαχωρίζονται οι δύο επιφάνειες το κάθε υλικό συγκρατεί το ηλεκτρικό φορτίο που απομονώνεται από το κενό μεταξύ τους. Στην περίπτωση που συνδεθεί ένα εξωτερικό ηλεκτρικό φορτίο (π.χ. μία αντίσταση) ανάμεσα στα δύο ηλεκτρόδια που βρίσκονται στα άκρα των επιφανειών τότε θα εμφανιστεί ροή ρεύματος εξ επαγωγής με σκοπό την εξισορρόπηση των φορτίων.

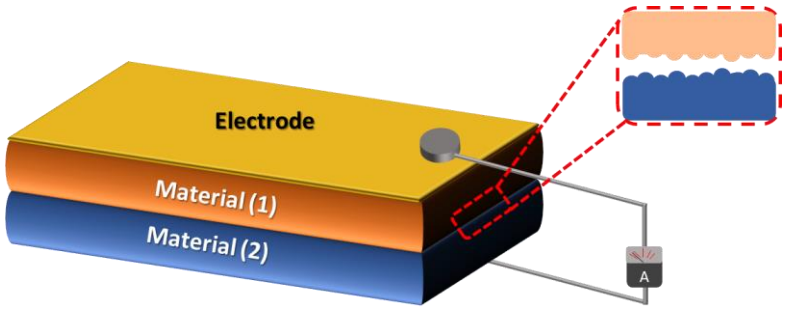

Figure 0.1 Επαφή τριβοηλεκτρικών επιφανειών και σύνδεση ηλεκτροδίων με φορτίο.

Η μεταφορά φορτίων, συνήθως ηλεκτρονίων, από μία επιφάνεια σε άλλη, σε σχέση με τα διαφορετικά υλικά που επιλέγονται για να εκμεταλλευτούν το φαινόμενο της τριβοηλεκτρισμού και εξαρτάται από την ηλεκτρική τους πολικότητα. Κάποια υλικά διαθέτουν εντονότερη τάση να κατακρατούν ηλεκτρόνια σε σύγκριση με άλλα, το ίδιο όπως υπάρχουν υλικά που φαίνεται να αποβάλλουν ηλεκτρόνια πιο εύκολα. Η αποτίμηση αυτής της δυνατότητας για τα υλικά παρουσιάζεται στο Figure 0.2 μέσω μιας καθορισμένης τριβοηλεκτρικής σειράς για ποικίλα υλικά.

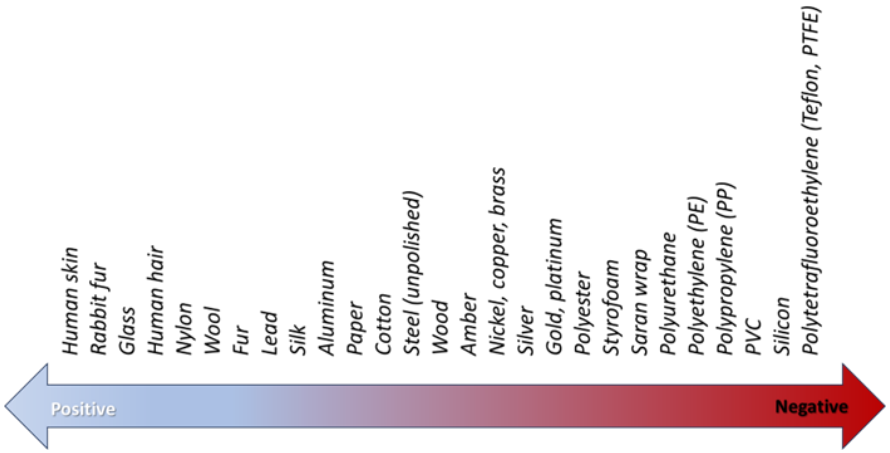

Figure 0.2 Τριβοηλεκτρική σειρά υλικών για την κατασκευή τριβοηλεκτρικών επιφανειών [1]

1.2.2 Αρχή και Τρόποι Λειτουργίας Τριβοηλεκτρικών Νανογεννητριών

Οι τριβογεννήτριες λειτουργούν με βάση τον συνδυασμό της ηλεκτρικής αλληλεπίδρασης και της ηλεκτροστατικής επαγωγής. Η αλληλεπίδραση αυτή δημιουργεί στατικά φορτία, ενώ η ηλεκτροστατική επαγωγή αντιστοιχεί στη διαδικασία μετατροπής της κινητικής ενέργειας σε ηλεκτρική. Η ικανότητα της ηλεκτροστατικής επαγωγής να αντικατοπτρίζει τη λειτουργία ενός πυκνωτή σημαίνει ότι οι τριβογεννήτριες φέρουν εγγενώς χωρητικά χαρακτηριστικά. Όταν δύο ετερογενή υλικά έλθουν σε επαφή, δημιουργείται ένας χημικός δεσμός ονομαζόμενος προσκόλληση, ωθώντας τη μεταφορά φορτίων ανάμεσα στα υλικά προκειμένου να επιτευχθεί ισορροπία στο ηλεκτροχημικό τους δυναμικό. Αυτή η μεταφορά μπορεί να περιλαμβάνει ηλεκτρόνια, ιόντα ή ακόμη και μόρια. Κατά τη διαδικασία του διαχωρισμού, κάποια άτομα προτιμούν να διατηρούν επιπλέον ηλεκτρόνια ενώ άλλα είναι πρόθυμα να τα αποβάλλουν, γεγονός που μπορεί να προκαλέσει τριβοηλεκτρική φόρτιση στις επιφάνειες. Η εμφάνιση τριβοηλεκτρικών φορτίων στις επιφάνειες αυτές αποτελεί το κίνητρο για την ηλεκτρονική μεταφορά προς τα ηλεκτρόδια, αντισταθμίζοντας το ηλεκτρικό δυναμικό που δημιουργείται [1].

Όταν αναλύουμε μέσω μαθηματικών το πώς δημιουργείται η διαφορά δυναμικού σε κάθε μορφή τριβοηλεκτρικής νανογεννήτριας, καταλήγουμε σε μία βασική εξίσωση:

$$V = \frac{|Q|}{C(x)} + V_{oc}(x) \qquad (0.1)$$

Το μέγεθος $|Q|$ αναφέρεται στα προκύπτοντα θετικά και αρνητικά φορτία στις επιφάνειες των διαφορετικών υλικών μετά την απομάκρυνσή τους μεταξύ τους. Ο όρος C χαρακτηρίζει την χωρητικότητα ανάμεσα στα ηλεκτρόδια όταν συμβαίνει μεταφορά ηλεκτρονίων, ενώ το V_{oc} είναι η μέτρηση της διαφοράς δυναμικού που προκύπτει από τα τριβοηλεκτρικά φορτία. Αυτά τα μεγέθη είναι συναρτήσει της απόστασης x μεταξύ των υλικών, καθώς αυτή μεταβάλλεται.

Παρακάτω απεικονίζονται οι τέσσερις βασικοί τρόποι λειτουργίας των τριβοηλεκτρικών νανογεννητριών (TENGs). Στην παρούσα εργασία θα χρησιμοποιηθεί η λειτουργία κάθετου τρόπου επαφής-διαχωρισμού όπου θα αναλυθεί παραπάνω στα επόμενα κεφάλαια.

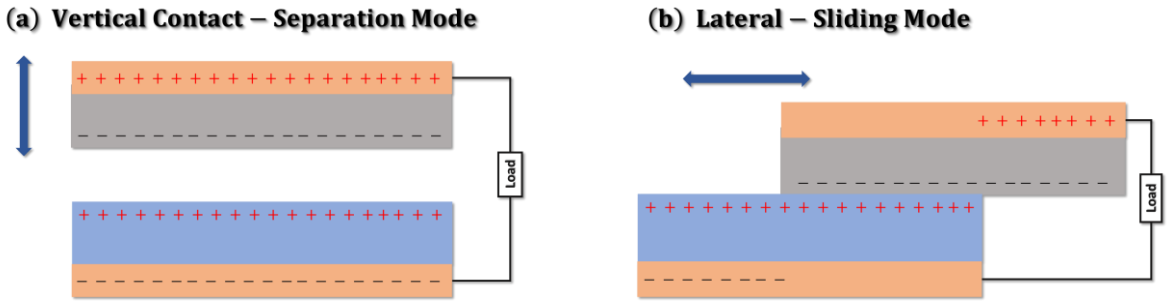

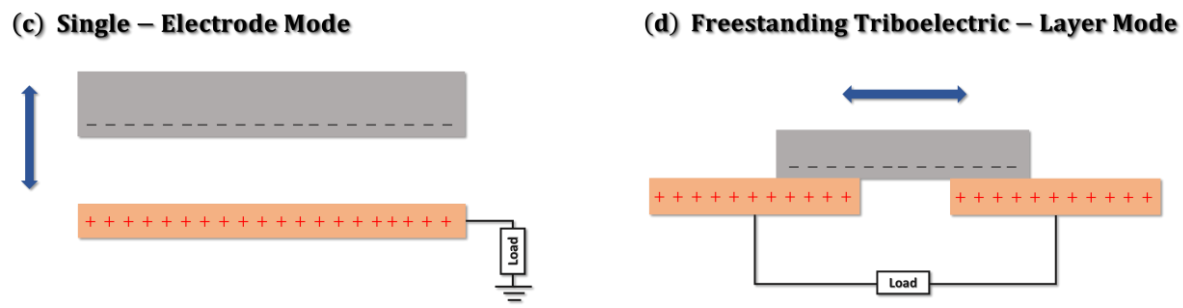

Figure 0.3 Οι τέσσεροι βασικοί τρόποι λειτουργίας των τριβοηλεκτρικών νανογεννητριών: (α) Λειτουργία κάθετου τρόπου επαφής- διαχωρισμού (β) Λειτουργία πλευρικού τρόπου ολίσθησης (γ) Λειτουργία μονού ηλεκτροδίου (δ) Λειτουργία ελεύθερων τριβοηλεκτρικών στρωμάτων

Στη λειτουργία κάθετης επαφής, οι επιφάνειες της TENG δομής βρίσκονται στραμμένες η μία προς την άλλη, στην εξωτερική επιφάνεια των οποίων εναποτίθενται ηλεκτρόδια. Η μηχανική δύναμη που ενεργοποιεί το φαινόμενο, ασκείται στον κάθετο άξονα και έτσι τα δύο υλικά έρχονται σε επαφή. Η επαφή των δύο υλικών οδηγεί σε συσσώρευση αντίθετου φορτίου στις επιφάνειες και η απομάκρυνση των επιφανειών, που οδηγεί στην σταδιακή αύξηση του κενού ανάμεσα τους, είναι η αιτία εμφάνισης της διαφοράς δυναμικού. Ως αποτέλεσμα, υπάρχει ροή ελεύθερων ηλεκτρονίων μέσω των ηλεκτρόδιων από την μία επιφάνεια στην άλλη, ώστε να εξισορροπηθεί το ηλεκτροστατικό πεδίο.

1.3 Υλικά

Το PLA (REVODE 101, Luminy LX175), που χρησιμοποιήθηκε ως μήτρα για το σύνθετο υλικό, προμηθεύτηκε από την Total Corbion. Η σκόνη SiC (#1200 mesh, περίπου 8.3 μm μέγεθος κόκκου) προμηθεύτηκε από την Struers. Η σκόνη ZnO (σχετικά "≤100 nm" σε μέγεθος νανοσωματιδίου) προμηθεύτηκε από την Sigma-Aldrich.

Τα πέλλετ PLA ξηράθηκαν για 24 ώρες στους 100 °C. Η σκόνη SiC αναμίχθηκε καλά με το PLA σε θερμαινόμενο μπολ στους 75 °C με ταυτόχρονη προσθήκη μερικών σταγόνων ακετόνης για να καταστεί δυνατή η προσκόλληση της σκόνης SiC στα σφαιρίδια. Το μείγμα ξηράθηκε εκ νέου στους 100 °C για 24 ώρες και αποθηκεύτηκε σε ξηραντήρα μέχρι την εξώθηση.

Παρασκευάστηκαν πέντε τύποι σύνθετων υλικών με 1, 1.5, 2, 2.5 και 3$wt\%$ SiC που αντιστοιχούν σε υπολογισμένες τιμές περίπου 0.4, 0.6, 0.8, 1.05 και 1.3$vol\%$ αντίστοιχα (λαμβάνοντας την πυκνότητα του PLA και του SiC ως 1,3g/cm^3 και 3,15g/cm^3 αντίστοιχα) και τρία σύνθετα υλικά PLA με πρόσμιξη ZnO όπου παρασκευάστηκαν με παρόμοια μέθοδο με συγκεντρώσεις που κυμαίνονταν από 1$wt\%$ έως 3$wt\%$.

1.3.1 Παρασκευή δοκιμίων

Το αποξηραμένο μείγμα μεταφέρθηκε σε εξωθητή μονού κοχλία (Felfil Evo) για την παραγωγή συνεχούς σύνθετου νήματος διαμέτρου περίπου 1.75 mm. Η θερμοκρασία εξώθησης ήταν 185 –

195 °C και ο ρυθμός εξώθησης ήταν 50 cm ανά λεπτό. Καθαρό νήμα PLA παρήχθη επίσης μετά από πανομοιότυπες συνθήκες ξήρανσης και μέθοδο εξώθησης.

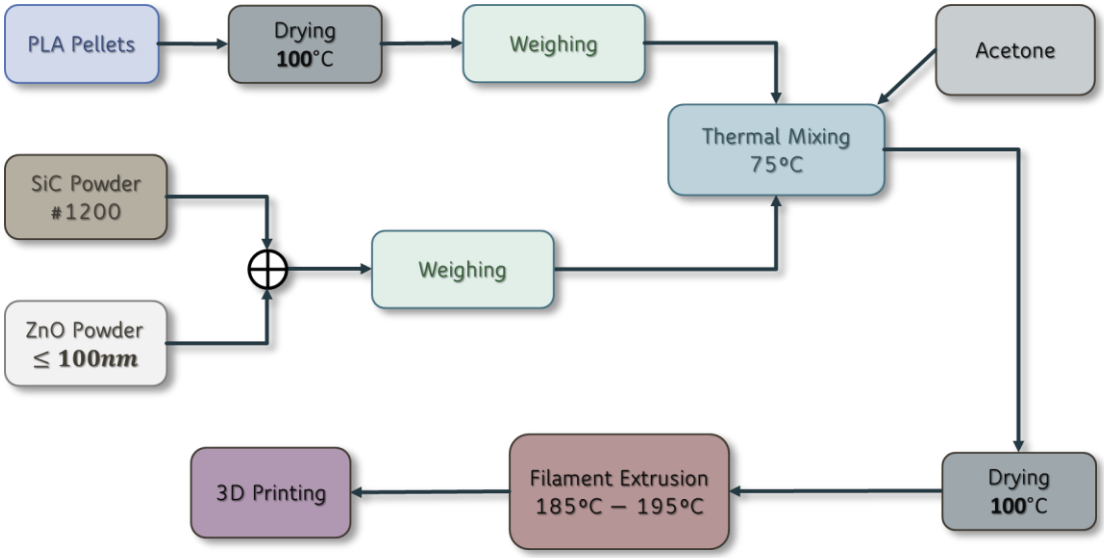

Figure 0.4 Διαδικασία Παρασκευής Δοκιμίων

Τα διάφορα δοκίμια που χρησιμοποιήθηκαν σε αυτή τη μελέτη κατασκευάστηκαν με το νήμα που παρήχθη χρησιμοποιώντας έναν τρισδιάστατο εκτυπωτή CREALITY CR20 Pro. Τα δοκίμια εκτυπώθηκαν τρισδιάστατα χρησιμοποιώντας τις ακόλουθες παραμέτρους: διάμετρος νήματος = 1,75 mm, θερμοκρασία ακροφυσίου = $200 - 210\,°C$, θερμοκρασία του bed = $55\,°C$, μέγεθος ακροφυσίου = 1 mm και ταχύτητα εκτύπωσης = 50 mm/sec.

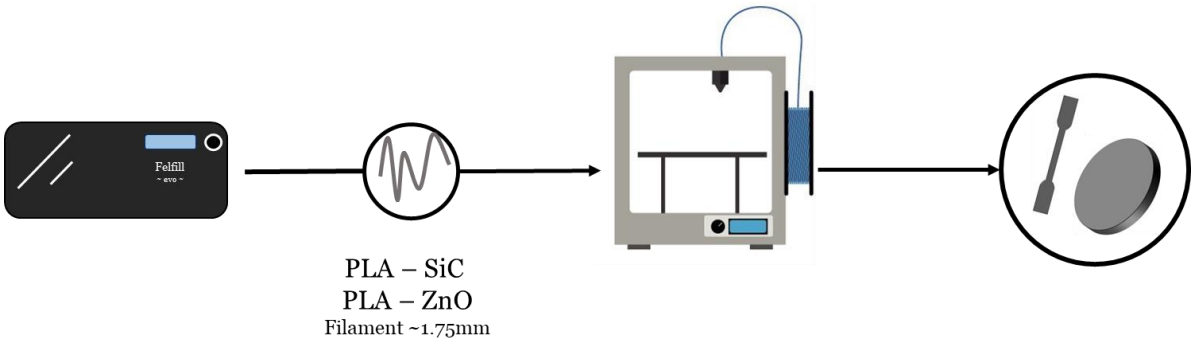

Figure 0.5 Διαδικασία από την εξώθηση νήματος έως την τρισδιάστατη εκτύπωση των δοκιμίων.

1.3.2 Δομικός Χαρακτηρισμός

Στο Figure 0.6 (a) παρουσιάζονται χαρακτηριστικές επιφάνειες θραύσης ενός δοκιμίου PLA-3wt% SiC μετά από κόπωση και θραύση σε εφελκυσμό. Κατά κύριο λόγο είναι ορατή η όλκιμη θραύση με κάποιες ενδείξεις εύθραυστης θραύσης, όπως αποδεικνύεται από κάποιες λεπτές ραβδώσεις (ορατές στο Figure 0.6 (a)).

Μια εκτίμηση της επιφανειακής πυκνότητας του SiC στην επιφάνεια των δοκιμίων 3wt% έδειξε τιμές μεταξύ 1 και 1,5 $areal$%, οι οποίες βρίσκονται σε γενική συμφωνία με το 1,3 vol% SiC που έχει υπολογιστεί για τέτοια υλικά.

Ακόμη, ένα φάσμα EDX ενός δείγματος PLA-3%SiC σε χαμηλή μεγέθυνση ($x100$) παρουσιάζεται στο Figure 0.6 (b), όπου η κορυφή Si καλύπτεται εν μέρει και καλύπτεται ελαφρώς από μια κορυφή χρυσού.

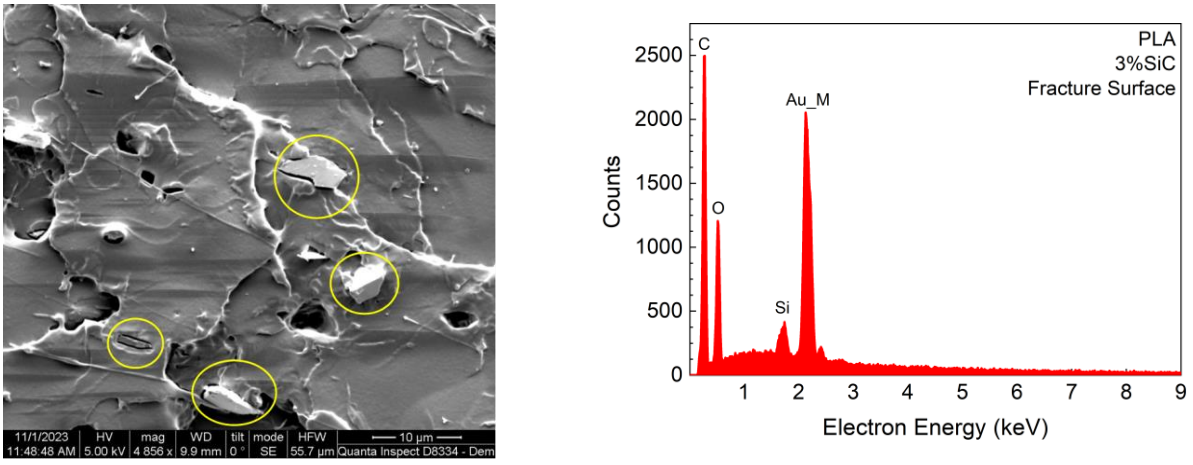

(α) **(β)**

Figure 0.6 Εικόνες SEM για 3% SiC από (α) επιφάνεια θραύσης από τάση με μέγεθος x4856 και (β) μετά από τριβή με χαρτί #1000 SiC με μέγεθος x6035.

Το Figure 0.7 (a) δείχνει μια απεικόνιση με SEM του PLA με προσθήκη ZnO, όπου μπορούμε να εντοπίσουμε την παρουσία νανοσωματιδίων ZnO. Η κατανομή των νανοσωματιδίων ZnO φαίνεται να είναι ομοιόμορφη. Στο Figure 0.7 (b) παρουσιάζεται ένα φάσμα EDX που αποκτήθηκε για το PLA με 3wt% ZnO. Μπορούμε να αναγνωρίσουμε τις κορυφές εκπομπής L και K του Zn στα 1,011keV και 8,61keV, επαληθεύοντας την ύπαρξη νανοσωματιδίων ZnO. Οι κορυφές εκπομπής στα 1,66eV και 2,14 eV αντιστοιχούν στο λεπτό στρώμα χρυσού που εναποτέθηκε στο δείγμα PLA πριν από την απεικόνιση με SEM, προκειμένου να αποφευχθούν φαινόμενα επιφανειακής φόρτισης.

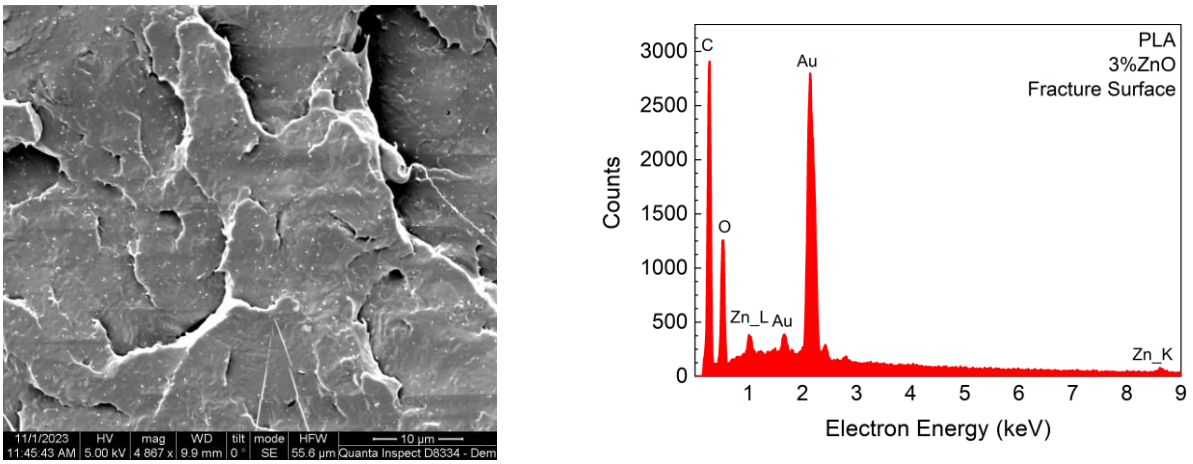

(α) **(β)**

Figure 0.7 Εικόνες SEM για 3% ZnO από (α) επιφάνεια θραύσης από τάση με μέγεθος x4867 και (β) μετά από τριβή με χαρτί #1000 SiC με μέγεθος x6019.

1.4 Μηχανικός Χαρακτηρισμός

Τα εννιά διαφορετικά υλικά που εξετάστηκαν (PLA με 0, 1, 1.5, 2, 2.5 και 3% SiC και 1, 2, 3% ZnO) χαρακτηρίστηκαν με μετρήσεις της αντοχής τους σε εφελκυσμό πριν και μετά την κόπωση, καθώς και με μετρήσεις της αντοχής σε τριβή, της σκληρότητας Shore D και της αντοχής σε σημειακή συμπίεση Hertz. Όλες οι μηχανικές δοκιμές πραγματοποιήθηκαν σε δοκίμια με συνθήκες θερμοκρασίας $23 \pm 2\ °C$ και $50 \pm 10\%$ σχετική υγρασία.

1.4.1 Δοκιμή εφελκυσμού έως την αστοχία μετά από κόπωση

Οι δοκιμές εφελκυσμού μέχρι αστοχίας πραγματοποιήθηκαν σύμφωνα με τις οδηγίες του προτύπου ISO 527. Τα δοκίμια που χρησιμοποιήθηκαν ήταν επίπεδα και είχαν σχήμα "dog-bone" με ονομαστικό μήκος μέτρου $40\ mm$, πλάτος μέτρου $6\ mm$ και πάχος μέτρου $2\ mm$. Οι δοκιμές πραγματοποιήθηκαν σε ένα πλαίσιο φόρτισης εφελκυσμού INSTRON 1026 με ρυθμό μετατόπισης $545 \mu m/min$ χρησιμοποιώντας λαβές. Τα δεδομένα εφελκυσμού καταγράφηκαν σε υπολογιστή μέσω μονάδας κλιματισμού με ακρίβεια $0.1N$, ενώ η ακρίβεια μετατόπισης εκτιμήθηκε σε $0.1\ mm$.

Τα δοκίμια δοκιμάστηκαν υπό εφελκυσμό πριν και μετά την κόπωση για τον προσδιορισμό της εναπομένουσας αντοχής. Η κόπωση των δοκιμίων εφελκυσμού πραγματοποιήθηκε υπό μικτή λειτουργία εφελκυσμού-καμπυλότητας σε ένα ειδικά κατασκευασμένο σύστημα. Τα δοκίμια δοκιμάστηκαν υπό κόπωση μεταξύ περίπου 50% της μέγιστης αναμενόμενης εφελκυστικής παραμόρφωσης και περίπου 50% της μέγιστης αναμενόμενης καμπτικής παραμόρφωσης για έως και 400 κύκλους με ρυθμό περίπου 0.5 Hz (2 δευτερόλεπτα ανά κύκλο).

Οι καμπύλες load-extension που ελήφθησαν αναλύθηκαν για να ληφθεί η τελική εφελκυστική αντοχή (UTS, Stress at Maximum Load) και η παραμόρφωση στο μέγιστο φορτίο (Strain at Maximum Load).

Τουλάχιστον 4 δείγματα με έως και 3wt% SiC δοκιμάστηκαν υπό εφελκυστική δύναμη πριν και μετά την κόπωση μικτού τρόπου και τα αποτελέσματα παρουσιάζονται στην ενότητα Figure 0.8 (a) (Ultimate tensile strength , UTS) και Figure 0.8 (b) (Strain at maximum load). Το UTS φαίνεται να μειώνεται με τον αριθμό των κύκλων κόπωσης κατά περίπου 10% μετά από περίπου 100 κύκλους για το καθαρό PLA και το 1% SiC, πιθανώς λόγω της συσσώρευσης λεπτών μικρορωγμών που οδηγεί σε τοπικές συγκεντρώσεις τάσεων. Από την άλλη πλευρά, το UTS φαίνεται να αυξάνεται κατά περίπου 10% μετά από περίπου 100 κύκλους όταν η πρόσμιξη SiC αυξάνεται σε 2% ή 3%, πιθανώς λόγω της εμπλοκής των μικρορωγμών με τα σωματίδια SiC τα οποία μπορούν να μειώσουν τις τοπικές συγκεντρώσεις τάσεων μέσω της τοπικής αμβλύνσεως. Επιπλέον, σε περιεκτικότητες SiC μεγαλύτερες ή ίσες με περίπου 2%, οι δεσμοί των σωματιδίων SiC μπορούν να λειτουργήσουν ως

"άγκυρες" για τυχόν μικρορωγμές που αναπτύσσονται κατά την κόπωση, καθυστερώντας την ανάπτυξή τους.

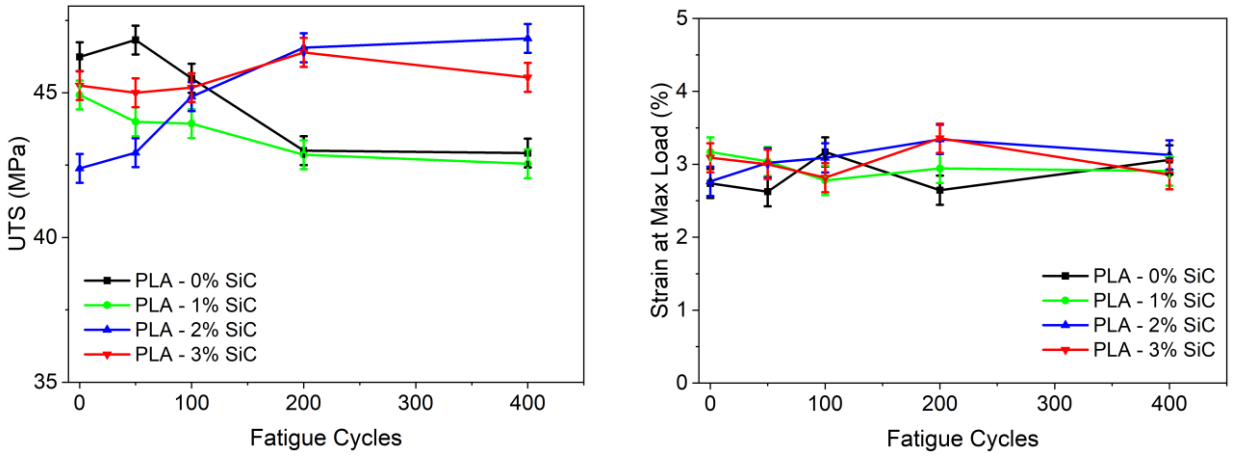

(α) **(β)**

Figure 0.8 (a) Ultimate tensile strength του σύνθετου PLA και (β) Strain at max load του SiC-dopped PLA μετά από κόπωση για PLA-SiC.

Η παραμόρφωση στο μέγιστο φορτίο του σύνθετου υλικού PLA παρουσιάζεται στο Figure 0.8 (b). Σε όλες τις περιπτώσεις, η παραμόρφωση στο μέγιστο φορτίο ήταν περίπου 3% και δεν βρέθηκε σημαντική διαφορά στην παραμόρφωση μέχρι 400 κύκλους κόπωσης μικτού τρόπου. Αυτό δείχνει ότι δεν δημιουργούνται ή δημιουργούνται λίγες σημαντικές μικρορωγμές από την κόπωση μικτού τρόπου σε αυτά τα υλικά, τουλάχιστον μέχρι 400 κύκλους.

1.4.2 Σκληρότητα Shore D

Η σκληρότητα Shore D μετρήθηκε σε διάφορα σημεία της επιφάνειας των 3DP δοκιμίων με διάμετρο 32 mm και πάχος 7 mm με τη χρήση σκληρόμετρου με κλίμακα Shore D. Η σκληρότητα δίνεται με έναν αριθμό χωρίς μονάδα μεταξύ 1 και 100.

Η αύξηση της αντοχής σε εφελκυσμό που παρατηρείται για την πρόσμιξη SiC επιβεβαιώνεται από τις μετρήσεις της σκληρότητας Shore D που παρουσιάζονται στο Figure 0.9 (a). Η σκληρότητα Shore D είναι σχετικά ανεπηρέαστη μέχρι περίπου 1% SiC, αλλά αυξάνεται απότομα στη συνέχεια και φτάνει σε ένα πλατό περίπου στο 2% SiC.

Η μείωση της αντοχής σε εφελκυσμό και η μείωση της σκληρότητας Shore D κατά την προσθήκη νανοσωματιδίων ZnO σε μια πολυμερική μήτρα υλικού, όπως το πολυγαλακτικό οξύ (PLA), μπορεί να αποδοθεί στις πολύπλοκες αλληλεπιδράσεις μεταξύ των νανοσωματιδίων και της πολυμερικής μήτρας, καθώς και στα ειδικά χαρακτηριστικά που αυτά τα νανοσωματίδια προσδίδουν στο σύνθετο υλικό.

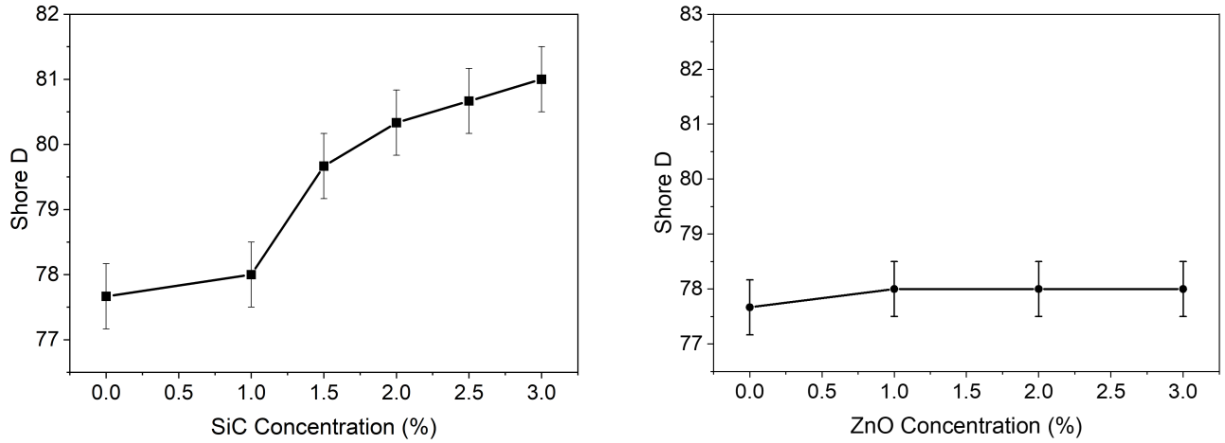

(α) **(β)**

Figure 0.9 Αποτελέσματα σκληρότητας Shore D για (α) PLA-SiC και (β) PLA-ZnO.

1.4.3 Abrasion Resistance

Η αντοχή των υλικών στην τριβή 2 σωμάτων διερευνήθηκε σε δοκίμια με διάμετρο 32 mm και πάχος 7 mm σε προσαρμοσμένη περιστρεφόμενη εγκατάσταση στίλβωσης, βασισμένη σε λειαντήρα/στιλβωτή STRUERS DAP-7 με υποδοχή δοκιμίου PEDEMIN-2 στις 125 στροφές ανά λεπτό. Δοκιμάστηκαν τρία δοκίμια μαζί και κάθε δοκίμιο δοκιμάστηκε με φορτίο 10N (μέση τάση σε κάθε δοκίμιο $12kPa$) και δοκιμάστηκε έναντι φρέσκου χαρτιού SiC #1000 για 1 λεπτό με συνεχή παροχή νερού για την απομάκρυνση τυχόν χαλαρών σωματιδίων και την αποφυγή τριβής 3 σωμάτων. Τα δοκίμια στεγνώθηκαν και ζυγίστηκαν πριν και μετά τη δοκιμή με ακρίβεια $1mg$ και η αντοχή στην τριβή δίνεται από το αντίστροφο της απώλειας βάρους ανά μονάδα επιφάνειας του δοκιμίου με μονάδες m^2/kg.

Η αντοχή στην τριβή αυξάνεται απότομα ακόμη και με μόλις 1% SiC, δεδομένου ότι το SiC είναι πολύ σκληρότερο από το PLA και προστατεύει τη μήτρα PLA από τους κόκκους τριβής, όπως φαίνεται στο Figure 0.10(α).

Για το PLA-ZnO, ενώ η μείωση των μηχανικών ιδιοτήτων υποδηλώνει πιθανές αρνητικές επιπτώσεις στην αντοχή στην τριβή, αυτό παρατηρήθηκε. Προστέθηκε ποσότητα νανοσωματιδίων ZnO και διαπιστώθηκε ότι αυτό μείωσε κάπως την αντίσταση στην τριβή, όπως φαίνεται στο Figure 0.10(α).

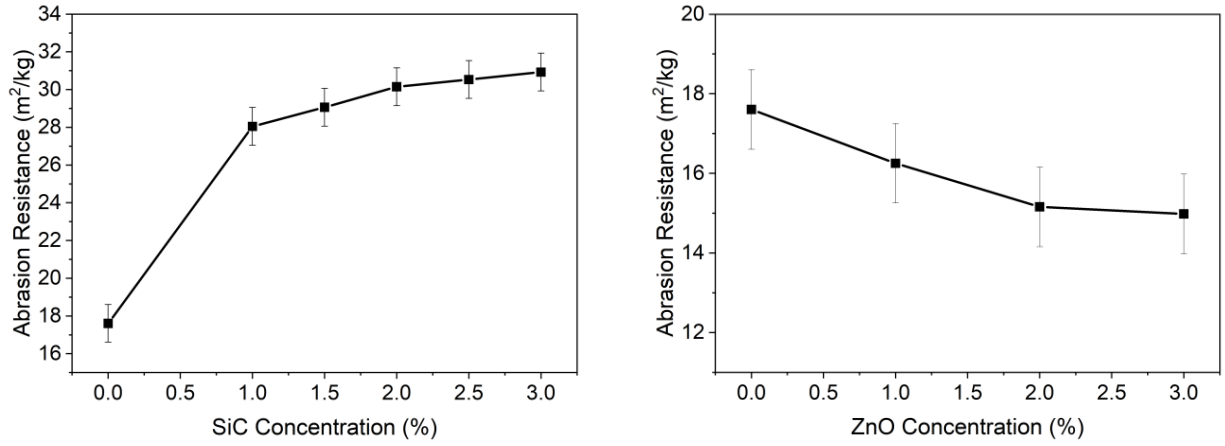

(α) **(β)**

Figure 0.10 Αποτελέσματα για την αντοχή σε τριβή των (α) PLA-SiC και (β) PLA-ZnO.

1.4.4 Συμπίεση Hertzian Point

Η αντίσταση των υλικών σε σημειακή φόρτιση μετρήθηκε υπό συνθήκες φόρτισης "σημειακής επαφής Hertz" με τη χρήση πείρου από χάλυβα με ακτίνα καμπυλότητας 2.5 mm με ρυθμό μετατόπισης $500 \mu m/min$ στο INSTRON 5982. Τα δοκίμια που δοκιμάστηκαν είχαν διάμετρο 32 mm και ονομαστικό πάχος 7 mm και η φόρτιση καταγράφηκε έως ότου ο indentor διεισδύσει σε βάθος 0,5 mm. Η αντίσταση σε σημειακή συμπίεση Hertz δίνεται από την κλίση της εφαπτομένης στην καμπύλη φορτίου βάθους σε βάθος διείσδυσης 0,5 mm σε μονάδες N/mm.

Τα αποτελέσματα που προέκυψαν για τη συμπίεση της σφαίρας Hertz παρουσιάζονται στα Figure 0.11 (a) (καμπύλες μέσου βάθους φορτίου) και Figure 0.11 (b) (μέσες κλίσεις). Η κλίση (υπολογιζόμενη μεταξύ 0,3 και 0,45 mm βάθος διείσδυσης για όλες τις καμπύλες).) των καμπυλών βάθους φορτίου μπορεί να θεωρηθεί ως μέτρο της "αποτελεσματικής σκληρότητας", δηλαδή της πλαστικής παραμόρφωσης και τα αποτελέσματα δείχνουν ότι η αποτελεσματική σκληρότητα αυξάνεται μετά από περίπου 1-1,5% SiC φθάνοντας σε ένα οροπέδιο σε περίπου 2wt% SiC, περίπου 40% πάνω από την τιμή για καθαρό PLA.

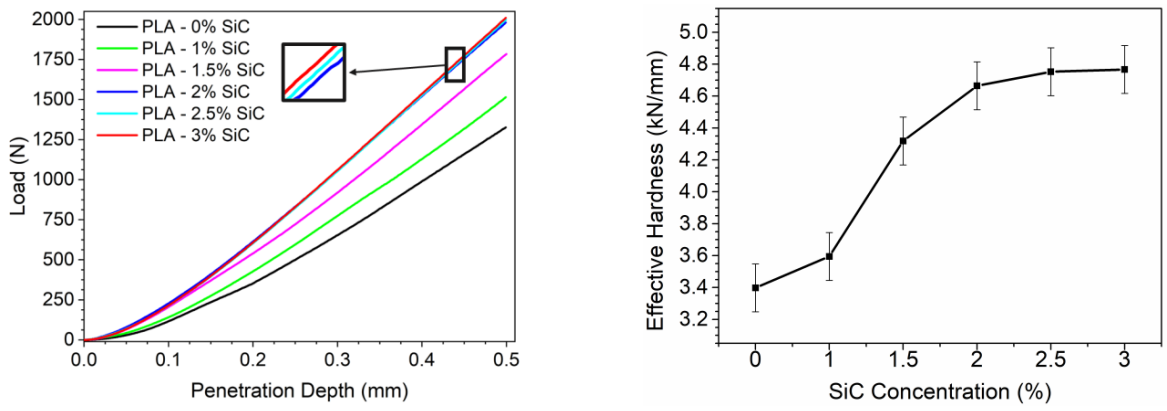

(α) **(β)**

Figure 0.11 Αποτελέσματα για δοκίμια με 1-3wt% SiC για (α) τη δύναμη επαφής Hertz με τα δεδομένα της δοκιμής συμπίεσης και (β) την αποτελεσματική σκληρότητα.

Η αύξηση της πραγματικής σκληρότητας μετά από περίπου 1-1,5% SiC οφείλεται πιθανώς στα εμπόδια που παρουσιάζουν τις συνδέσεις των σωματιδίων SiC στην πλαστική παραμόρφωση της μήτρας PLA. Μόλις στο 1% τα σωματίδια SiC είναι ενδεχομένως πολύ μακριά το ένα από το άλλο για να σχηματίσουν συνεχείς συνδέσεις, αλλά μέχρι το 1,5% τα σωματίδια είναι αρκετά κοντά το ένα στο άλλο ώστε να προκαλούν σχετικά εμπόδια στην περαιτέρω πλαστική παραμόρφωση, αυξάνοντας τη σκληρότητα.

Τα αποτελέσματα που προέκυψαν για τη συμπίεση με σφαίρα Hertzian για τα σύνθετα υλικά ZnO παρουσιάζονται στην ενότητα Figure 0.12(a) (average load-depth curves) και Figure 0.12 (b) (average gradients). Τα νανοσωματίδια ZnO, όταν προστίθενται στο PLA, τείνουν να μειώνουν τόσο την αντοχή σε εφελκυσμό όσο και την πραγματική σκληρότητα του υλικού. Η μείωση της αντοχής σε εφελκυσμό θα μπορούσε να οφείλεται σε παράγοντες όπως η συσσωμάτωση των σωματιδίων, όπως αναφέρθηκε προηγουμένως, η οποία μπορεί να δημιουργήσει αδύναμα σημεία στο σύνθετο υλικό. Η μείωση της πραγματικής σκληρότητας υποδηλώνει ότι η παρουσία των σωματιδίων ZnO μεταβάλλει την απόκριση του σύνθετου υλικού στη συμπίεση, καθιστώντας το πιο ευαίσθητο στην παραμόρφωση.

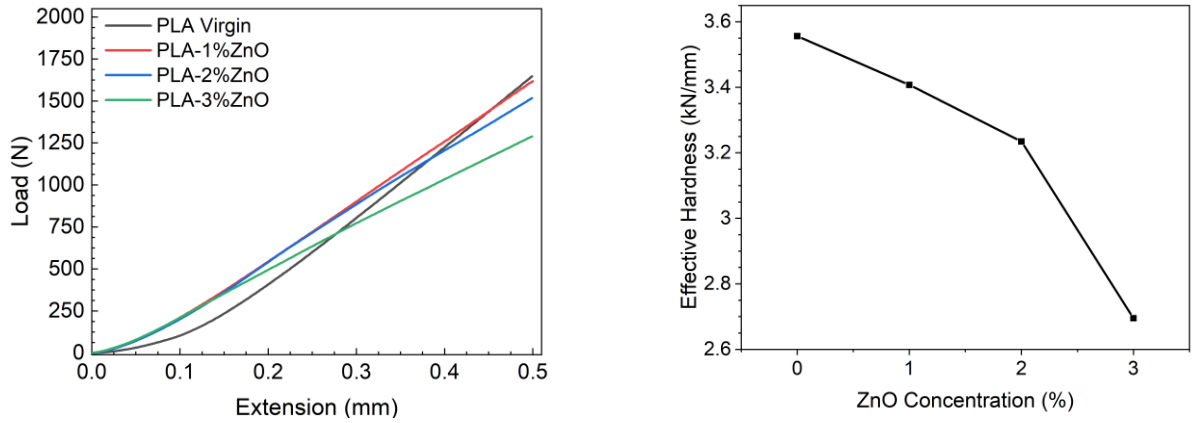

(α) **(β)**

Figure 0.12 Αποτελέσματα για δοκίμια με 1-3wt% ZnO για (α) τη δύναμη επαφής Hertz με τα δεδομένα της δοκιμής συμπίεσης και (β) την αποτελεσματική σκληρότητα.

1.5 Ηλεκτρικός Χαρακτηρισμός

Για την κατασκευή των πυκνωτών που χρησιμοποιήθηκαν στον ηλεκτρικό χαρακτηρισμό, εκτυπώθηκαν τρισδιάστατα και γυαλίστηκαν κυλινδρικά δείγματα διαμέτρου 32 mm και πάχους περίπου 390 μm για κάθε διαφορετικό υλικό.

Τα δείγματα χαρακτηρίστηκαν ηλεκτρικά με τη χρήση σταθμού ακίδων (prober) για τις ηλεκτρικές επαφές. Οι μετρήσεις χωρητικότητας πραγματοποιήθηκαν με τη χρήση του HP 4284A LCR meter. Οι μετρήσεις πραγματοποιήθηκαν για συχνότητες που κυμαίνονταν από $1kHz$ έως $1MHz$

και για τάσεις που κυμαίνονταν από $0V$ έως $\pm 2V$. Οι μετρήσεις ρεύματος διαρροής πραγματοποιήθηκαν με τη χρήση του HP4140B pA meter.

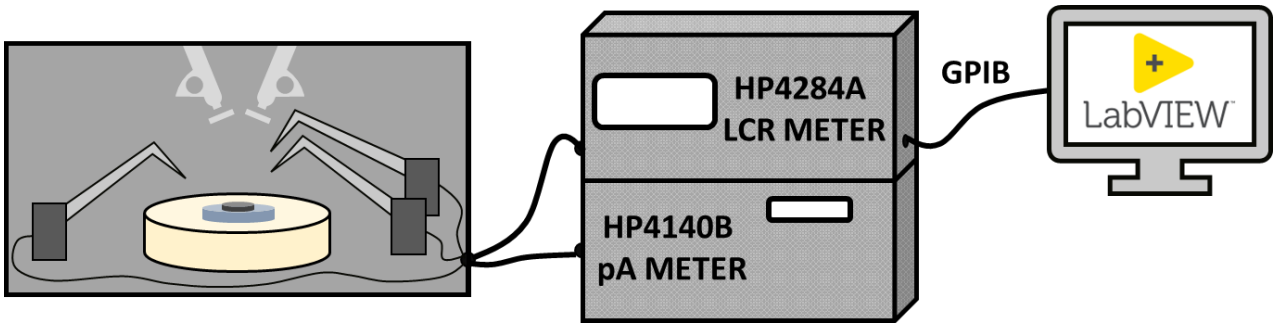

Figure 0.13 Αναπαράσταση του σταθμού ακίδων σε σύνδεση με HP4284A & HP4140B για τον ηλεκτρικό χαρακτηρισμό των δειγμάτων.

Οι μετρήσεις χωρητικότητας χρησιμοποιήθηκαν για τον υπολογισμό της διηλεκτρικής σταθεράς κάθε δείγματος χρησιμοποιώντας την εξίσωση

$$C_x = \frac{\varepsilon_o \cdot \varepsilon_x \cdot A}{d} \qquad (0.2)$$

όπου C_x είναι η μετρούμενη χωρητικότητα, $\varepsilon_o = 8.854x10^{-12}CV^{-1}m^{-1}$ είναι η διηλεκτρική διαπερατότητα του κενού, ε_x είναι η διηλεκτρική σταθερά του σύνθετου υλικού, A είναι η επιφάνεια του πυκνωτή και d είναι το πάχος του υλικού.

Ένα χαρακτηριστικό παράδειγμα μέτρησης της χωρητικότητας συναρτήσει της συχνότητας σε τάση πόλωσης 0 για όλα τα δείγματα εμφανίζεται στο Figure 0.14 (a). Φαίνεται ότι η χωρητικότητα είναι σχεδόν σταθερή, όπως αναμενόταν για το εύρος συχνοτήτων των μετρήσεων. Οι μικρές μεταβολές της χωρητικότητας κάθε δείγματος οφείλονται πιθανότατα στην παρουσία παγίδων φορτίου μεταξύ των επιφανειών μεταξύ του PLA και του Al. Το πιο σημαντικό, όμως, είναι ότι μεταξύ των δειγμάτων υπάρχει ευδιάκριτη διαφορά στη μετρούμενη χωρητικότητα.

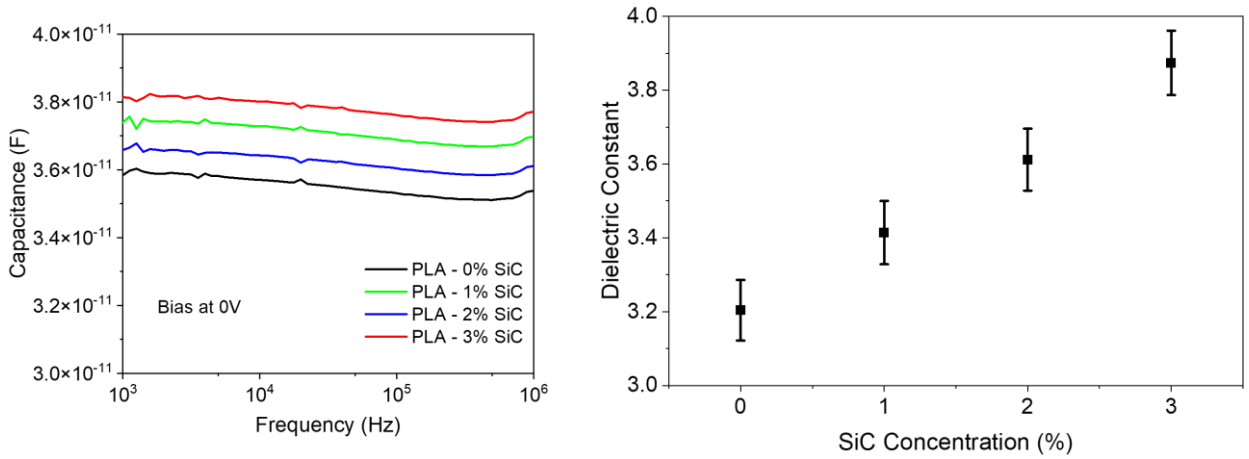

(α) **(β)**

Figure 0.14 (a) Χωρητικότητα συναρτήσει της συχνότητας σε μηδενική τάση πόλωσης για όλα τα δείγματα και (b) Διηλεκτρική σταθερά του σύνθετου υλικού PLA-SiC ως συνάρτηση της συγκέντρωσης SiC.

Χρησιμοποιώντας τη μετρούμενη χωρητικότητα στα $10kHz$, η διηλεκτρική σταθερά για κάθε δείγμα υπολογίστηκε χρησιμοποιώντας την εξίσωση (0.2). Τα αποτελέσματα παρουσιάζονται στο Figure 0.14 (b). Οι μπάρες σφάλματος έχουν υπολογιστεί χρησιμοποιώντας το σφάλμα που σχετίζεται με τη μέτρηση του πάχους του υλικού.

Από το Figure 0.14 (b) φαίνεται μια σαφής αύξηση της διηλεκτρικής σταθεράς με τη συγκέντρωση SiC. Η διηλεκτρική σταθερά του PLA με 0% SiC μετράται σε 3,2, η οποία είναι λίγο υψηλότερη από τις τιμές που έχουν αναφερθεί προηγουμένως και κυμαίνονται από 2,5 έως 3,11 [7], [8]. Η τιμή αυτή αυξάνεται μονοτονικά με τη συγκέντρωση SiC, σε 3,9 για το δείγμα PLA με 3% SiC. Λαμβάνοντας υπόψη ότι το SiC έχει διηλεκτρική σταθερά σχεδόν 15 [9] ,στη μορφή σκόνης, η παρατηρούμενη αύξηση της διηλεκτρικής σταθεράς με τη συγκέντρωση SiC δεν αποτελεί έκπληξη. Στην πραγματικότητα, αυτού του είδους το φαινόμενο έχει αποδειχθεί στη βιβλιογραφία για μια ποικιλία μορφών υλικού [10].

Το ρεύμα διαρροής (I) ως συνάρτηση της εφαρμοζόμενης τάσης (V) για όλα τα δείγματα παρουσιάζεται στο Figure 0.15. Το ρεύμα μετρήθηκε για ράμπες τάσης ξεκινώντας από τα $0V$ και πηγαίνοντας στα $+10V$ και πίσω στα $0V$ και στη συνέχεια στα $-10V$ και πίσω στα $0V$. Τα αποτελέσματα που παρουσιάζονται στο Figure 0.15 αποκαλύπτουν ότι το μέγεθος του ρεύματος διαρροής βρίσκεται στο κατώτατο όριο θορύβου του συστήματος μέτρησής μας, το οποίο είναι σχεδόν $5 \cdot 10^{-13}A$. Στη συνέχεια, μπορούμε να χρησιμοποιήσουμε τις διαστάσεις των δειγμάτων μας για να υπολογίσουμε την ειδική αντίσταση των εξεταζόμενων σύνθετων υλικών PLA. Με τον τρόπο αυτό, συμπεραίνουμε ότι η ειδική αντίσταση είναι μεγαλύτερη από $6 \cdot 10^{14}\Omega cm$ για όλα τα σύνθετα υλικά. Η τιμή αυτή είναι σύμφωνη με τις αναφορές για την ειδική αντίσταση όγκου του καθαρού PLA που κυμαίνονται από $5 \cdot 10^{14}\Omega \cdot cm$ [11] μέχρι $4 \cdot 10^{17}\Omega cm$ [12].

Μια άλλη ενδιαφέρουσα παρατήρηση σχετικά με το ρεύμα διαρροής είναι ότι υπάρχει υστέρηση των καμπυλών τάσης ρεύματος σε σχέση με την εφαρμοζόμενη πόλωση. Αυτή η υστέρηση πρέπει να οφείλεται στην παγίδευση φορτίου εντός του υλικού PLA. Είναι ενδιαφέρον ότι η προσθήκη SiC, φαίνεται να μειώνει την αντιληπτή παγίδευση χωρίς να αυξάνει το ρεύμα διαρροής και, συνεπώς, την ειδική αντίσταση όγκου του σύνθετου υλικού. Στην πραγματικότητα, η ειδική αντίσταση φαίνεται να μειώνεται με την αύξηση της περιεκτικότητας σε SiC, παρόλο που οι μετρήσεις είναι πολύ κοντά στο κατώτατο όριο θορύβου των οργάνων μας και η περιεκτικότητα σε SiC είναι μικρότερη από τις συνήθως αναφερόμενες περιεκτικότητες σε πρόσθετα [11], [12]. Πρέπει να τονίσουμε σε αυτό το σημείο ότι το SiC δεν είναι αγώγιμο υλικό, γεγονός που αποτελεί σημαντική διαφορά μεταξύ αυτών των περιπτώσεων και άλλων αναφερόμενων προσθέτων σε PLA στη βιβλιογραφία.

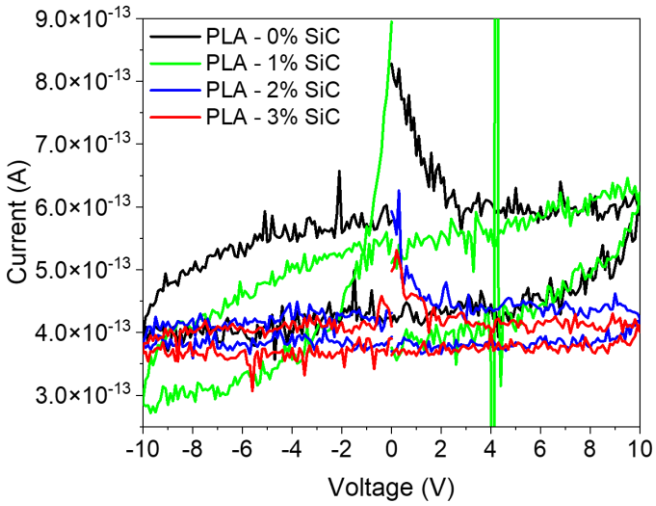

Figure 0.15 Ρεύμα διαρροής ως συνάρτηση της εφαρμοζόμενης τάσης για όλα τα δείγματα. Οι μετρήσεις πραγματοποιήθηκαν για εύρος τάσης από +10V έως 0V έως -10V έως 0V.

1.6 Χαρακτηρισμός Τριβογεννητριών

Οι τριβοηλεκτρικές νανογεννήτριες που χρησιμοποιήθηκαν στην παρούσα μελέτη λειτουργούν σύμφωνα με τη λειτουργία διαχωρισμού επαφής. Κυλινδρικά δείγματα, με διάμετρο 32 mm και πάχους περίπου 390 μm, εκτυπώθηκαν τρισδιάστατα χρησιμοποιώντας έναν τρισδιάστατο εκτυπωτή CREALITY CR20 Pro και τα προαναφερθέντα ντοπαρισμένα νήματα PLA και στη συνέχεια ακολούθησε στίλβωση των δειγμάτων.

Ως τριβοηλεκτρική επιφάνεια αναφοράς, ένα 75 μm-thick Kapton® layer (DuPont™) κόπηκε από ένα μεγάλο φύλλο σε διάσταση $2x2\ cm^2$. Κάθε τριβοηλεκτρική επιφάνεια τοποθετήθηκε σε εξαγωνικούς φορείς δειγμάτων PCB χρησιμοποιώντας αγώγιμη ταινία αλουμινίου διπλής όψης, συμπληρώνοντας ένα τριβοηλεκτρικό ζεύγος, όπως φαίνεται στο Figure 0.16. Οι πλακέτες φορέων PCB περιέχουν στην πίσω πλευρά τους ένα επίθεμα επαφής που παρέχει την ηλεκτρική επαφή για τις τριβοηλεκτρικές επιφάνειες.

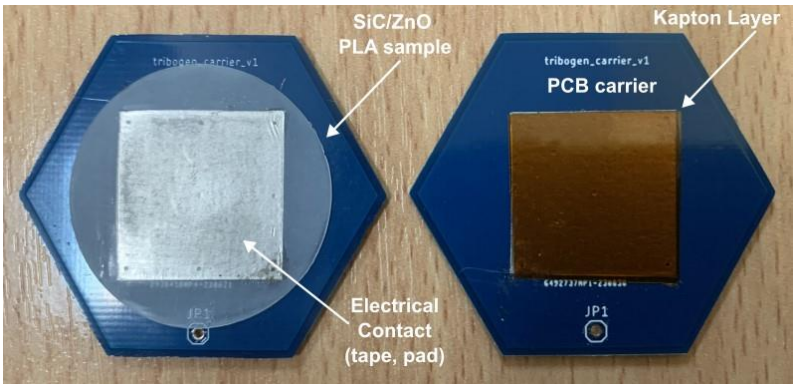

Figure 0.16 PCB για την τοποθέτηση των κατασκευασμένων υλικών και των μεμβρανών Kapton, που χρησιμοποιήθηκαν ως επιφάνεια αναφοράς, για τον τριβοηλεκτρικό χαρακτηρισμό.

Για τη διερεύνηση της απόδοσης εξόδου των TENGs με βάση το PLA πραγματοποιήθηκαν τέσσερις τύποι μετρήσεων: α) χρονικά εξαρτώμενη τάση εξόδου (transient), β) τάση ανοικτού κυκλώματος (Voc) και γ) ρεύμα βραχυκύκλωσης (Isc).

Για τις transient μετρήσεις χρησιμοποιήθηκε ο παλμογράφος InfiniiVision DSO7104A (Agilent Technologies). Οι μετρήσεις ρεύματος πραγματοποιήθηκαν με προενισχυτή ρεύματος χαμηλού θορύβου Stanford Research Systems SR570. Για την εκτίμηση της ισχύος ως συνάρτηση ενός εξωτερικού φορτίου καθώς και της τάσης ανοιχτού κυκλώματος εφαρμόστηκε η μεθοδολογία που αναπτύχθηκε από τους Jayasvasti et al. [13]. Για την περιοδική κίνηση των τριβοηλεκτρικών επιφανειών χρησιμοποιήθηκε το εσωτερικό σύστημα που παρουσιάζεται στο Figure 0.17.

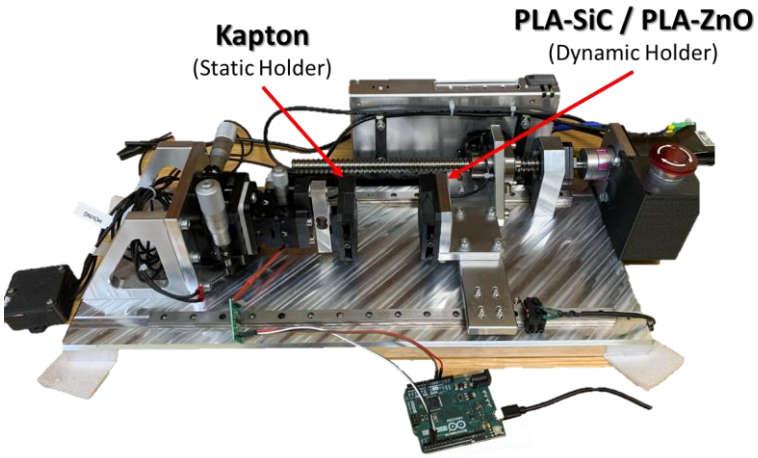

Figure 0.17 Το εσωτερικό σύστημα διαχωρισμού οριζόντιας επαφής.

1.6.1 SiC based tribogenerators

Στο Figure 0.18 (a) παρουσιάζεται το τριβοηλεκτρικό σήμα ως συνάρτηση του χρόνου για τα διάφορα TENGs με πρόσμιξη SiC. Παρατηρούμε ότι αρχικά το τριβοηλεκτρικό σήμα αυξάνεται από $11{,}3V$ για το καθαρό PLA σε $14{,}4V$ για το PLA που έχει προστεθεί με $1{,}5wt\%$ SiC. Ωστόσο, καθώς η συγκέντρωση SiC αυξάνεται σε $3wt\%$, το τριβοηλεκτρικό σήμα μειώνεται στα $10{,}5V$, το οποίο είναι συγκρίσιμο με την τιμή που λαμβάνεται για το μη ντοπαρισμένο PLA. Παρόμοια αποτελέσματα μπορούν να εξαχθούν από το Figure 0.18 (b), όπου παρουσιάζεται η εξάρτηση της παραγόμενης ισχύος σε συνάρτηση με το εξωτερικό φορτίο. Παρατηρούμε ότι η μέγιστη ισχύς που λαμβάνεται για το PLA με πρόσμιξη SiC $1{,}5wt\%$ είναι $26\mu W$ ($6{,}5\mu W/cm^2$, λαμβάνοντας υπόψη ότι η επιφάνεια των δειγμάτων είναι $4cm^2$), η οποία παρουσιάζει 2,5 φορές αύξηση σε σύγκριση με όλα τα άλλα δείγματα.

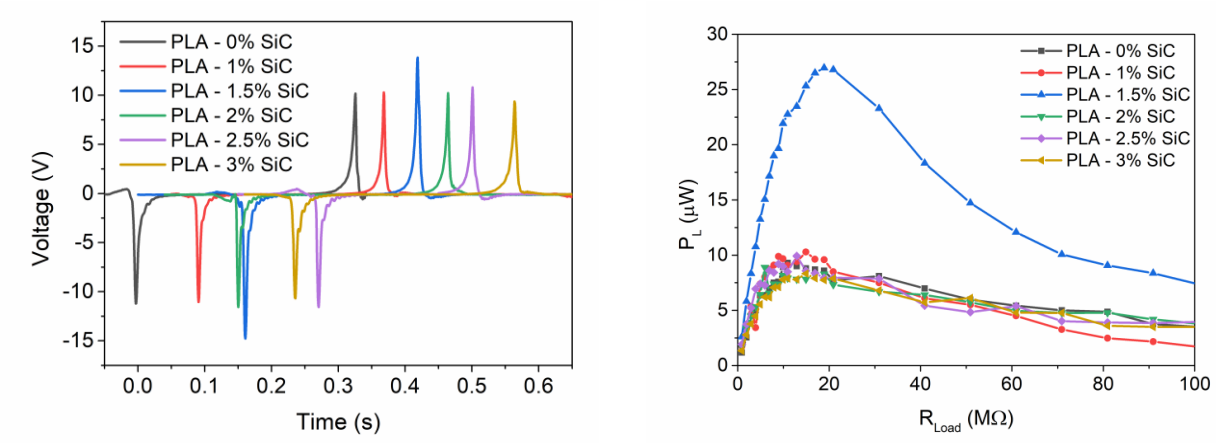

(α) **(β)**

Figure 0.18 (α) Τριβοηλεκτρικό σήμα τάσης εξαρτώμενο από το χρόνο και (β) ισχύς ως συνάρτηση του εξωτερικού φορτίου για τριβογεννήτριες με διαφορετικές συγκεντρώσεις SiC.

Το Figure 0.19 (a) δείχνει την τάση εξόδου σε συνάρτηση με το εξωτερικό φορτίο. Παρατηρούμε ότι το SiC με πρόσμιξη 1,5$wt\%$ εμφανίζει την υψηλότερη τάση ανοιχτού κυκλώματος που φτάνει την τιμή των $26V$. Παρόμοιο συμπέρασμα προκύπτει και από το Figure 0.19 , όπου παρουσιάζεται το ρεύμα της τριβογεννήτριας σε συνάρτηση με το εξωτερικό φορτίο. Παρατηρούμε ότι το ρεύμα βραχυκύκλωσης (σε μηδενικό εξωτερικό φορτίο) για το PLA με πρόσμιξη SiC 1,5$wt\%$ φτάνει τα $2\mu A$ ($500nA/cm^2$), το οποίο είναι υψηλότερο σε σύγκριση με όλα τα άλλα δείγματα.

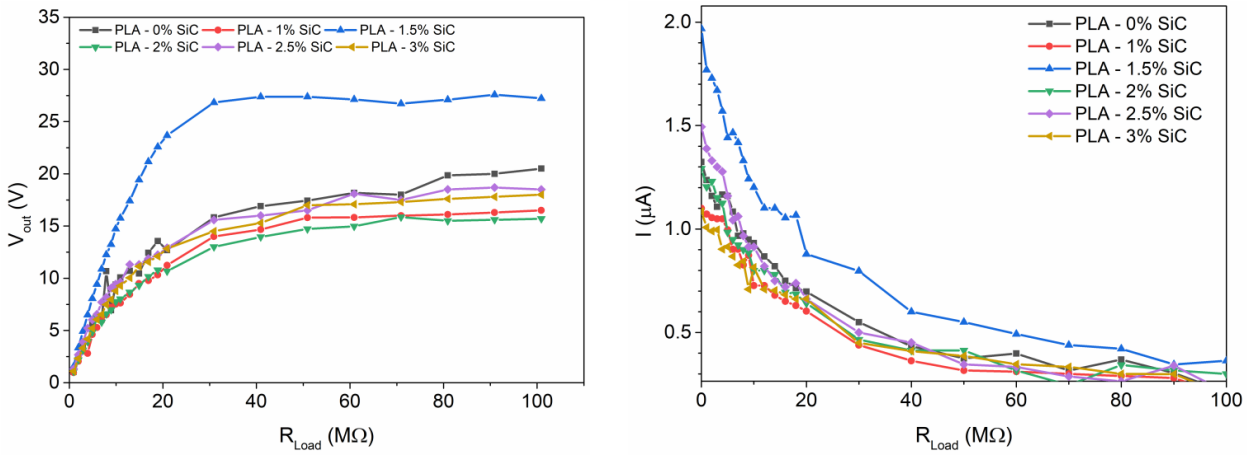

(α) **(β)**

Figure 0.19 α) Τάση ανοικτού κυκλώματος (Voc) και β) ρεύμα βραχυκύκλωσης (Isc) για τριβογεννήτριες με διαφορετική συγκέντρωση SiC.

1.6.2 ZnO based tribogenerators

Στο Figure 0.20 (a) παρουσιάζεται το τριβοηλεκτρικό σήμα ως συνάρτηση του χρόνου για τα διάφορα TENGs με πρόσμιξη ZnO. Παρατηρούμε ότι το τριβοηλεκτρικό σήμα αυξάνεται καθώς αυξάνεται η συγκέντρωση του ZnO φτάνοντας σε μια τιμή $40V$ όταν η συγκέντρωση του ZnO είναι 3$wt\%$. Παρόμοια αποτελέσματα μπορούν να εξαχθούν από το Figure 0.20 (b) όπου παρουσιάζεται η εξάρτηση της ισχύος της τριβοηλεκτρικής γεννήτριας σε συνάρτηση με το εξωτερικό φορτίο.

Παρατηρούμε ότι η μέγιστη ισχύς που λαμβάνεται για το PLA με πρόσμιξη $3wt\%$ ZnO είναι $80\mu W$ ($20\mu W/cm^2$), η οποία είναι περίπου 8 φορές υψηλότερη σε σύγκριση με το μη προσμιγμένο PLA.

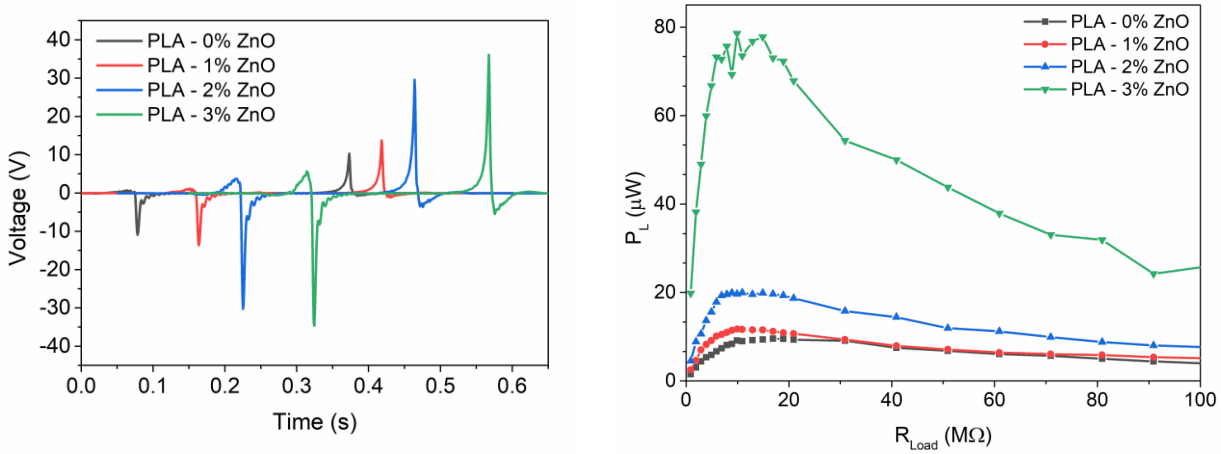

(α) **(β)**

Figure 0.20 α) Μεταβατικό σήμα ως συνάρτηση του χρόνου και β) ισχύς ως συνάρτηση του εξωτερικού φορτίου για τριβογεννήτριες με διαφορετική συγκέντρωση ZnO.

Το Figure 0.21 (a)δείχνει την τάση εξόδου σε συνάρτηση με το εξωτερικό φορτίο. Παρατηρούμε ότι το $3wt\%$ ντοπαρισμένο ZnO παρουσιάζει την υψηλότερη τάση ανοιχτού κυκλώματος που φτάνει την τιμή των $50V$. Παρόμοια αποτελέσματα προκύπτουν από το Figure 0.21 (b), όπου παρουσιάζεται το ρεύμα της τριβογεννήτριας σε συνάρτηση με το εξωτερικό φορτίο. Παρατηρούμε ότι το ρεύμα βραχυκύκλωσης για το PLA με πρόσμιξη $3wt\%$ ZnO φτάνει τα $2{,}2\mu A$ ($550nA/cm^2$), το οποίο είναι υψηλότερο σε σύγκριση με όλα τα άλλα δείγματα.

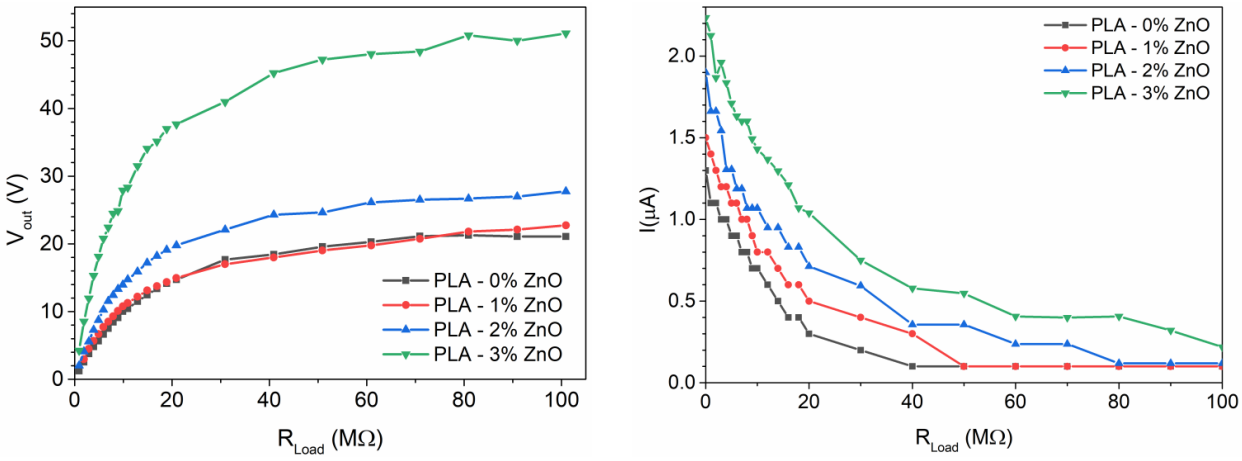

(α) **(β)**

Figure 0.21 (α) Τάση ανοικτού κυκλώματος (Voc) και (β) ρεύμα βραχυκύκλωσης (Isc) για τριβογεννήτριες με διαφορετική συγκέντρωση ZnO.

1.6.3 Συμπεράσματα

Για την καλύτερη κατανόηση των αποτελεσμάτων, παραπέμπουμε στη θεωρητική ανάλυση του Niu et al. [14]. Το Figure 0.22 δείχνει ένα σχηματικό διάγραμμα μιας τριβογεννήτριας που

αποτελείται από δύο διηλεκτρικές επιφάνειες και τα ηλεκτρόδια που είναι προσαρτημένα στην πίσω πλευρά των διηλεκτρικών. Η TENG λειτουργεί στη λειτουργία διαχωρισμού επαφής. Όταν οι δύο τριβοηλεκτρικές επιφάνειες βρίσκονται σε επαφή, στις επιφάνειες των διηλεκτρικών εμφανίζονται ηλεκτρικά φορτία αντίθετης πολικότητας, λόγω μεταφοράς φορτίου μεταξύ των δύο υλικών. Στην περίπτωσή μας η επιφάνεια του PLA φορτίζεται θετικά, ενώ η επιφάνεια του Kapton φορτίζεται αρνητικά, λόγω των διαφορών στις ηλεκτραρνητικότητες των δύο υλικών.

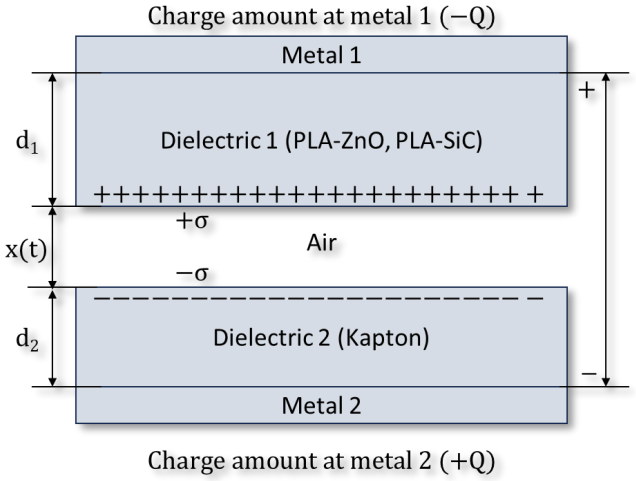

Figure 0.22 Σχηματικό της τριβοηλεκτρικής γεννήτριας σε λειτουργία διαχωρισμού επαφής.

Η τάση που αναπτύσσεται στη διάταξη δίνεται από τη σχέση V-Q-x:

$$V(t) = -\frac{Q}{S\varepsilon_0}[d_0 + x(t)] + \frac{\sigma x(t)}{\varepsilon_0} \qquad (0.3)$$

όπου Q είναι η ποσότητα του φορτίου στη μεταλλική επαφή, σ είναι η πυκνότητα του επιφανειακού φορτίου στην επιφάνεια των διηλεκτρικών, ε_0 είναι η διαπερατότητα του κενού, S είναι η επιφάνεια επαφής μεταξύ του τριβοηλεκτρικού ζεύγους και d_0 δίνεται από την εξίσωση:

$$d_0 = \frac{d_1}{\varepsilon_{r1}} + \frac{d_2}{\varepsilon_{r2}} \qquad (0.4)$$

Όπου d_1, d_2 και $\varepsilon_{r1}, \varepsilon_{r2}$ είναι τα πάχη και οι σχετικές διηλεκτρικές σταθερές των διηλεκτρικών στρωμάτων 1 και 2 αντίστοιχα. Στην περίπτωσή μας όπου το Kapton® χρησιμοποιείται ως ηλεκτρόδιο αναφοράς και το σύνθετο PLA ως ενεργό ηλεκτρόδιο, οι τιμές είναι:$d_1 = 75\mu m, \varepsilon_{r1} = 3, d_2 = 390\mu m$. Η τιμή για ε_{r2} εξαρτάται από το σύνθετο ντοπάρισμα.

Εναλλακτικά, η εξίσωση (0.3) μπορεί να γραφεί στη μορφή:

$$V(t) = -\frac{Q}{C_{TENG}} + V_{oc} \qquad (0.5)$$

όπου CTENG είναι η συνολική χωρητικότητα του TENG που δίνεται από την εξίσωση (0.6)

$$C_{TENG} = \frac{S\varepsilon_0}{[d_0 + x(t)]} \qquad (0.6)$$

Και V_{oc} είναι η τάση ανοικτού κυκλώματος όπως ορίζεται στην εξίσωση (0.7)

$$V_{oc} = \frac{\sigma \cdot x(t)}{\varepsilon_o} \qquad (0.7)$$

Το Figure 0.24 (a) δείχνει μια σύγκριση της τάσης ανοιχτού κυκλώματος V_{oc} και το ρεύμα βραχυκύκλωσης I_{sc} των TENGs με τις διάφορες συγκεντρώσεις SiC και ZnO. Βλέπουμε ότι καθώς αυξάνεται η συγκέντρωση SiC και ZnO η V_{oc} και το Isc ενισχύονται και στις δύο περιπτώσεις. Στην πραγματικότητα, για το PLA με πρόσμιξη SiC, V_{oc} και I_{sc} αυξάνονται κατά 42% και 48% αντίστοιχα σε σύγκριση με το μη ντοπαρισμένο PLA καθώς η συγκέντρωση αυξάνεται στο 1,5wt%, ενώ για το PLA με ντοπαρισμένο ZnO η αύξηση είναι 44% και 69% αντίστοιχα καθώς η συγκέντρωση αυξάνεται στο 2%. Παρόμοια συμπεριφορά παρατηρείται και για τη μέγιστη ισχύ με την αύξηση να είναι 280% και 188% αντίστοιχα.

Μια τέτοια συμπεριφορά μπορεί να αποδοθεί στη βελτίωση της χωρητικότητας/διηλεκτρικής σταθεράς του doped-PLA λόγω της εισαγωγής πληρωτικών υλικών (μικρο/νανοσωματίδια) με υψηλότερη διηλεκτρική σταθερά σε σύγκριση με το PLA [15]. Έχει αποδειχθεί ότι η συμπερίληψη πληρωτικών υλικών σε ένα διηλεκτρικό μπορεί να ενισχύσει το τριβοηλεκτρικό σήμα. Αυτό οφείλεται στο γεγονός ότι τα νανοσωματίδια με υψηλότερη διηλεκτρική σταθερά σε σύγκριση με τον ξενιστή, όταν διασκορπιστούν στη κύριο υλικό, θα λειτουργήσουν ως μικροπυκνωτές. Με την παρουσία ηλεκτρικού πεδίου, φορτίο θα συσσωρευτεί στη διεπιφάνεια των σωματιδίων, οδηγώντας σε διεπιφανειακή πόλωση και ενίσχυση της πυκνότητας επιφανειακού φορτίου του διηλεκτρικού στρώματος[16] όπως φαίνεται στην Figure 0.24.

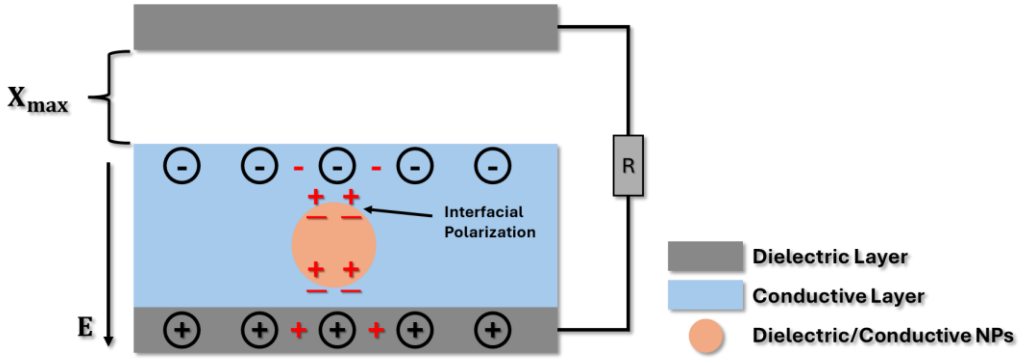

Figure 0.23 Schematic diagram of internal interface polarization in TENG dielectric layer thin films doped with dielectric/conductive nanoparticles, inspired from [16].

Επιπλέον, η παρουσία αυτών των σωματιδίων θα αυξήσει τις διηλεκτρικές ιδιότητες του σύνθετου υλικού. Έχει αποδειχθεί θεωρητικά ότι η συμπερίληψη σωματιδίων με υψηλότερη διηλεκτρική σταθερά από τη μήτρα υποδοχής, θα αυξήσει τη διηλεκτρική σταθερά, ανεξάρτητα από το σχήμα των σωματιδίων[17]. Οι αναφερόμενες τιμές για τη διηλεκτρική σταθερά του PLA κυμαίνονται από 2,5 έως 3,11 [7], [8], η οποία είναι πολύ χαμηλότερη σε σύγκριση με τη διηλεκτρική σταθερά του SiC που είναι σχεδόν 15 στη μορφή σκόνης του[9] και για τα νανοσωματίδια ZnO που είναι περίπου 10[18]. Από την υποενότητα 1.5 αποδείξαμε ότι η συμπερίληψη σωματιδίων SiC αυξάνει μονοτονικά τη διηλεκτρική σταθερά του σύνθετου υλικού φτάνοντας την τιμή 3,9 για το PLA με πρόσμιξη SiC 3wt%. Παρόμοια αποτελέσματα αναμένονται και για το PLA με πρόσμιξη ZnO. Αυτή η αύξηση της

διηλεκτρικής σταθεράς αύξησε σημαντικά την πυκνότητα των φορτίων που μπορούν να συσσωρευτούν στο συμπολυμερές κατά τη διάρκεια της φυσικής επαφής[19]. Από το Figure 0.24 (α) και λαμβάνοντας υπόψη την εξίσωση (0.6) μπορούμε να συμπεράνουμε ότι η πυκνότητα επιφανειακού φορτίου για τα δείγματα με πρόσμιξη 1,5wt% SiC και τα δείγματα με πρόσμιξη $3wt\%$ ZnO είναι αυξημένη σε σύγκριση με το μη προσμιγμένο PLA φθάνοντας σε τιμή $2{,}65\mu C/m^2$ και $4{,}86\mu C/m^2$ αντίστοιχα.

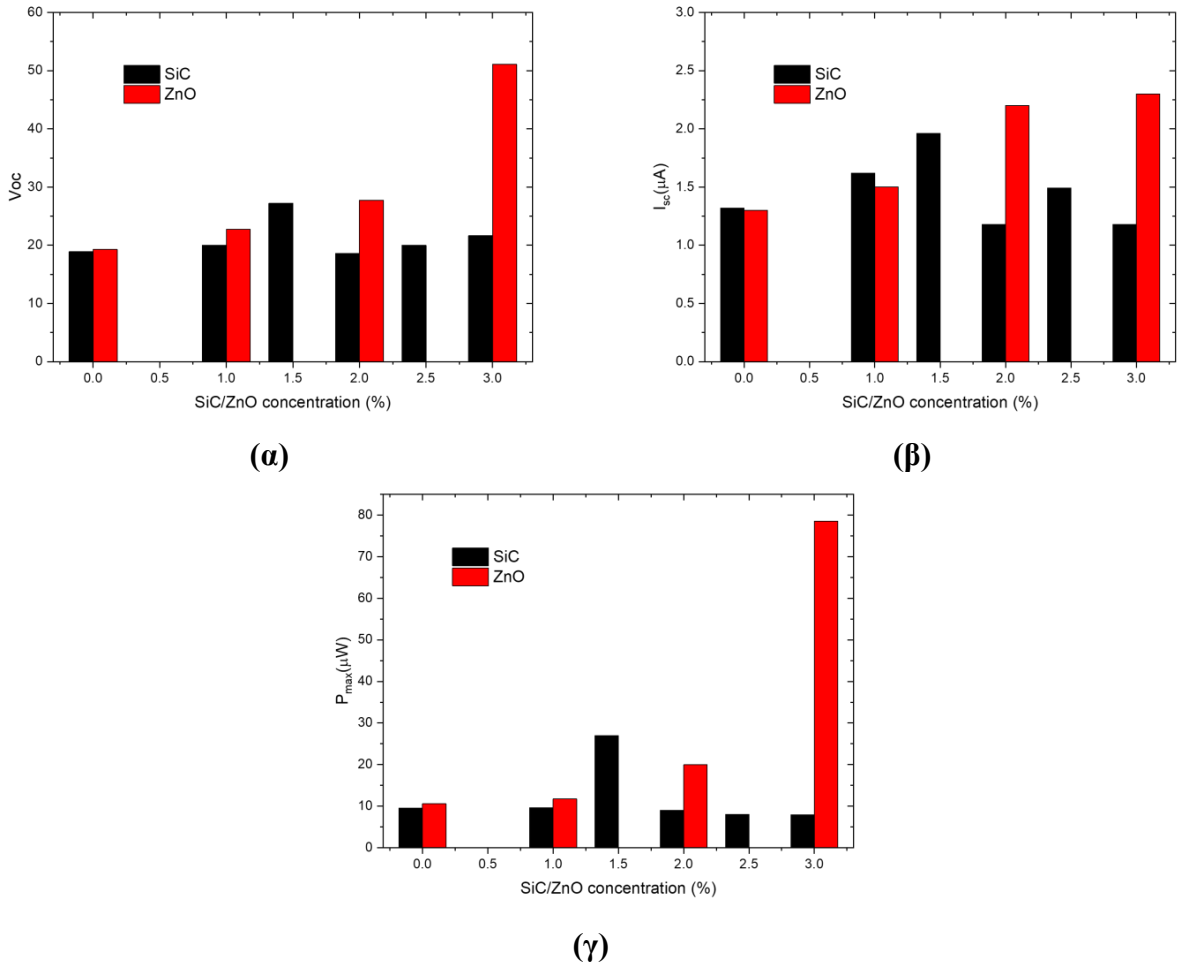

Figure 0.24 (α) Τάση ανοικτού κυκλώματος και (β) ρεύμα βραχυκύκλωσης και (γ) ισχύς των TENGs με τις διάφορες συγκεντρώσεις SiC και ZnO.

Ένα άλλο σημείο που παρατηρούμε από Figure 0.21 είναι η διαφορετική συμπεριφορά μεταξύ των υλικών με πρόσμιξη PLA. Παρατηρούμε ότι για τα δείγματα με προσθήκη ZnO το τριβοηλεκτρικό σήμα συνεχίζει να αυξάνεται καθώς η συγκέντρωση αυξάνεται στο $3wt\%$. Στην πραγματικότητα, η τάση ανοιχτού κυκλώματος, το ρεύμα βραχυκύκλωσης και η ισχύς εξόδου αυξάνονται κατά 265%, 177% και 741% αντίστοιχα, σε σύγκριση με το μη ντοπαρισμένο PLA.

Ωστόσο, το PLA με πρόσμιξη SiC συμπεριφέρεται με διαφορετικό τρόπο. Το τριβοηλεκτρικό σήμα φτάνει σε ένα μέγιστο (στο $1{,}5wt\%$ στην περίπτωσή μας) και στη συνέχεια μειώνεται καθώς η συγκέντρωση αυξάνεται στο $3wt\%$. Για να κατανοήσουμε καλύτερα αυτή τη συμπεριφορά, λαμβάνουμε υπόψη τους μηχανισμούς που επηρεάζουν το τριβοηλεκτρικό σήμα. Για τα ντοπαρισμένα δείγματα PLA, υπάρχουν δύο ανταγωνιστικοί μηχανισμοί που καθορίζουν το

τριβοηλεκτρικό σήμα: (α) το ντοπάρισμα με τα σωματίδια SiC και ZnO, τα οποία οδηγούν σε αύξηση του τριβοηλεκτρικού σήματος λόγω της αυξημένης διηλεκτρικής σταθεράς/χωρητικότητας των ντοπαρισμένων δειγμάτων PLA, όπως αναλύθηκε παραπάνω, και (β) η αύξηση της επιφανειακής τραχύτητας, η οποία οδηγεί σε μείωση του τριβοηλεκτρικού σήματος λόγω της μείωσης της ενεργού επιφάνειας επαφής μεταξύ των δύο τριβοηλεκτρικών επιφανειών. Όπως έχει προαναφερθεί, κατά την προετοιμασία τα δείγματα γυαλίστηκαν με λειαντικό χαρτί SiC για να μειωθεί η επιφανειακή τραχύτητα της τρισδιάστατα εκτυπωμένης επιφάνειας. Αυτό έχει ως αποτέλεσμα μια σχετικά χαμηλή τιμή της επιφανειακής τραχύτητας. Από τις μετρήσεις του οπτικού προφίλ, εκτιμούμε ότι το μέσο τετραγωνικό ύψος είναι μικρότερο από 0,3 μm. Ωστόσο, καθώς η συγκέντρωση του SiC στη μήτρα PLA αυξάνεται κατά 3wt%, η επιφανειακή τραχύτητα αυξάνεται κατά 33%, φθάνοντας σε τιμή 0,41 μm. Αυτό έχει ως αποτέλεσμα τη μείωση της επιφάνειας επαφής που οδηγεί σε μείωση του τριβοηλεκτρικού σήματος. Αντίθετα, για το PLA με προσθήκη ZnO, οι μετρήσεις οπτικού προφίλ δείχνουν ότι η ενσωμάτωση σωματιδίων ZnO στο PLA δεν επηρεάζει την επιφανειακή τραχύτητα. Αυτό μπορεί να αποδοθεί στο μικρότερο μέγεθος των νανοσωματιδίων ZnO καθώς και στο γεγονός ότι το ZnO είναι πολύ πιο μαλακό σε σύγκριση με το χαρτί λείανσης SiC.

Η μείωση του τριβοηλεκτρικού σήματος λόγω της αυξημένης επιφανειακής τραχύτητας συμφωνεί με τα βιβλιογραφικά αποτελέσματα. Kumar et al.[20] διερεύνησαν την επίδραση της τυχαίας πολυδιάστατης επιφανειακής τραχύτητας στο τριβοηλεκτρικό σήμα των TENGs. Οι εν λόγω ερευνητές ανέπτυξαν TENGs με βάση διαφανή μίκα σε επαφή με πολυβινυλοσιλοξάνιο (PVS) με διαμορφωμένη επιφανειακή τραχύτητα. Με τη βοήθεια μιας νέας in situ οπτικής τεχνικής, μπόρεσαν να εκτιμήσουν άμεσα την επιφάνεια επαφής ως συνάρτηση της τραχύτητας. Παρατήρησαν ότι, καθώς αυξανόταν η τραχύτητα, αυξανόταν και το τριβοηλεκτρικό σήμα καθώς και η απόδοση εξόδου του TENG, λόγω της μείωσης της πραγματικής επιφάνειας επαφής. Παρόμοια αποτελέσματα προέκυψαν από τους Wen et al.[21] οι οποίοι διερεύνησαν, τόσο θεωρητικά όσο και πειραματικά, ένα TENG διαχωρισμού επαφής αγωγού-διηλεκτρικού για την ανίχνευση της τραχύτητας των επιφανειών υλικών. Η μείωση του τριβοηλεκτρικού σήματος για SiC με πρόσμιξη PVDF έχει επίσης αναφερθεί στη βιβλιογραφία από τους Shafeek et al.[22]. Οι εν λόγω ερευνητές διερεύνησαν την επίδραση των νανοσωματιδίων SiC στις τριβοηλεκτρικές ιδιότητες ενός νανοσύνθετου υλικού από φθοριούχο πολυβινυλίδιο (PVDF) / καρβίδιο του πυριτίου (SiC). Έδειξαν ότι το τριβοηλεκτρικό σήμα μπορεί να ενισχυθεί σημαντικά σε σύγκριση με το παρθένο PVDF καθώς η συγκέντρωση του SiC αυξάνεται έως και 6%. Ωστόσο, για υψηλότερες συγκεντρώσεις (9%) η απόδοση της συσκευής τείνει να μειώνεται. Απέδωσαν αυτή τη μείωση στη συσσωμάτωση των νανοσωματιδίων SiC στην επιφάνεια των μεμβρανών PVDF με αποτέλεσμα τη μείωση της επιφάνειας επαφής μεταξύ του PVDF και του πολυαμιδίου που χρησιμοποιήθηκε ως υλικό αναφοράς.

Chapter II
English Version

2 Introduction

Triboelectric energy harvesting has emerged as a critical alternative method for converting the abundant mechanical energy that surrounds us into useful electricity that can power electronic devices and systems. Following the discovery of the triboelectric nanogenerator (TENG) by Zhong Lin Wang's team [1], there has been an exponential increase in research activity around efficient triboelectric energy harvesting using various materials and technologies [2], [3], [4]. The ability of triboelectricity and electrostatic induction to work with almost any combination of materials highlights the challenge of finding ideal materials to maximize the triboelectric response. The emergence of 3D printing [5] as a cost-effective manufacturing process, which allows the production of a variety of structures with minimal material waste and shortens production time, makes it reasonable to develop triboelectric devices based on this technology for self-powered electronic systems[6].

Polylactic acid (PLA), a recyclable, biocompatible and biodegradable natural thermoplastic material produced from renewable resources, is widely used in the manufacture of triboelectric devices. In this work, we develop PLA-based triboelectric nanogenerators and analyze the influence of SiC and ZnO nanoparticles on their performance.

2.1 Energy Demand

The global energy landscape is undergoing a significant transformation, driven by the dual imperatives of reducing carbon emissions and meeting the growing energy demand of a burgeoning global population. This chapter delves into the anticipated energy market size by 2030, the role of nanotechnology in advancing electronic devices, the integration of the Internet of Things (IoT) in smart cities, and the deployment of sensors for optimizing renewable energy sources.

The global renewable energy market is on a trajectory of robust growth, projected to reach a valuation of USD 2182.99 billion by 2030, growing at a compound annual growth rate (CAGR) of 8.50% from 2023 to 2032. This growth is underpinned by a concerted push towards sustainable energy sources, driven by governmental policies, technological advancements, and increasing environmental awareness. The Asia Pacific region is expected to dominate the market, fueled by rapid industrialization, urbanization, and supportive government initiatives[23].

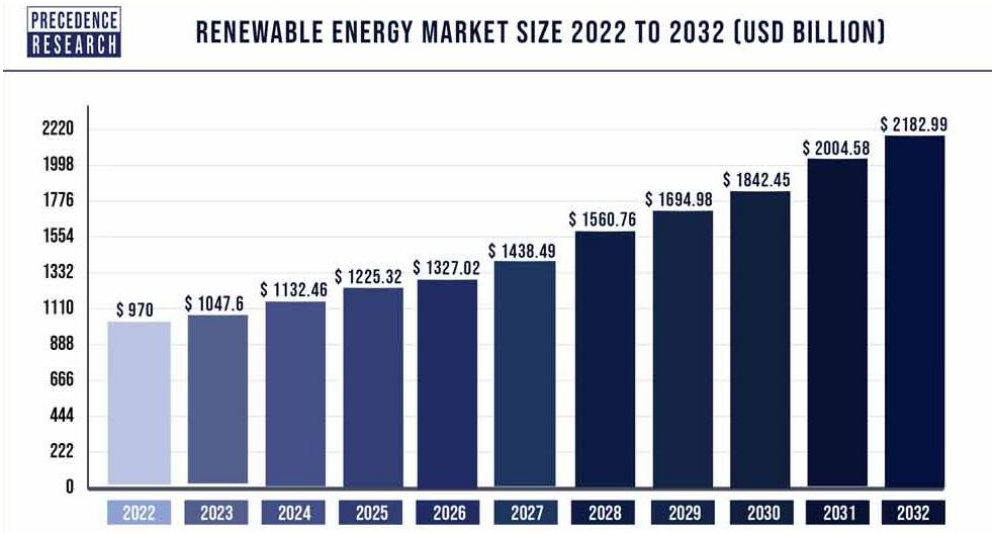

Figure 2.1 Renewable Energy Market Size 2022 to 2023 (USD) [23].

Nanotechnology is poised to revolutionize electronic devices, making them faster, smaller, and more energy efficient. By manipulating materials at the molecular or atomic level, nanotechnology enables the development of devices with enhanced functionalities and performance. For instance, nanoelectronics, leveraging materials like graphene and carbon nanotubes, promises to significantly improve the density of memory chips and reduce the size of transistors used in integrated circuits. This advancement is crucial for the energy sector, as it leads to the creation of more efficient energy storage systems and solar panels, thereby supporting the broader adoption of renewable energy sources.

Energy harvesting presents a compelling solution to these challenges. By capturing energy from ambient sources such as light, radio frequencies, and mechanical vibrations, energy harvesting technologies can power IoT sensors without the need for conventional batteries. This approach not only reduces the environmental footprint associated with battery use but also extends the operational lifespan of IoT devices, minimizing maintenance and replacement costs.

For instance, RF energy harvesting, as discussed in the study on Zero Energy IoT Devices in Smart Cities, demonstrates how IoT devices can be powered by harvesting energy from radio frequency signals, enabling a self-sustaining ecosystem of wireless sensors within urban settings[24], [25].

Similarly, energy harvesting mechanisms reviewed in the context of smart cities highlight the diversity of available sources, including mechanical vibration, electromagnetic induction, and electrostatic energy, which can be harnessed to power IoT applications seamlessly integrated into the urban fabric.

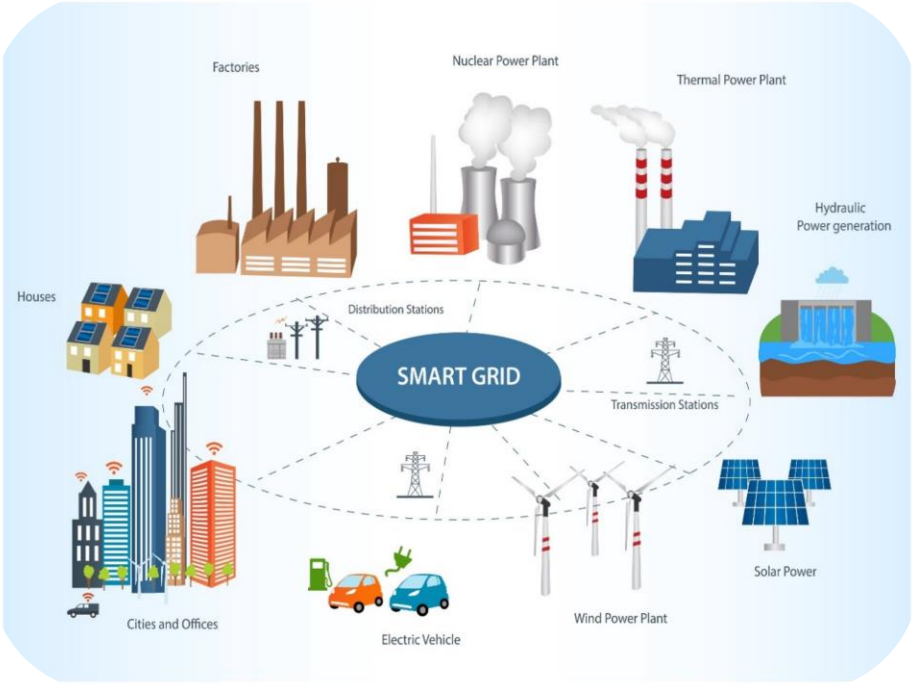

Figure 2.2 IoT smart grid applications for intelligent urban computing [26].

As we approach 2030, the global energy market is set to expand significantly, with renewable energy at its core. Nanotechnology, IoT, and sensors are instrumental in this transition, offering innovative solutions to enhance the efficiency, reliability, and sustainability of energy systems. In order to advance the promising fields of WSNs and the Internet of Things, especially the IoT devices needed to complete intelligent cities, a variety of ambient energy sources exist in the human environment and might be studied. This work discusses the common sources of energy that can be collected. Energy is easily obtained near the application because it is present practically everywhere there are natural sources such as vibrations, daylight, heat, wind, radio frequency, water, or any other type of naturally existing source. By doing this, it will be ensured that the EH plans for the shining city reap all of its benefits, such as minimal maintenance costs and quick answers to multiple requests from various city zones. The synergy between these technologies and renewable energy sources not only addresses the growing energy demand but also propels us towards a more sustainable and environmentally friendly future.

2.2 Energy Harvesting

The new 5G and big data era, marked by the rapid expansion of wearable and portable electronics, has been brought about by the development of the Internet of Things (IoT) and wireless data transmission systems. Consequently, the spread of dispersed Internet of Things sensor nodes that integrate with our bodies and surroundings is changing the way we traditionally interact with the outside world. For instance, tactile and pressure sensors are incorporated into gloves, socks, and mats to detect human gestures and motions in order to build human-machine interfaces and humidity and gas sensors are placed in both wearable and portable devices to furnish information related to human motion and healthcare.

The dynamo, created in 1831 by Michael Faraday and able to transform kinetic energy into electrical energy, was one of the earliest examples of energy harvesting in use. Nonetheless, the development of the water and windmills is likely where energy collecting got its start. The scientific community has been interested in energy harvesting ever since. These days, energy conservation and the use of renewable resources have drawn increased funding and attention from researchers to make society more ecologically friendly.

The good news is that there are many different types of abundant energy available to us in our surroundings. For example, human kinetic energy, wind energy, thermal energy, solar energy, etc., can all be transformed into electrical energy through the use of hybrid architectures that power distributed wireless sensor nodes in phases using electrostatic, electromagnetic, piezoelectric, thermoelectric, pyroelectric, triboelectric, and photovoltaic effects, as illustrated in Figure 2.3 [27].

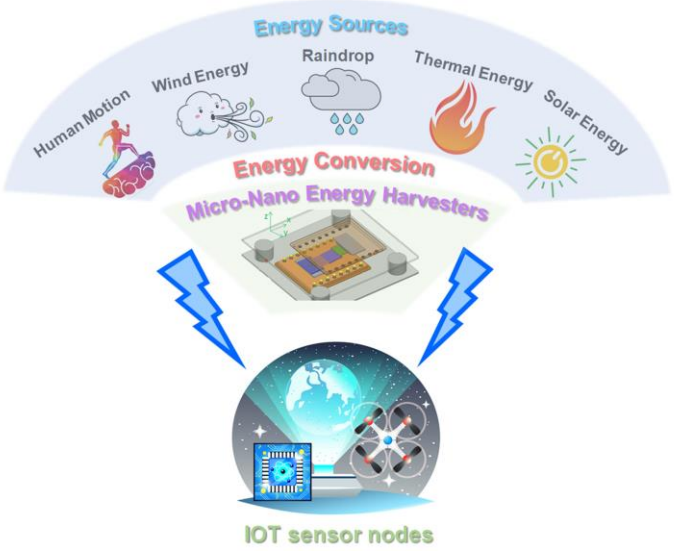

Figure 2.3 An overview of the various energy sources that can be used to power self-sufficient systems using various energy conversion techniques [27].

Today, to be more environmentally friendly, renewables and energy saving have gained more attention and resources at the research level. Moreover, the recent development of microelectronic technology has managed to reduce energy requirements, making renewable sources (wind, hydrothermal, solar, etc.) viable options as primary energy sources. More broadly, the term energy harvesting recommends the creation of energy autonomous electronic devices to operate a variety of wireless applications. Energy harvesting is the process of collecting and modifying any form of energy derived from the environment into a source of electrical energy. Common energy harvesting systems include car tire pressure monitors, wireless weather stations, implantable medical devices, traffic alert signals, Mars nodes, WSN (Wireless Sensor Network) nodes, IoT (Internet of Things) devices, etc.

There is an abundance of energy available in the environment in different forms, which can be harnessed to create an energy self-sufficient device as shown in Figure 2.4. The main forms of energy are:

- Mechanical energy in the form of vibrations, stresses and deformations, e.g. air movement, waves at sea, etc.
- Thermal energy from furnaces, combustion engines and other heat sources.
- Electromagnetic energy in the form of solar radiation or RF (radio frequency) radiation.
- Human energy from metabolic activities within the human body, even at rest.

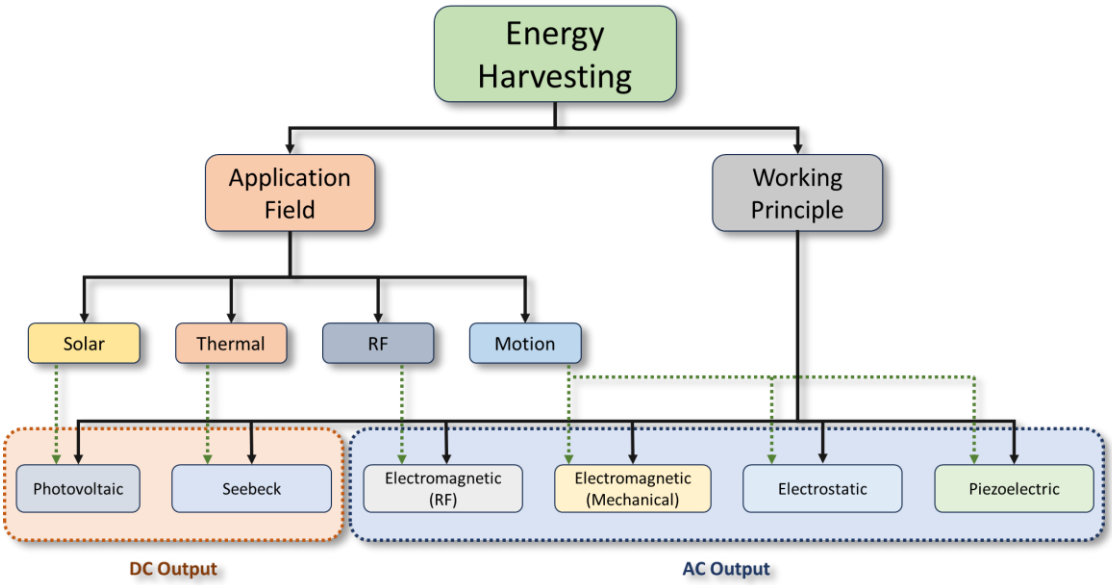

Figure 2.4 Tree of the principles and fields of energy harvesting applications (Inspired from [28]*).*

The energy from the energy sources mentioned above can be captured and converted into electrical voltage and current, depending on the requirements of low-power electronic devices and WSNs applications.

2.2.1 Energy Harvesting Systems

Energy harvesters, on the other hand, have been the subject of years of scientific literature as essential parts that can be incorporated into sensor nodes to realize energy conversion [40]. Significant progress has been achieved in raising their energy output under various conditions. Microelectromechanical system (MEMS) technology has advanced rapidly since the mid-1900s. This has led to the development of a number of miniaturized sensors that are used in environmental monitoring, healthcare, and industrial automation. Additionally, MEMS electrostatic, electromagnetic, thermoelectric, and piezoelectric energy harvesters are among the miniaturized energy harvesters that have been produced. The advantages of these MEMS, or microscale energy harvesters, include their tiny size, ease of mass manufacture, and compatibility with wearable and portable electronics. However, in 2012, the group of Prof. Z. L. Wang developed the triboelectric nanogenerator (TENG) as an example of a nanoscale energy harvester, based on contact

electrification and electrostatic induction. Since then, there has been a great deal of interest in TENG research all over the world, with numerous studies focusing on different aspects of this technology, including energy density, structural improvements, stability, biocompatibility, surface modification, circuitry design, and overall system integration. TENG is a promising biomechanical energy collecting power source for wearable and implanted electronic devices because of its broad range of accessible materials. Micro-nano energy harvesters are a potential technology for low-power distributed IoT sensor nodes, even though their energy production is not as high as that of conventional large-scale energy harvesters. Firstly, micro-nano energy harvesters can be directly integrated into Internet of Things sensor nodes due to their tiny size. Moreover, different ambient fragmented energies can be converted into electrical energy by micro-nano energy harvesters, enabling IoT sensor nodes to function. Finally, micro-nano energy harvesters may be mass-produced to fulfill the energy requirements of large IoT sensor nodes due to their low fabrication costs.

Depending on the type, quantity, and source of energy being transformed into electrical energy, energy harvesting can take many various forms. In its most basic configuration, the energy harvesting system needs the following three essential parts in addition to an energy source, such as heat, light, or vibration.

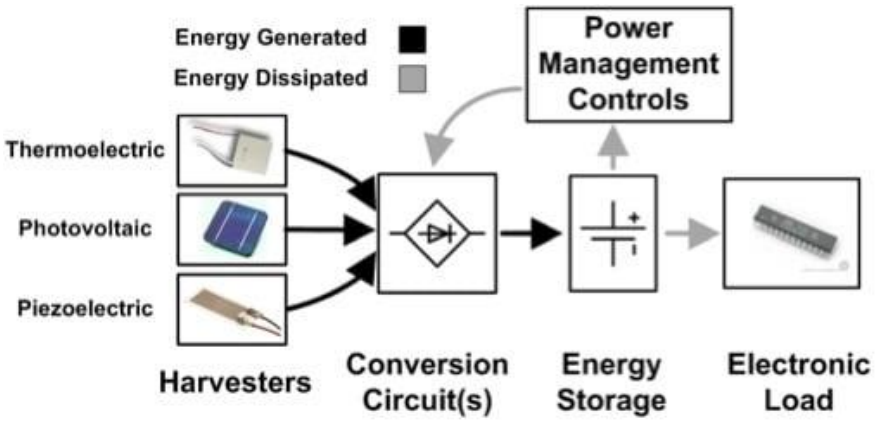

Figure 2.5 Basic Components of an energy harvesting system.

The basic components of an energy harvesting system are:

- Transducer/harvester: This is the energy harvester that collects and converts the energy from the source into electrical energy. Typical transducers include photovoltaic for light, thermoelectric for heat, inductive for magnetic, RF for radio frequency, and piezoelectric for vibrations/kinetic energy.
- Energy storage: Such as a battery or super capacitor.
- Power management: This conditions the electrical energy into a suitable form for the application. Typical conditioners include regulators and complex control circuits that can manage the power, based on power needs and the available power.

3 Triboelectric Generators

3.1 Introduction

Static electricity is a phenomenon known since antiquity that usually occurs when two surfaces rub together or come into contact and move apart. This phenomenon is usually due to the transfer of charges from one surface to the other, or to the polarization of atoms or molecules, depending on the nature of the materials being rubbed. The result of this process is the appearance of a charge that is uniformly distributed if it is a conductor or localized in the friction area in the case of non-conductive materials. Static electricity has always been an undesirable phenomenon because it can cause serious accidents and disasters. These are due to the electrical discharges caused when there is a potential difference with the charged surface, making the phenomenon very dangerous in industrial environments where the risk of ignition is real.

In order to prevent ignition, vehicles transporting combustible or volatile chemicals must also be appropriately discharged. Additional instances include static loads produced by airplanes during flight that obstruct radio frequency transmission. Static charges have the potential to harm integrated circuits (CMOS) and transistors (MOSFETs) on a lesser scale. However, because the induced current is extremely brief and safe for humans, it is not a particularly threatening occurrence when we come into close contact with it daily. Industry and technology have conducted a considerable deal of study to reduce these phenomena and improve the safety of their applications because they are believed to have only negative impacts. Modern scientific research, however, has reinterpreted the significance of these electrostatic events by emphasizing their practicality and potential for future usage. This chapter goes over the triboelectric effect and how it can be used to create triboelectric nanogenerators that can produce the energy needed to run an independent system. The kinds of materials that might make good candidates for building these kinds of nanogenerators are also mentioned, along with the four main modes of operation.

The research group of Zhong Lin Wang (Georgia Tech) developed the first triboelectric nanogenerator (TENG), which was reported in January 2012 [1]. Additionally, this was the first attempt to use the triboelectric phenomenon and electrostatic induction to transform small-scale mechanical energy into electrical energy. When compared to other generators, triboelectric nanogenerators' ability to function at low frequencies is their most significant characteristic. This enables the energy from low frequency movements—such as walking, sea waves, air movement, and human body movements—to be harvested. These movements are commonly available but also lost every day.

3.2 Triboelectric Effect

The triboelectric effect is the most common reason for the occurrence of static electricity. The phenomenon is based on the contact of dissimilar surfaces, a charge donor and a charge acceptor. When the two materials come into contact, charges are transferred from one material to the other, and as the two surfaces separate, each material retains the electrical charge isolated from the gap between them. If an external electrical charge (e.g. a resistor) is connected between the two electrodes located at the edges of the surfaces, then a current flow will occur in order to balance the charges.

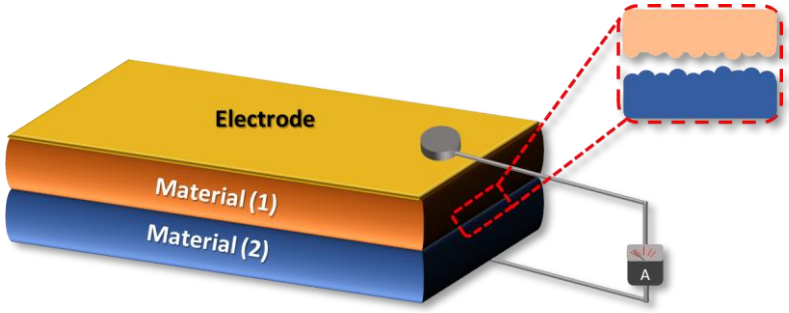

Figure 3.1 Contact of triboelectric surfaces and connection of electrodes to a load.

Structures that exploit the triboelectric effect and are used as charging sources are called triboelectric generators. The first devices to exploit the triboelectric effect were the Wimshurst machine and Van De Graaf generator.

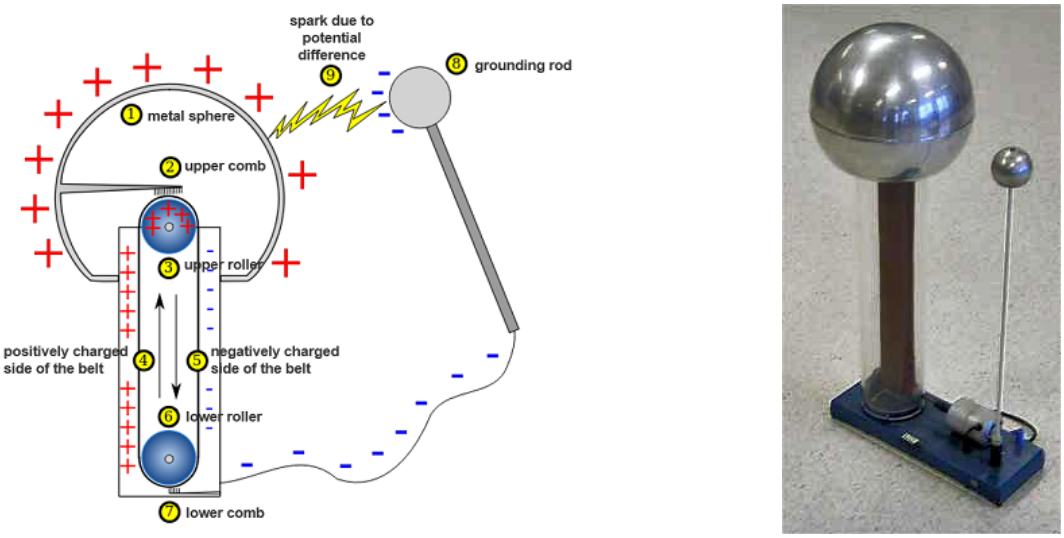

Figure 3.2 The Van de Graaff generator and its working mechanism.

This generator basically consists of an electric motor that drives a rubber belt which in turn drives insulated pulleys. The positive and negative charge generated is collected by the scallops located on the lower and upper pulleys. A polished metal ball surrounds the upper collection pulley and accumulates the charge on the ball. The sphere is mounted on a cylindrical insulating base that supports the pulley system. This device is capable of generating a potential of many kilovolts but is

not capable of generating electricity in a usable form. Its application is limited to scientific demonstrations such as electrostatic attraction, simple particle acceleration, etc.

3.2.1 Triboelectric Series

The transfer of electrons from one surface to another, in relation to the different materials chosen to exploit the triboelectricity effect, depends on their electrical polarity. Depending on how positively or negatively charged they are, materials are charged appropriately, i.e., it is determined which material will become negatively charged and which positively charged, based on their propensity to accept or reject electrons. Some materials have a stronger tendency to retain electrons than others, just as there are materials that seem to expel electrons more readily. An assessment of this potential for materials is shown in Figure 3.3 through a defined triboelectric series for a variety of materials.

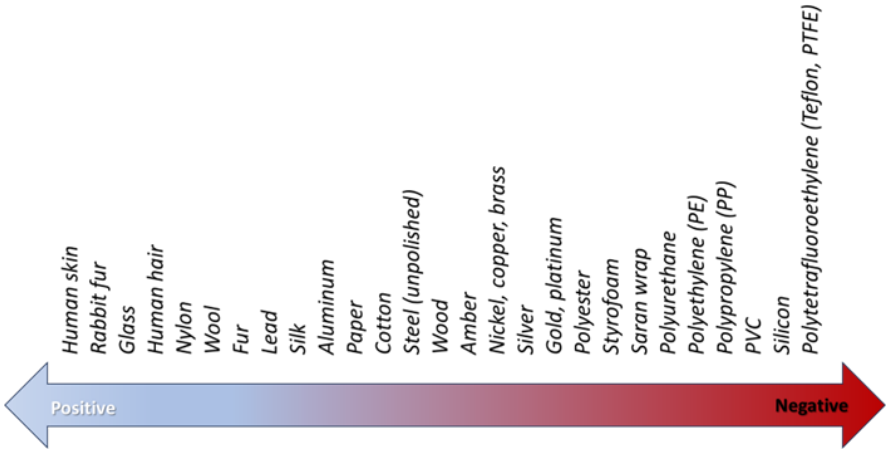

Figure 3.3 Triboelectric series for some commonly materials following a tendency of easy losing electrons(positive) to gaining electrons(negative).

The triboelectric series ranks different materials according to their tendency to gain or lose electrons. It usually lists materials in order of decreasing voltage of positive charge (losing electrons) and increasing voltage of negative charge (gaining electrons). In the middle of the list are materials that exhibit neither of these two behaviors. Due to the complexity of experiments involving controlled loading of materials, the research obtains tentative results in terms of determining the classification of a material in the triboelectric series. This fact results from the multitude of factors and conditions that affect the tendency of a material to be loaded. The selection of materials according to the triboelectric series is relevant as the triboelectric surfaces are modified in various ways to achieve optimum performance. In particular, the material of which a surface is composed can be chemically modified using nanowires, nanoparticles, nano cubes, etc. in order to increase the triboelectric charges. It is also possible for the surfaces to undergo changes in their morphology. That is, the uniform surface structure is modified, forming relief areas which exhibit different behavior on contact. In conclusion, the chemical and surface structure of the materials of triboelectric surfaces is an important factor in determining the potential difference developed, the dielectric constant of the materials and therefore the electrostatic induction.

3.2.2Operating Principle of Triboelectric Nanogenerators

Tribogenerators work on the basis of the combination of electrostatic induction and electrical contact. The primary process that transforms mechanical energy into electrical energy is electrostatic induction, which also produces statically polarized charges when electrical contact occurs. We deduce that tribogenerators inherently display capacitive behavior as electrostatic induction is a hallmark phenomenon of a capacitor. Charges transfer from one material to the other to balance their electrochemical potential when two distinct materials come into contact. This process is known as adhesion and occurs when specific portions of the two surfaces form a chemical connection. The transferred charges may consist of molecules, ions, or electrons. As the bonded atoms separate, some of them keep their excess electrons, while others tend to shed them, which could lead to frictional charges on the surfaces. The movement of electrons to the electrode to balance the growing potential difference is facilitated by the presence of triboelectric charges on the dielectric surfaces.

The working principle of TENGs, in terms of chemical bonds, is based on the phenomenon of adhesion. When two surfaces come into contact with each other, a chemical bond is formed on some parts and thus charges, electrons molecules or ions, move from one surface to the other in order to balance their electrochemical potential. When the surfaces separate, the surfaces do not electrically return to their original state. Some of the atoms in the materials retain the electrons they bound upon attachment, while others tend to remove them, thus creating triboelectric charges on the surfaces. It is the presence of these charges that is the fundamental phenomenon to which the operation of TENGs is due, since the triboelectric charges are responsible for the transfer of electrons to the electrons attached to the surfaces in order to balance the potential difference that develops.

Existing circuit models describing a tribo-generator arrangement are based on the parallel plate capacitor model. The behavior of a capacitor describes an electric field perpendicular to an infinitely charged field such as resulting from Gauss's law.

$$E = \frac{\sigma}{2\varepsilon} \qquad (3.1)$$

Whereas σ represents the surface's charge density and the parameter ε indicates the surface's electrical permeability, E is the uniform electric field created in a direction perpendicular to the charging surface. The electric charge between two opposing charged surfaces will double between the two charged surfaces, but it will be zero between the outside surfaces. This phenomenon explains the typical behavior of a normal capacitor, which holds electrical charges with opposite polarity when voltage is supplied to its electrode's polarity. However, the electrodes that react to the induced charges are linked to the opposite sides of the contact surfaces, but the surfaces that undergo the triboelectric effect are those that are in contact. Consequently, the electric field is transferred through the dielectric layers' thickness and is charged by the induced free charges at the dielectric-electrode contact. However, since these regions are not situated between the frictionally charged surfaces, the infinitely charged plane theory states that the total electric field acting within the dielectric layers

and on the dielectric-electrode interfaces must be zero. Consequently, the polarization of dielectrics and the induction of free charges on a tribogenerator's electrodes cannot be completely explained by the traditional parallel plate capacitor model, which describes infinitely charged planes.

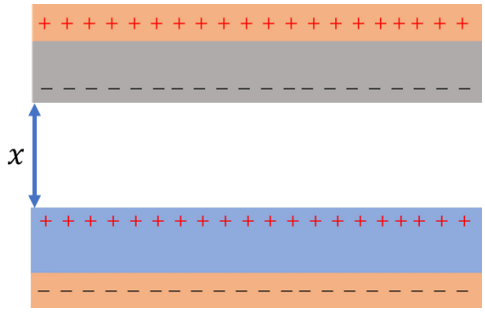

Figure 3.4 Arrangement of triboelectric surfaces and development of electrical charges on the surfaces.

In a typical friction generator structure, the spacing x (Figure 3.4) between the surfaces varies with the mechanical force applied to the surfaces. The result of the contact between the materials is the generation of opposing surface static loads. Then, upon separation of the surfaces the Q charges will transfer from one electrode to the other to create a charge of opposite polarity on the two electrodes, $+Q/-Q$. Therefore, the potential difference that occurs between the electrodes can be described as the superposition of two different potential values. The first value characterizes the potential difference of the polarized triboelectric charges $V_{OC}(x)$, the second potential value denotes the Q charges already transferred between the electrodes. As mentioned above in the case where no triboelectric charges were developed the structure would be a simple capacitor with voltage $\frac{Q}{C(x)}$ where $C(x)$ is the capacitance between the electrodes. In conclusion, the fundamental equation describing the potential difference in any tribogenerator structure is obtained as:

$$V = \frac{|Q|}{C(x)} + V_{oc}(x) \qquad (3.2)$$

However, depending on the distance between the surfaces, the structure of the materials and the movement way of the surfaces, equation (3.4) takes more complex forms for the expression of the potential difference developed at the electrodes of the structure in question.

3.2.3Methods of Operation

The development of triboelectric nanogenerators (TENGs) is divided into four fundamental modes of operation involving both the relative motion and the type of materials used. The modes of operation of TENGs are:

- Vertical Contact- Separation Mode (VC-Separation Mode)
- Lateral Sliding Mode
- Single Electrode Mode
- Freestanding Triboelectric- Layer Mode

Figure 3.5 schematically illustrates each of the triboelectric-layer modes of operation of the triboelectric generator.

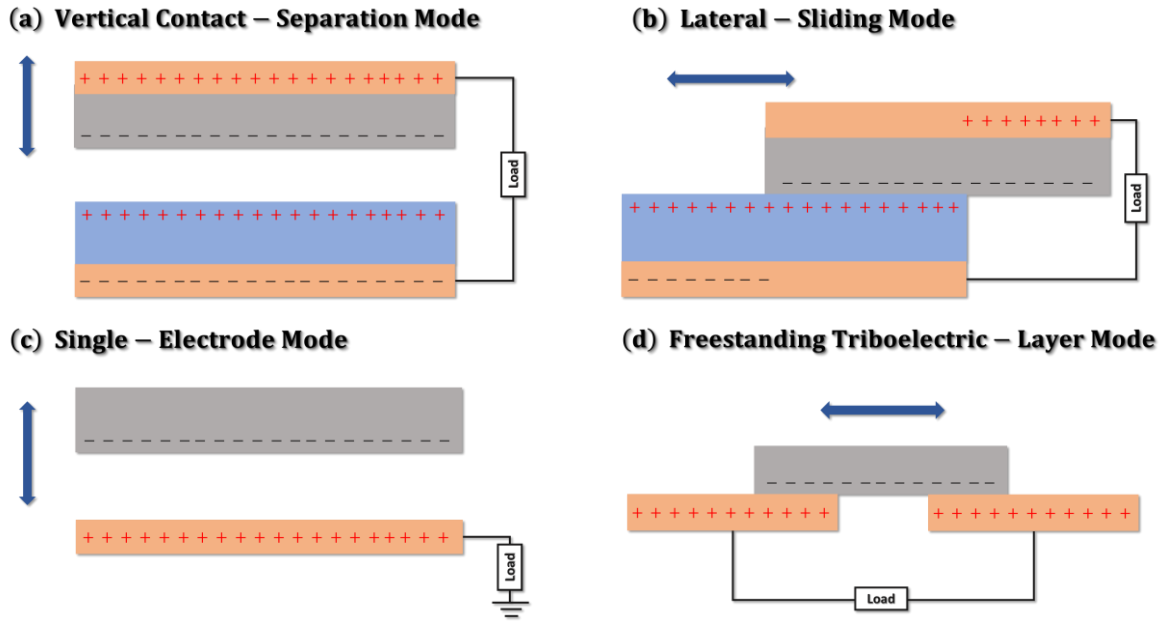

Figure 3.5 The four basic modes of operation of triboelectric nanogenerators: (a) Vertical contact-separation mode operation (b) Lateral-sliding mode operation (c) Single-electrode mode operation (d) Freestanding triboelectric-layer mode.

In this thesis, the vertical contact mode is used and will be described in more detail in the following chapters.

3.2.3.1 Vertical Contact-Separation Mode

In this mode of operation (vertical contact- separation mode) the tribogenerator consists of two surfaces of different dielectric material facing each other and two electrodes on the upper and lower side of the resulting device. The two dielectrics come into contact and charges of opposite sign are generated on their surfaces[29]. Their removal by the external mechanical force will create a potential difference. To balance this potential difference from the triboelectric charges, free electrons will flow between the electrodes[1].

Figure 3.6 and Figure 3.7 show the operation of a triboelectric nanogenerator with a vertical contact-separation arrangement for the two cases of open- circuit and short-circuit respectively. In the initial position (a) the two dielectrics are at a distance from each other and are therefore uncharged and there is no potential difference. A vertical external force causes them to come into vertical contact. Then, and according to the triboelectric series table, one dielectric will acquire a positive surface charge and the other a negative one. Due to the insulating properties of the dielectrics, the surface charge developed will be uniform over their entire area [14]. Also, dielectrics in their entirety have the ability, when charged, to maintain their surface charge for quite a long time.

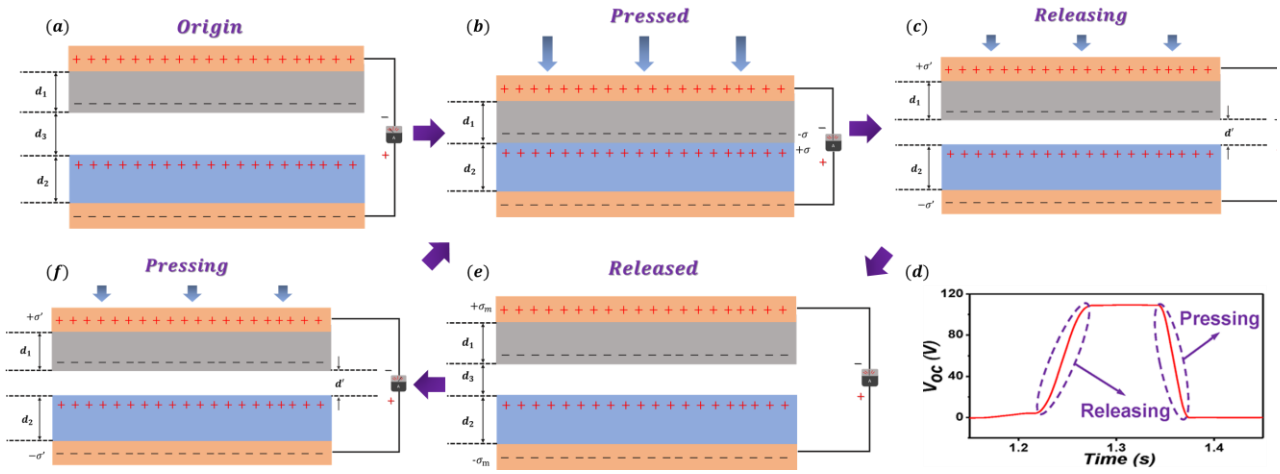

Figure 3.6 Operating principle of the generator in vertical contact-separation mode (open-circuit Voltage). (Image inspired from [30])

Because the charging takes place only on the friction surface of the dielectrics and because the developing charges are equal and opposite, no potential difference will occur as long as the dielectrics are in full contact Figure 3.6 (b). With the separation of the surfaces, the potential difference between the electrodes also occurs under open circuit conditions Figure 3.6 (b). The open-circuit voltage V_{oc} will continue to increase until the pairs return to the original removal position. The resistance of the multimeter to which the device is connected shall be infinite so that no voltage drop is observed across it. Consequently, the potential difference will decrease when the dielectric surfaces immediately come back into contact with each other, resulting in its zeroing at full contact Figure 3.6 (f). In the case of short-circuiting the two electrodes, movement of the free electrons in the potential difference state will be observed in the first removal, and the opposite movement of the electrons in their re-contact. When full contact of the dielectrics occurs, the induced charges on the electrodes are neutralized.

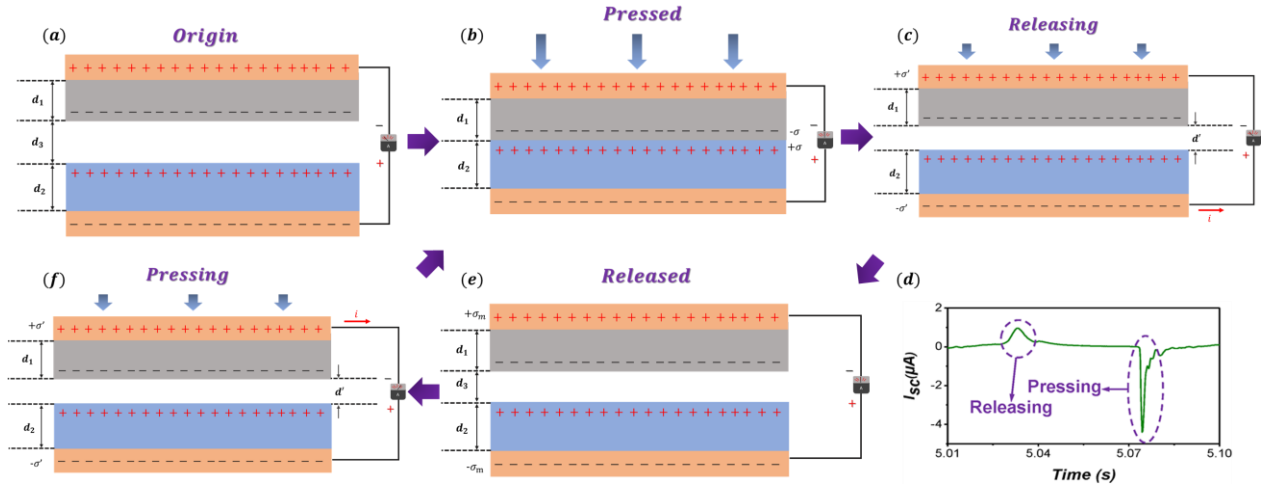

Figure 3.7 Operating principle of the generator in vertical contact-separation mode (short-circuit current). (Image inspired from[30])

The most important theoretical equation for explaining the real-time power generation of a TENG is the relationship between three parameters: the separation distance (x) between the two triboelectric charged layers, the voltage (V) between the two electrodes, and the amount of

transferred charge (Q) between them [14]. This relationship is known as the $V-Q-x$ relationship. Depending on the materials utilized for the triboelectric pairs, the contact-mode TENG is mainly divided into two categories: dielectric-to-dielectric and conductor-to-dielectric types.

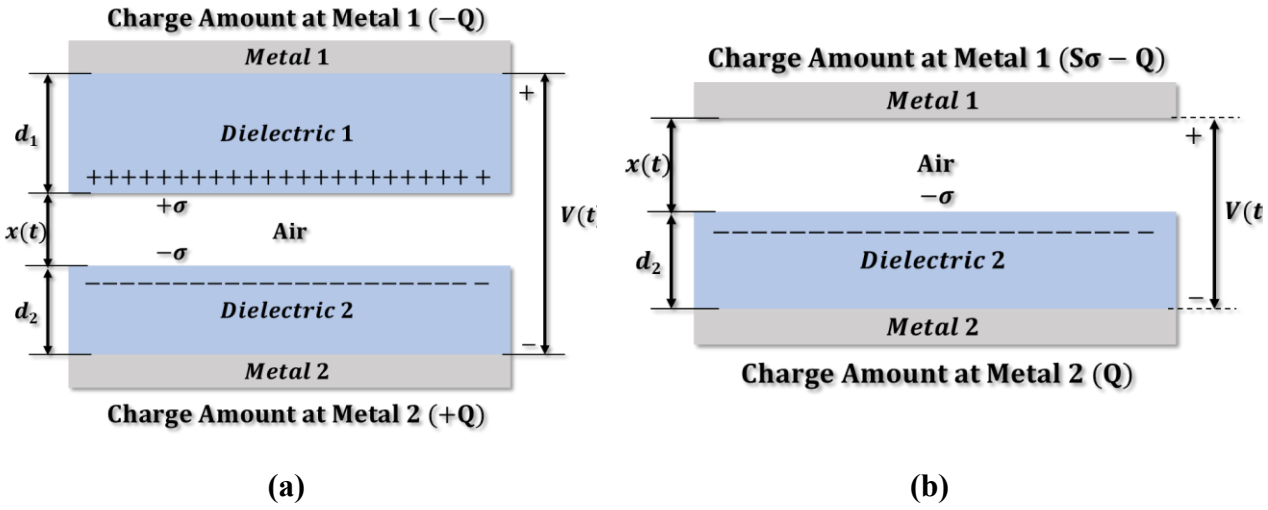

Figure 3.8 Theoretical models for (a)dielectric-to-dielectric contact-mode TENG and (b)conductor-to-dielectric contact-mode TENG. (Inspired from [14]*)*

As shown in the Figure 3.8, the two dielectrics with thickness d_1 and d_2 and relative dielectric constant ε_{r1} and ε_{r2} respectively are located opposite each other. On their outer sides metal layers have been deposited to play the role of electrodes. The distance (x) between them varies under the influence of an external force. Their inner sides, after contact, will develop equal and opposite surface charges σ. Because they are insulators, these triboelectric charges will be evenly distributed on their surface. Their removal, i.e., increasing (x) will create the observed potential difference and force the movement of the free electrons of the electrodes. This results in the electrodes gaining a charge which is denoted Q as defined in a previous paragraph.

Therefore the instantaneous charge of each electrode will be $+Q$ and $-Q$ correspondingly. The relationship between the electrodes' voltage V, induced charge Q, and separation (x) between the dielectrics is the most significant equation that can explain how this tribogenerator works. The electrostatics laws provide the basis for this relationship, which is known as the $V-Q-x$ equation. We can assume that the electrodes have infinite dimensions because their size S is significantly larger than the distance between them ($d-1.+, d-2.+x$), always in respect to the experimental approach. We can assume that there is a uniform distribution of charges on the electrodes because of this assumption. Similar to a capacitor, the electric field between the dielectrics and the air gap will also include a component whose direction is perpendicular to the surface. Gauss's theorem implies that the following relations determine the electric field at any given point:

Inside Dielectric 1:

$$E_1 = -\frac{Q}{S\varepsilon_0\varepsilon_{r1}} \qquad (3.3)$$

Inside the air gap:

$$E_{air} = \frac{-\frac{Q}{S} + \sigma(t)}{\varepsilon_0} \quad (3.4)$$

Inside Dielectric 2:

$$E_2 = -\frac{Q}{S\varepsilon_0\varepsilon_{r2}} \quad (3.5)$$

The voltage between the two electrodes can be given by

$$V = E_1 d_1 + E_2 D_2 + E_{air} x \quad (3.6)$$

Substituting the equations (3.3)-(3.5) into equation (3.6), the $V - Q - x$ relationship for the dielectric-to-dielectric TENG in vertical contact-mode is given by

$$V = -\frac{Q}{S\varepsilon_0}\left(\frac{d_1}{\varepsilon_{r1}} + \frac{d_2}{\varepsilon_{r2}} + x(t)\right) + \frac{\sigma x(t)}{\varepsilon_0} \quad (3.7)$$

The active thickness constant d_0 as the sum of the thickness of the individual dielectrics between the electrodes to their respective relative dielectric constants. This is

$$d_0 = \frac{d_1}{\varepsilon_{r1}} + \frac{d_2}{\varepsilon_{r2}} \quad (3.8)$$

So, the $V - Q - x$ relation for the TENGs can be defined as

$$V = -\frac{Q}{S\varepsilon_0}\big(d_0 + x(t)\big) + \frac{\sigma x(t)}{\varepsilon_0} \quad (3.9)$$

The following are the relations describing the characteristic parameters of the tribogenerators.

The voltage as obtained for Open Circuit Voltage V_{oc}

$$V_{oc} = \frac{\sigma x(t)}{\varepsilon_0} \quad (3.10)$$

The transferred charges at short circuit condition where $V = 0$ are given by

$$Q_{sc} = \frac{S\sigma x(t)}{d_0 + x(t)} \quad (3.11)$$

$$I_{sc} = \frac{S\sigma d_0 v(t)}{\big(d_0 + x(t)\big)^2} \quad (3.12)$$

And the Capacitance can be given by

$$C = \frac{Q_{sc}}{V_{oc}} = \frac{\varepsilon_0 S}{d_0 + x(t)} \quad (3.13)$$

3.2.3.2 Lateral Sliding Mode

For the description of this mode we consider a tribogenerator of a structure similar to that of the vertical contact-separation mode. The two surfaces are subjected to a horizontal force and parallel sliding occurs resulting in triboelectric charges. The transverse polarization that develops along the

slip contributes to the flow of electrons across the two electrodes of the materials in order to compensate for the field created by the triboelectric charge [31].

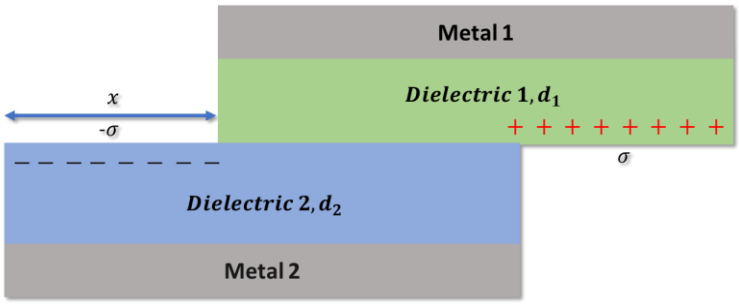

Figure 3.9 Lateral Sliding Mode.

The amount of charge transferred to the electrodes will be Q. The equation $V - Q - x$ can be derived by making the assumptions that the length l is greater than the thickness of the dielectrics d_1 and d_2 and that the lateral displacement x is less than $0.9l$ to ensure the parallelism of the plates. To do this, the capacitance $C(x)$ must be calculated. The capacitance between the overlapping regions will be the dominant component of the total capacitance since the thickness of the dielectrics is sufficiently less than the length until they are completely separated. The equation is derived from that for a capacitor with parallel armature:

$$C = \frac{\varepsilon_0 w(1-x)}{d_0} \quad (3.14)$$

Where d_0 is the active thickness constant. The open circuit V_{oc} voltage will be calculated by simultaneously calculating the load distribution. With minimal error we can consider the metal plates infinite which ensures that the load distribution will be uniform. In addition, the surface loading in non-overlapping regions is defined as σ. In overlapping regions the surface density is assumed to be zero. The ideal load distribution for each region will be: For the non-overlapping area on the bottom electrode:

$$\rho = \sigma \quad (3.15)$$

For the overlapping area on the lower electrode:

$$\rho = -\frac{\sigma x}{1-x} \quad (3.16)$$

For the non-overlapping area of the upper electrode:

$$\rho = -\sigma \quad (3.17)$$

For the overlapping area of the upper electrode:

$$\rho = \frac{\sigma x}{1-x} \quad (3.18)$$

So the $V - Q - x$ relation for the lateral-sliding friction generator will be the following:

$$V = -\frac{1}{C}Q + V_{oc} = -\frac{d_0}{w\varepsilon_0(1-x)}Q + \frac{\sigma d_0 x}{\varepsilon_0(1-x)} \quad (3.19)$$

3.2.3.3 Single-Electrode Mode

In cases where it is not possible to electrically connect any of the parts of the tribogenerator to the load, the single-electrode method is applied. The equivalent electrical circuit corresponding to the method describes the electrode of the device grounded. If the size of the device is finite, then placing or removing material in the device causes a change in the distribution of the electric field generated during electron flow. The single-electrode method can be performed in vertical and parallel configurations. The determination of $V - q - x$ is similar in form to the sliding lateral and vertical contact-separation modes, except that the structure consists of a dielectric surface (Figure 3.10). Therefore, the difference is geometric as the thickness of the single dielectric surface is omitted[1].

Vertical Operation

$$V = \frac{Q}{S \cdot \varepsilon_0}\left(\frac{d_2}{\varepsilon_{r2}} + x(t)\right) + \frac{\sigma x(t)}{\varepsilon_0} \qquad (3.20)$$

Parallel Operation

$$V = \frac{Q}{w(l-x)\varepsilon_0}\left(\frac{d_2}{\varepsilon_{r2}}\right) + \frac{\sigma x}{\varepsilon_0 (l-x)}\left(\frac{d_2}{\varepsilon_{r2}}\right) \qquad (3.21)$$

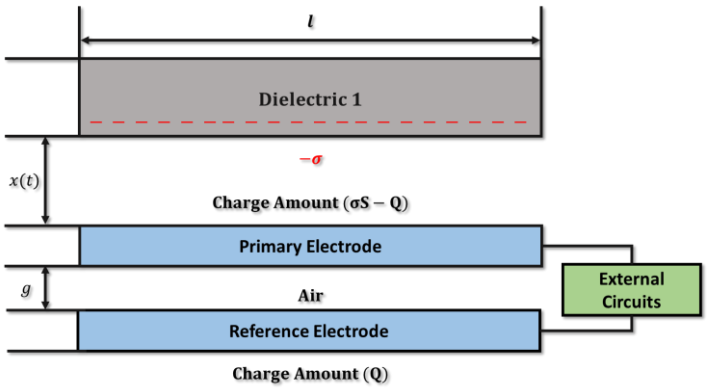

Figure 3.10 Vertical single electrode operation with the electrode grounded through a circuit element.

3.2.3.4 Freestanding Triboelectric- Layer Mode

A moving object in the environment, such clothing or shoes, is typically charged by contact with the ground, air, or other things. Hours can pass while electrical charges are on the surface without needing to come into touch with anything or cause friction.

A dielectric surface and two symmetrical electrodes make up this technique. The electrodes' breadth and the spaces between them lie in the same plane as the item in motion. The flow of electrons between the electrode surfaces is caused by an asymmetric charge that forms on the material surfaces while the object is in motion. Because of the oscillatory mobility of the electrons, an alternating output is created between the two electrodes. Furthermore, free rotation is allowed without the need for any mechanical contact because the moving object's surface is not in direct

touch with the upper dielectric surface of the electrodes or subjected to direct friction. Furthermore, the dielectric material's surface remains unchanged[1].

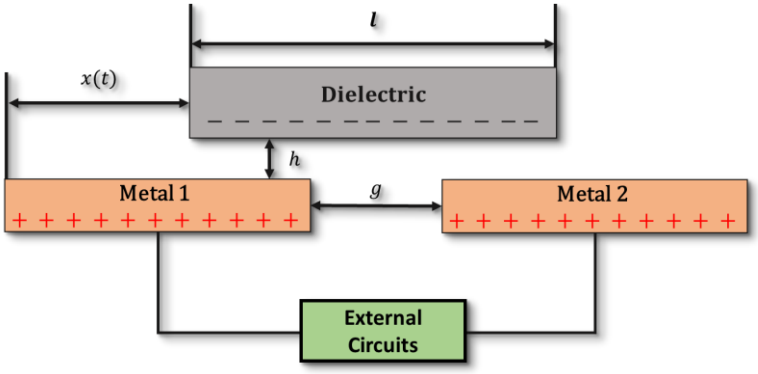

Figure 3.11 Freestanding Triboelectric- Layer Mode Function.

3.2.4Applications

Since 2012, when the first triboelectric nanogenerator was developed, a multitude of tribogenerators have been developed to harness energy from the movement of the human body, from various vibrations, wind and sound movement, water movement, as well as tribogenerators for autonomous systems and sensors.

Below are examples of the various applications of triboelectric nanogenerators as developed to present.

3.2.4.1 Harvesting Body Motion Energy

Ryu et al. [32] made commercial coin battery-sized high-performance inertia-driven tribo electric nanogenerator (I-TENG) based on body motion and gravity. They demonstrated that the enclosed five-stacked I-TENG converts mechanical energy into electricity at $4.9\mu W/cm^3$.

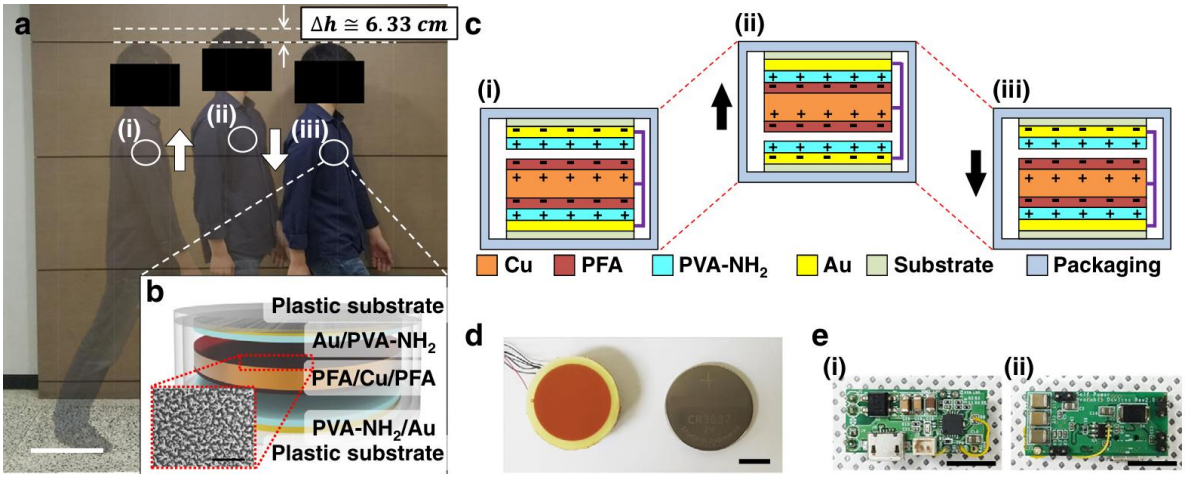

Figure 3.12 (a) image of a walker with a ~6 cm vertical displacement. the 30-cm scale bar. (b) The surface SEM picture of the surface-modified PFA layer and the schematic image of the I-TENG. the 5μm scale bar. (c) The I TENG's standalone unit's operating mechanism. (d) Image showing a commercial

coin battery and stacked I-TENG.. (e) Images of the power management system's 1 centimeter scale bar [32].

3.2.4.2 Harvesting Vibration Energy

Lee et al [33] created a multi-modal human emotion recognition system that combines data on verbal and non-verbal expressions to effectively use comprehensive emotional information. This system consists of a customized skin-integrated facial interface (PSiFI) system, which is easy to use, flexible, transparent, triboelectric strain, and vibration sensor. For the first time, this system allows us to sense and combine data on both spoken and nonverbal expressions.

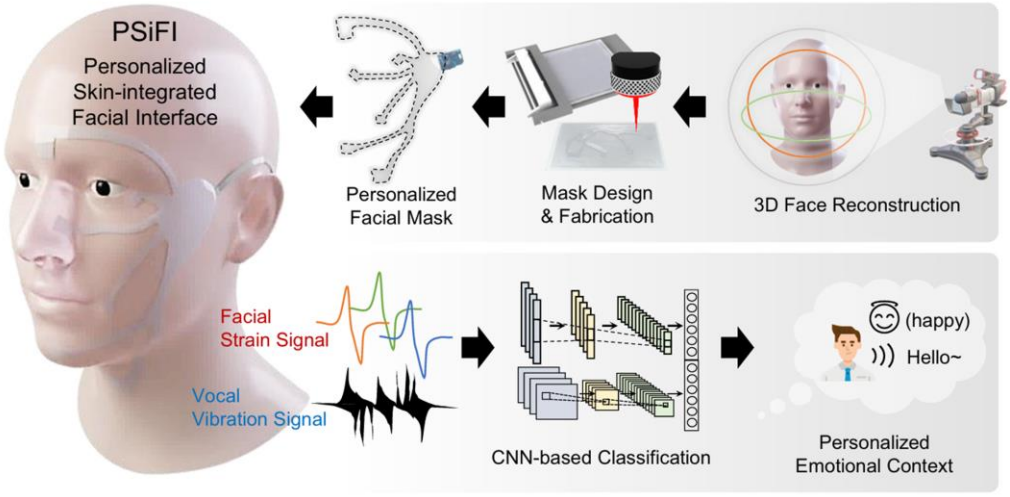

Figure 3.13 A schematic representation of a customized skin-integrated facial interface (PSiFI) that incorporates deep learning classifier for speech and facial expression detection, data processing circuit for wireless communication, and triboelectric sensors (TES) [33] .

3.2.4.3 Harvesting Wind Energy

Gao et al. [34] created a structure-based triboelectric-electromagnetic- piezoelectric hybrid generator (SS-TEPG) with the innovative strategy appropriately integrates suspension and damping structure for jointly achieving high efficiency wind and vibration energy harvesting with vibration attenuation function, consisting of a wind-driven triboelectric-electromagnetic hybrid generator (WD-TEHG), a vibration-driven piezoelectric energy generator and damper (VD-PEGD), and a spring-based energy dissipation structure.

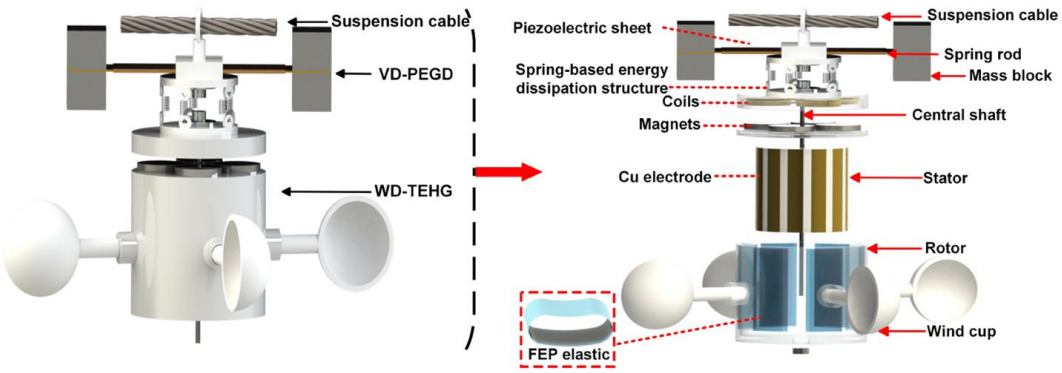

Figure 3.14 Diagrammatic construction of the hybrid generator made up of the WD-TEHG and VD-PEGD [34].

3.2.4.4 Harvesting Blue Energy

Gao et al. [35] presented a novel idea that seeks to create a wave-energy harvesting protective layer in order to turn wave scouring damage into chances for improving marine structure protection technologies. Based on its essential function in inhibiting ion diffusion, this innovative protective layer combines an X-shaped triboelectric nanogenerator (X-TENG) with a surface protection coating, efficiently buffering wave forces and turning wave energy into electric energy.

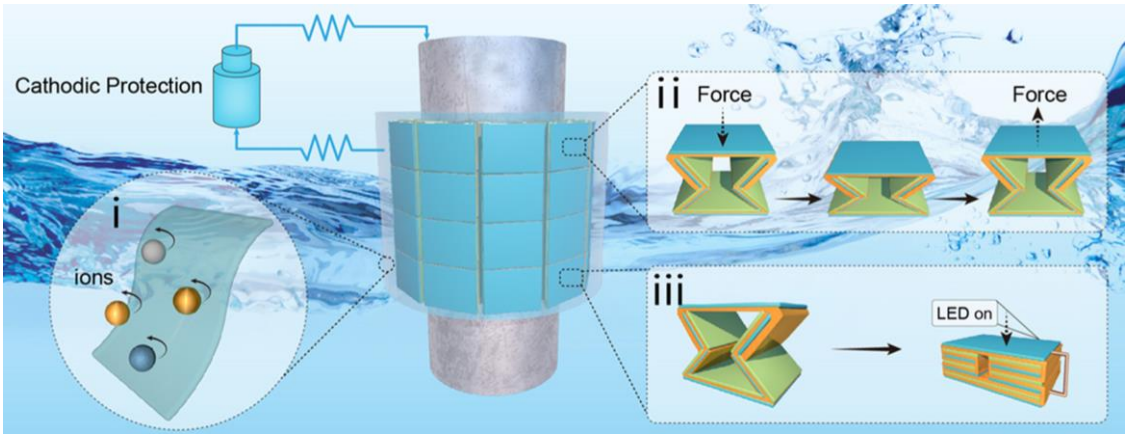

Figure 3.15 Design and fabrication of the X-TENG and the multifunction protective layer, and the function of the multifunctional protective layer [35].

3.2.4.5 Applications in Self-Powered Systems and Processes

A large-area multiplexing self-powered untethered triboelectric electronic skin (UTE-skin) with an ultralow misrecognition rate is provided by Shao et al. [34]using an electrical signal shielding technique. The development of an omnidirectionally stretchy carbon black-Ecoflex composite based shielding layer ensures low-level noise in sensing matrices by efficiently attenuating electrostatic interference from wirings. Demonstrated are deformable human-machine interfaces, intelligent insoles for gait measurement, and smart gloves for tactile identification. This work represents a significant advancement in haptic sensing by providing answers for the difficult problem of large-area multiplexed sensing arrays.

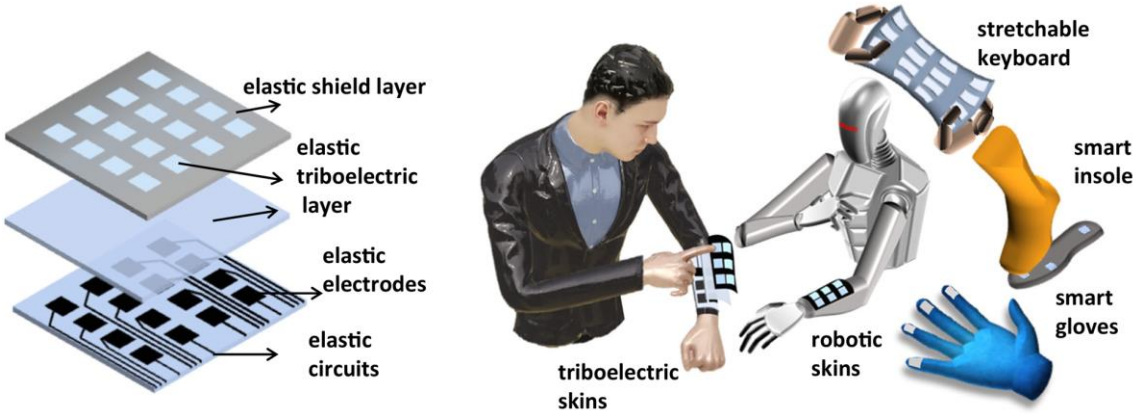

Figure 3.16 Schematic design of the untethered triboelectric electronic skin (UTE skin) [34].

4 Development of PLA filaments

4.1 Synthesis of PLA

In this thesis, the primary matrix material utilized was Polylactic Acid (PLA), specifically REVODE 101 (Luminy L175) [36], supplied by Total Corbion PLA, Thailand. PLA in general is considered a recyclable, natural thermoplastic polyester that is produced from renewable resources. PLA is routinely used in 3D printing due to its low cost compared to other thermoplastics, while also being very forgiving during the printing process.

Moreover, PLA is biodegradable under certain conditions, bio-compatible, non-toxic and does not contribute to environmental pollution [37]. PLA printed structures can be recycled, although the mechanical properties of the recycled parts may differ from the original material [37]. Regarding its mechanical properties PLA has relatively high strength although its rigidity is moderately low [38]. PLA's applications span from biodegradable packaging to medical devices, reflecting its versatility and eco-friendly nature.

According to used PLA's data sheet, its typical (physical & mechanical) properties are shown in Table 1.

Table 1 Physical and Mechanical Properties of REVODE 101 (Luminy L175) [36]

Properties	***Values***	***Units***
Density	1.24	$g/cm3$
Glass transition temperature	60	$°C$
Melting point	175	$°C$
Stereochemical purity	$\geq$ 99	% $(L-isomer)$
Residual monomer	$\leq$ 0.3	%
Water / moisture	$\leq$ 400	ppm
Tensile modulus	3.5	GPa
Tensile strength	50	MPa
Specific heat	1800	$J/Kg°K$
Elongation at break	$\leq$ 5	%
Charpy notched impact, 23	$\leq$ 5	$kJ/m2$
Heat Deflection Temperature, amorphus	60	$°C$
Heat Deflection Temperature, crystalline	105	$°C$

Polylactic Acid (PLA)

PLA (Figure 4.1) is an aliphatic polyester that is made from starch that is taken from renewable vegetable sources like potatoes and corn [38]. The glucose is then fermented to produce lactic acid, which is then further polymerized. PLA is completely biodegradable, strong, and has exceptional biocompatibility. After decomposition, carbon dioxide and water are the final products. It is therefore non-toxic and does not pollute the environment [46]. PLA's stiffness is low despite its great integral characteristics and high strength (Table 1).

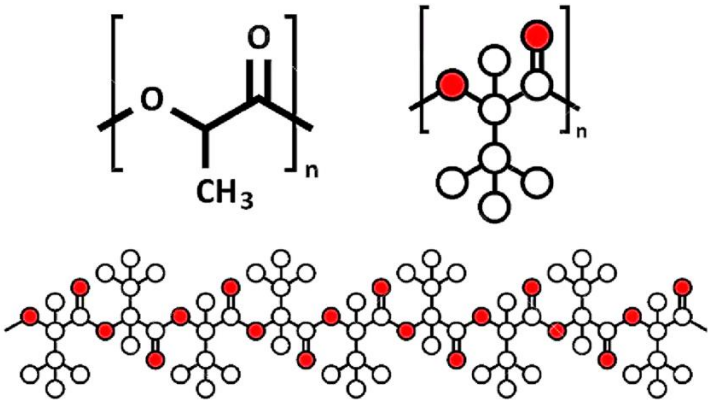

Figure 4.1 Chemical Structure of polylactic acid (PLA) [38].

PLA is an aliphatic polyester that possesses minimal shrinkage, strong mechanical processing performance, and the essential properties of popular polymer materials. It is extensively utilized in the production of biodegradable medicinal items, household appliance shells, and packaging materials: Airless water bottle, fresh juice bottle, cosmetic bottle; blow molding: dessert container, tray, cup, coffee capsule; composite: wood, PMMA, PC, ABS; fiber extrusion: apparel, tea bags; injection molding: containers, disposable tableware; This material's diversity pertains to all highly interesting 3DP undertakings[38].

Silicon Carbide (SiC) doping

To augment the mechanical properties of the PLA matrix, Silicon Carbide (SiC) powder, provided by Struers, USA, was added. With a specified grain size of less than 1200 nanoparticles per cm, i.e. $\frac{1cm}{1200} = 8.3\mu m\ size$, SiC introduces exceptional hardness, thermal conductivity, and resistance to thermal shock into the composite. This inclusion leverages SiC's applications in high-performance environments, including abrasives and semiconductors, enhancing the composite's utility in demanding applications [39]. In addition, SiC is a semiconductor and is being developed as a potential replacement for Si in high-temperature electronic applications.

Although it is rarely encountered in nature, silicon carbide is present in the mineral moissanite. It is created artificially via a process known as the Acheson method, after Edward G. Acheson, who invented it [40]. An electric resistive furnace is used to combine pure silica (SiO_2), also known as quartz sand, with finely ground petroleum coke (carbon), and heat the mixture to a temperature that

is escalated to between 1700 and 2500°C. Here below is the main chemical reaction resulting in the formation of α-SiC:

$$SiO_2 + 3\ C \rightarrow SiC + 2\ CO$$

Zinc Oxide (ZnO) doping

Additionally, Zinc Oxide (ZnO) powder, sourced from Sigma Aldrich, USA, was integrated into PLA to produce a second category of composites. The ZnO particles, with a size of less than 100 nm, contribute to the composite's functionality by offering UV protection, antimicrobial properties, and improved thermal conductivity. ZnO's broad application range, from sunscreens to semiconductor devices, underscores its value in enhancing the PLA composite's performance and utility [41].

The choice of production method of ZnO depends on the desired purity, particle size, morphology, and specific application of the ZnO. For high-purity applications, such as in electronics or optics, the indirect method might be preferred. For broader industrial applications, the direct method offers a cost-effective solution [41]. The starting materials conventionally used in this method are mainly anhydrous $ZnCl_2$,Na_2CO_3 and NaCl. The following reactions take place during the procedure:

$$ZnCl_2 + Na_2CO_3 \rightarrow ZnCO_3 + 2\ NaCl$$

$$ZnCo_3 \rightarrow ZnO + CO_2$$

4.2 Filament Production for 3D Printing

The production process of composite filaments based on PLA by diffusion (either SiC microparticles or ZnO nanoparticles) is illustrated in the chart in Figure 4.2.

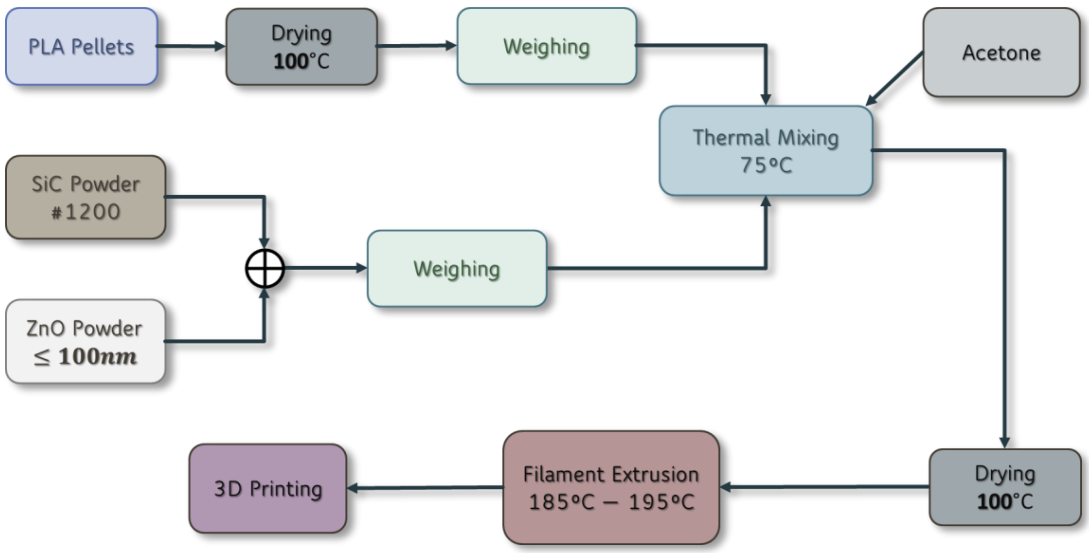

Figure 4.2 Schematic of the fabrication process.

At first, PLA pellets were dried at 100°C for 24 hours. Then, the dried PLA pellets and SiC or ZnO were weighed to produce composites containing 1 to 3% of the dopant. The mixture was then placed

in a heated mixing bowl shown in Figure 4.3 and manually mixed with a few drops of absolute grade acetone at about 75°C, where it is known that acetone partially dissolves PLA thereby enhancing adherence of the doping powder to PLA. The mixture was then placed in a drier at 100°C for 24 hours to remove any moisture from the external environment.

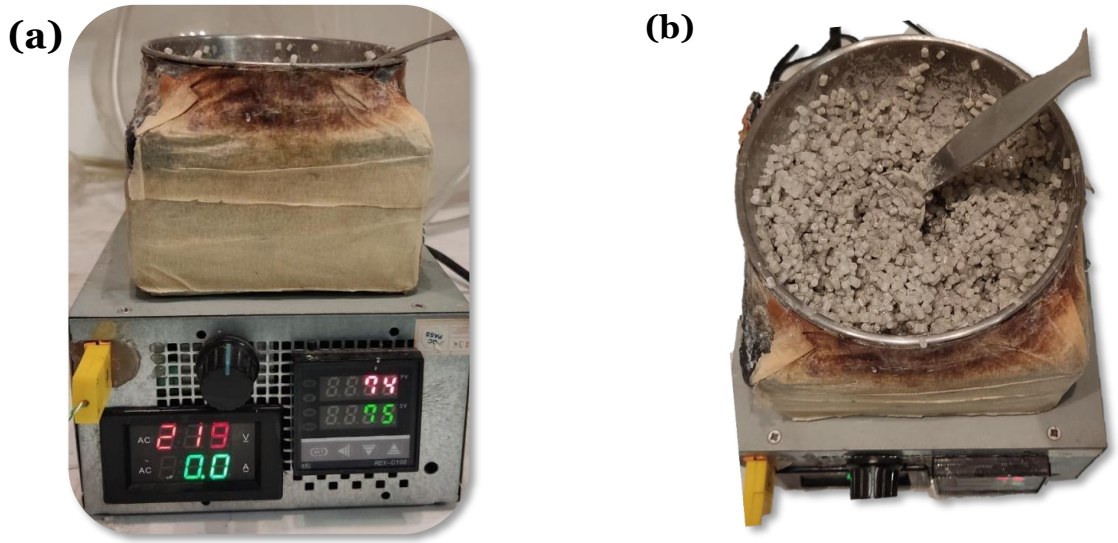

Figure 4.3 Thermal mixing bowl shown from (a) below and (b)above.

The mixture was then placed in the extruder (Felfil Evo Filament Extruder, Italy) shown in Figure 4.4 (a) to produce filament with a diameter of approximately 1.75 *mm*. The extruder operates using a screw-feed system: it heats the mixture to 185 – 195°C and through the screw it is extruded to the outlet, creating the desired filament. This filament is then placed in the printer to create the samples as explained in the section 4.2.2.

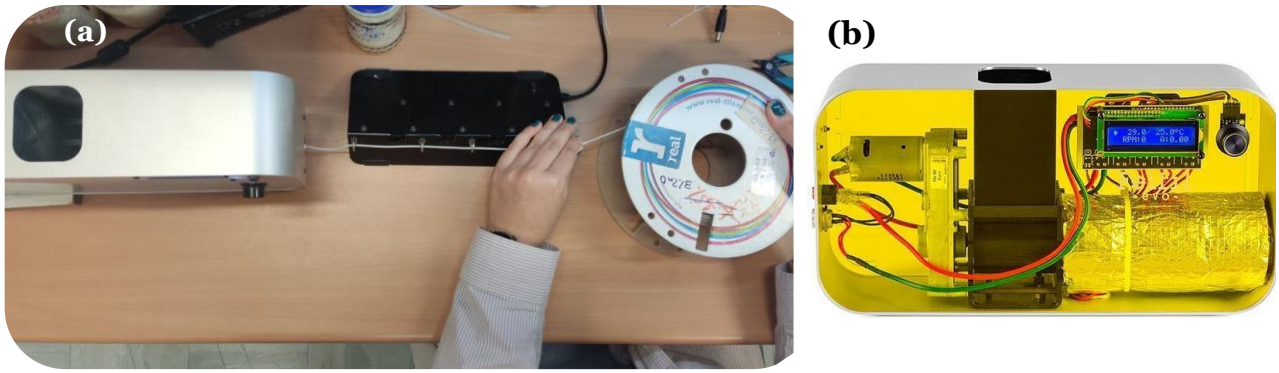

Figure 4.4 (a) Filament extrusion process (b) Felfil Evo Filament Extruder.

For the filament extrusion process, it was found that a higher extruder's temperature was necessary in order to successfully produce filaments with a larger SiC or ZnO powder content in the PLA mixture. In particular, 185°C was required for pure PLA filament but 195°C for PLA – 3wt% SiC filament, and for PLA – 3*wt*% ZnO filament. Some produced filaments are shown in Figure 4.4. Pure PLA filament has a transparent color, while SiC doped PLA has a kind of gray color and ZnO doped PLA has a white look color.

Figure 4.5 From left to right: PLA – 3wt% SiC, PLA – 3wt% ZnO, PLA virgin.

4.2.23D Printing of Specimens

The specimens used in the measurements of the present study - both for the examination of mechanical properties and the triboelectric properties - were manufactured using the 3D Printing method.

3D printing is a computer-assisted object manufacturing technique where the material is assembled in the design space throughout the process. One of the most popular commercial methods of this technology is Fused Deposition Modeling (FDM) or Fused Filament Fabrication (FFF). This is a technology based on the extrusion of thermoplastic material and has evolved to such an extent that the use of 3D printers has become established. In this work, the CREALITY CR20 Pro 3D printer (Creality 3D Technology Co., Ltd., Shenzhen, China) was used, which is illustrated in Figure 4.6.

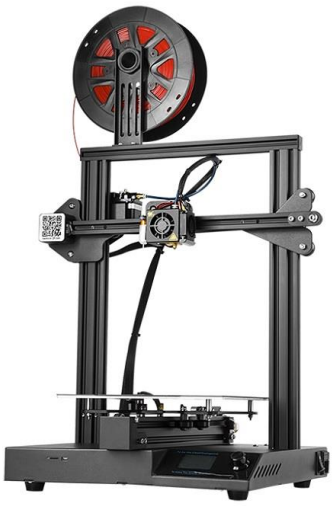

Figure 4.6 CREALITY CR20 Pro 3D printer.

The specimens (dog-bone shape) for measuring the tensile strength of the materials were printed by the above 3D printer according to the instructions according to ISO 527 standard [42] that will also be discussed in chapter 5.1.1 as shown in Figure 5.4. The specimens for the other hardness

measurements were shaped as a thick disk 32mm in diameter and approximately 6mm thick as shown in Figure 5.9.

The specimens for the investigation of the triboelectrical and electrical characterization were printed in the shape of a thin disk $32mm$ in diameter and $0.6mm$ thick.

The specimens were 3D-printed using the following parameters:

- Filament Diameter : 1.75 mm
- Nozzle temperature : 200 – 210 °C
- Bed temperature : 55 °C,
- Nozzle size = 1 mm
- Printing speed = $50mm/sec$.

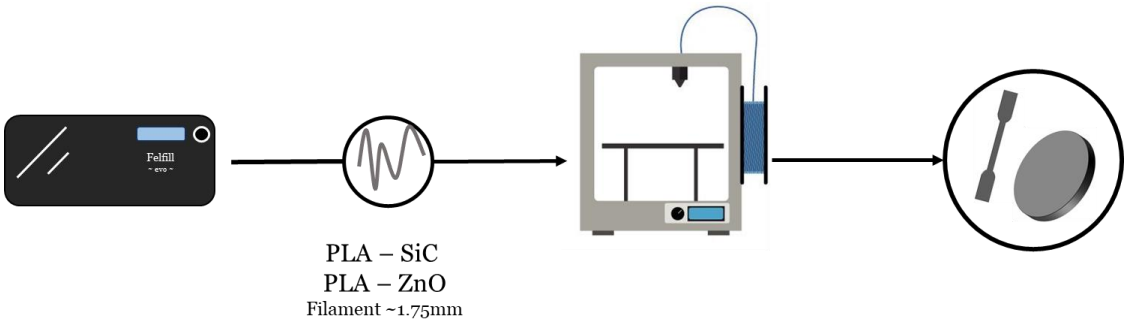

Figure 4.7 Process from filament extrusion to 3d printing of specimens under test.

4.3 Preparation of Specimens

For the samples to be comparable with each other in the measurements given and covered in the upcoming chapters, they had to be roughly ground to the same thickness using a polishing machine.

As seen in Figure 4.8 below, the Struers DAP-V (Struers Pedemin DAP-7 grinding and polishing machine) was used for the sample grinding and polishing procedure. The apparatus is made up of two main parts:

1. Base: spins the abrasive disc in rotation.
2. PEDEMIN-2 specimen support arm: Specimens can rotate in the opposite direction of the abrasive disc.

A faster removal of material is possible because of the increased frictional forces between the samples and the abrasive disc due to their opposite rotational directions. The samples can be processed and supported on the abrasive disc by a spring when they are in one of the arm's three slots, which contains a small motor.

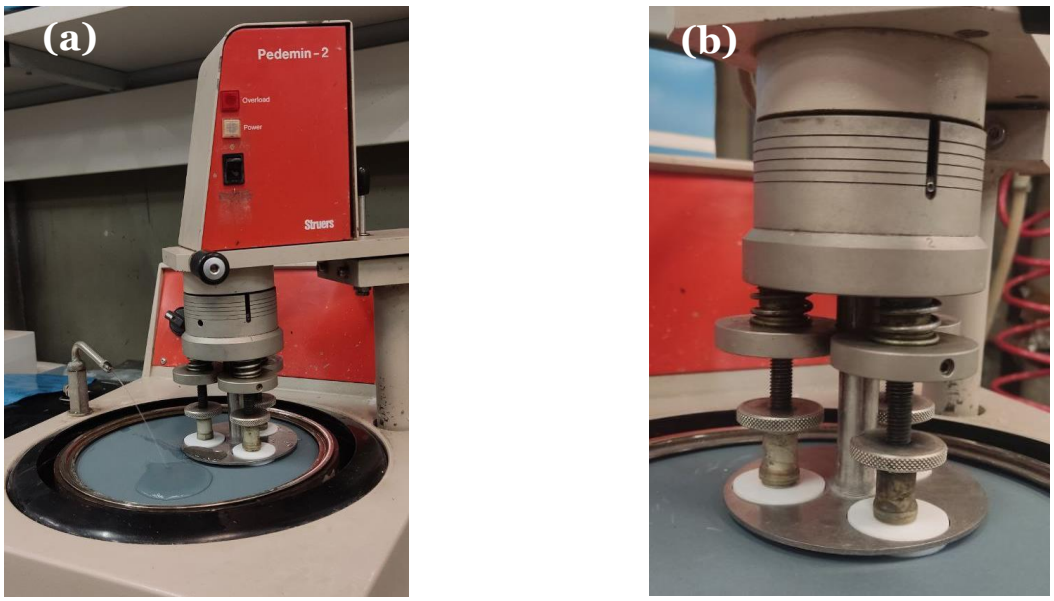

Figure 4.8 (a) Struers DAP-V with Struers Pedemin DAP-7 (b) Pedemin holding 3 specimens PLA-3%ZnO.

Silicon carbide (SiC) abrasive paper was used for the polishing of the samples. The paper was placed on the surface of the abrasive disc and fixed with a suitable metal ring. Each type of paper is identified by a "mesh size" number corresponding to the size of the abrasive grains. The higher the number, the smaller the grain size The mesh size is the number of grains per inch (25.4*mm*).

Polishing was carried out progressively utilizing SiC sandpaper with ascending order of mesh-size; that is, polishing proceeded with Sic paper #120, then #320 and finish with #1000.

After the samples are polished to #1000 SiC paper, they were allowed to air dry for 24 hours at room temperature.

4.4 Microstructural Characterization

The scanning electron microscopy (SEM) technique was used to study the surface morphology of the materials used for PLA reinforcement. This technique allows obtaining information that contributes to the understanding of the behavior of solid materials. Morphological and elemental characterization of the fabricated composites was performed by Scanning Electron Microscopy (SEM, FEI Quanta Inspect shown in Figure 4.12 (a)) and by Energy Dispersive X-ray Spectroscopy (EDX, 10 *keV* shown in Figure 4.12 (a)).

SEM is a type of electron microscope that creates a topological image and relative composition of a material by reacting with a concentrated electron beam. The concentrated electron beam will produce secondary electrons (SEs), backscattered electrons, and a distinctive X-ray upon contact with the material. These will subsequently be detected by the appropriate detectors and shown on the monitor. The electron source, sample chamber, electron detector, column with electromagnetic lenses, and computer display are the primary parts of a standard SEM [43].

The creation of a SEM picture is primarily associated with the identification of signals derived from interactions between scanned samples and electron signals. Elastic and inelastic interactions are the two main types of interactions that might happen. Following their bombardment by the primary beam electrons, the samples in the inelastic interaction release low-energy secondary electrons (transfer of energy to the atom in the sample). Conversely, elastic interaction results from the main electron's deflection upon contact with the atomic nucleus of the sample or electrons of similar energy. Back scattered electrons (BSE) are dispersed electrons that have been deflected at an angle greater than ninety degrees. They can be used for imaging samples [43]. The generation of SEs and BSEs is shown in Figure 4.9 .

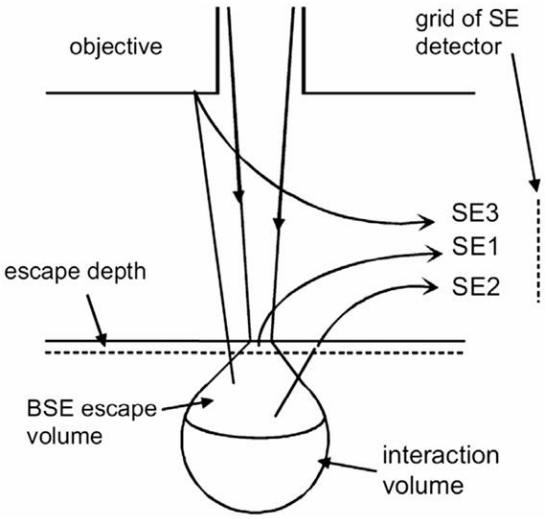

Figure 4.9 : Electron signal interaction upon contact with the specimen. SE1 corresponding to secondary electron mode, whereas SE2 and SE3 are used in back scattered electron mode.[43]

The result of this process is the acquisition of signals from the surface, including backscattered and secondary electrons, which are the most important signals. Auger electrons, X-ray fluorescence photons and other photons of other energies are also detected.

During the SEM analysis, chemical identification of the constituent elements of each sample was also carried out. Chemical identification during the study of samples was performed using the EDAX (Energy Dispersive Analysis of X-rays) technique.

EDX spectroscopy is involved in the detection of elemental composition of substance by using scanning electron microscope. EDX can detect elements that possess the atomic number of higher than boron and these elements can be detected at concentration of least 0.1%. The application of EDX includes material evaluation and identification, contamination identification, spot detection analysis of regions up to 10 cm in diameter, quality control screening, and others [43].

The materials in a standard SEM interact with the electron beam upon collision, releasing distinctive X-rays. Since every element has a unique X-ray emission spectrum, it is possible to distinguish between them and determine their concentration in the sample. The main electron beam's contact with the sample atom's nucleus produces the X-ray. An atom's nucleus contains an

electron that is excited by a primary electron beam, which causes the electron to be ejected and leaves an electron hole behind. The excess X-ray is released when an electron from the atom's outer shell, which has a higher energy, replaces the expelled electron that was lost. The X-ray that is released is composed of two types: the characteristic X-ray, which is produced when a higher shell electron fills the electron hole in the nucleus shell, and the X-ray continuum, which is produced when an electron decelerates. This is seen in Figure 4.10 .

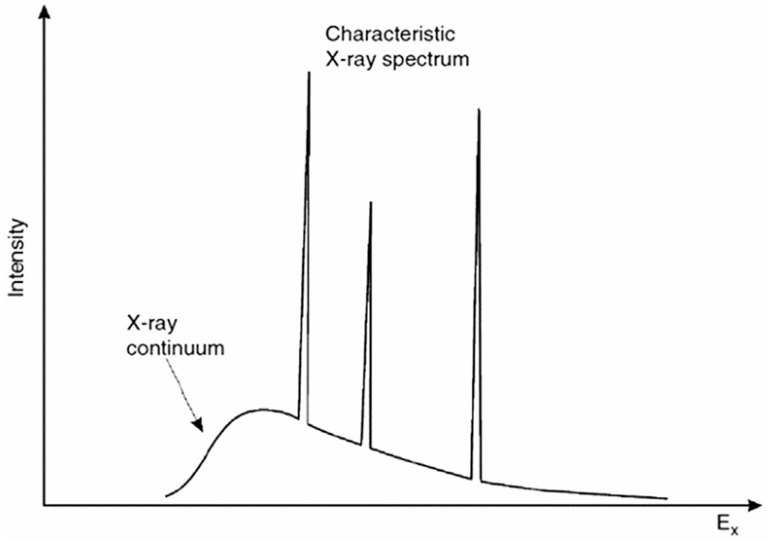

Figure 4.10 : Schematic representation of the types of X-ray spectrum emitted upon bombardment of fast electron.[43]

While conducting the SEM, the electron beam hitting the sample causes X-ray emission. This X-radiation interacts with the atoms in the sample, causing the emission of characteristic X-rays for each element in the sample. EDAX collects these X-rays and analyses their energy to determine which elements are present in the sample and in what quantities. Thus, the EDAX technique can provide information on the chemical composition of the material being tested.

Sputter deposition is a physical vapor deposition (PVD) method that involves ejecting material from a "target" that is a source onto a "substrate". Resputtering is re-emission of the deposited material during the deposition process by ion or atom bombardment. Sputtered atoms ejected from the target have a wide energy distribution, typically up to tens of eV (100,000 K). The sputtered ions can ballistically fly from the target in straight lines and impact energetically on the substrates or vacuum chamber (causing resputtering). Alternatively, at higher gas pressures, the ions collide with the gas atoms that act as a moderator and move diffusively, reaching the substrates or vacuum chamber wall and condensing after undergoing a random walk. The entire range from high-energy ballistic impact to low-energy thermalized motion is accessible by changing the background gas pressure. The sputtering gas is often an inert gas such as argon [44].

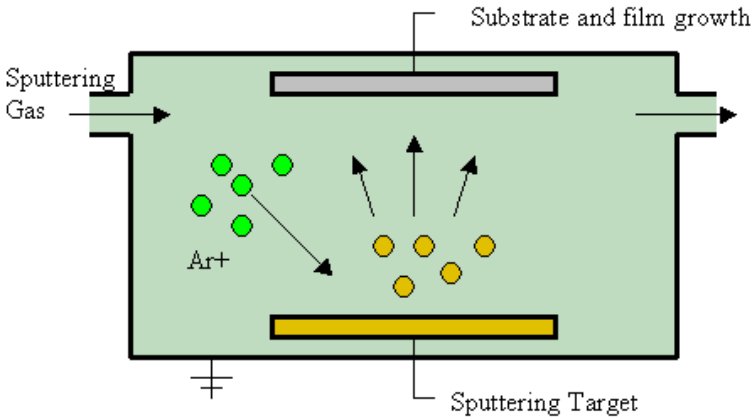

Figure 4.11 : A schematic of sputter deposition.

For the examination of non-conductive samples such as PLA, a Polaron E5100 Sputter Coater was used for coating the samples as shown in Figure 4.12 (b). The process is about applying an extremely thin layer of an electrically conducting metal, such as gold (Au), gold/palladium (Au/Pd), platinum (Pt), silver (Ag), chromium (Cr), or iridium (Ir) to a non-conductive or poorly conducting material is known as sputter coating in SEM terminology. The specimen is kept from charging by sputter coating, which stops static electric fields from building up. Additionally, it raises the signal to noise ratio by increasing the quantity of secondary electrons that can be seen on the specimen's surface in the SEM. The normal thickness range for sputtered films used in SEM is 2–20 nm [45].

(a) **(b)**

Figure 4.12 (a) SEM, FEI Quanta Inspect (b) E5100 Sputter Coater

4.4.1 SEM & EDAX Analysis

The microstructure of the SiC powder is shown in the SEM micrographs in Figure 4.13. The powder is irregular and angular with a maximum grain size (largest dimension) of about 8.3 μm corresponding to a mesh size of #1200.

A quantitative assessment of the grain size distribution based on SEM micro-graphs showed that the powder had an average grain size of about 7 μm and a range of $4 - 8.3\ \mu m$.

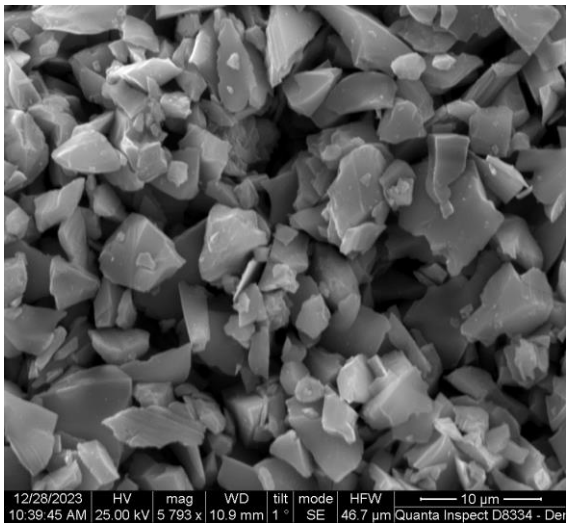

Figure 4.13 SEM micrograph of the irregular SiC powder of mesh size #1200 used in this work

Typical fracture surfaces of a PLA ('virgin") specimen after fracture in tension and after abrasion with #1000 SiC paper are shown in Figure 4.16 (a) and (b) respectively.

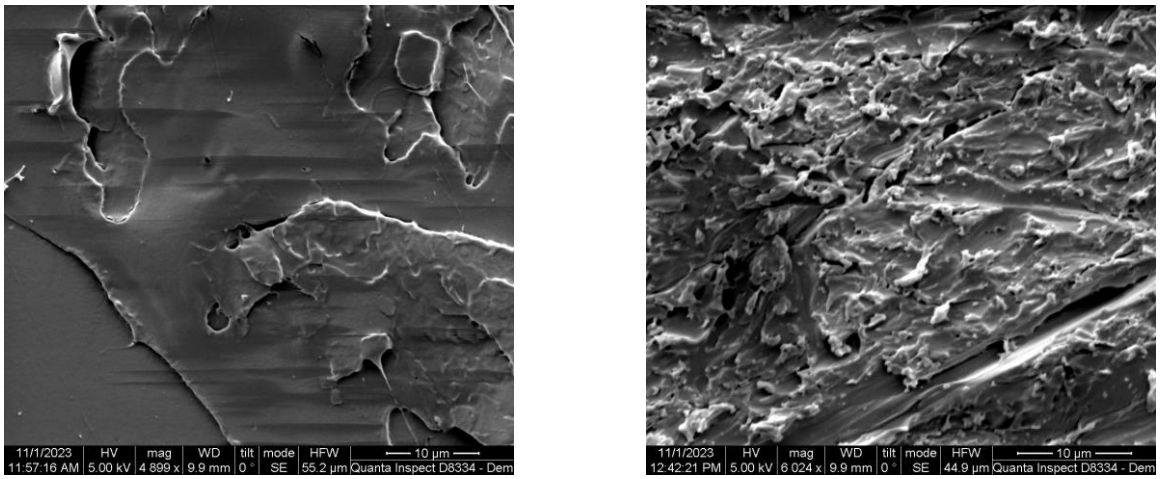

(a) **(b)**

*Figure 4.14 SEM Images for pure PLA from (a) Fracture Surface from tension with magnitude x*4899 *and (b) after abrasion with* #1000 *SiC paper with magnitude x*6024

An EDX spectrum of a PLA ("virgin") specimen at low ($x100$) magnification is shown in Figure 4.15 where Carbon and Oxygen are slightly obscured by some gold peaks.

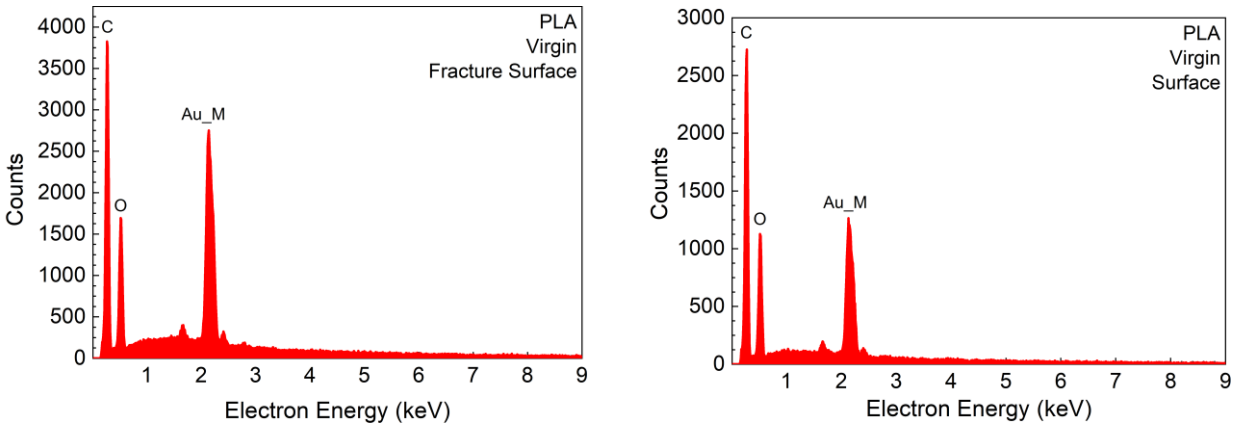

(a) **(b)**

Figure 4.15 EDX spectrum of a pure PLA specimen (a) for fracture surface and (b) after abrasion with #1000 SiC paper

Typical fracture surfaces of a PLA – 3%SiC specimen after fracture in tension and after abrasion with #1000 SiC paper are shown in Figure 4.16 (a) and (b) respectively. Predominantly quasi-ductile fracture is visible with some evidence of brittle fracture as evidenced by some fine striations (visible in Figure 4.16 (a)). The SiC particles are well coated by the PLA but occasionally they are exposed as in Figure 4.16 (b).

A semi-quantitative estimation of the areal density of SiC on the surface of the 3*wt*% specimens indicated values of between 1 and 1.5 *areal*% which is in a general agreement with the 1.3 *vol*% of SiC calculated for such materials.

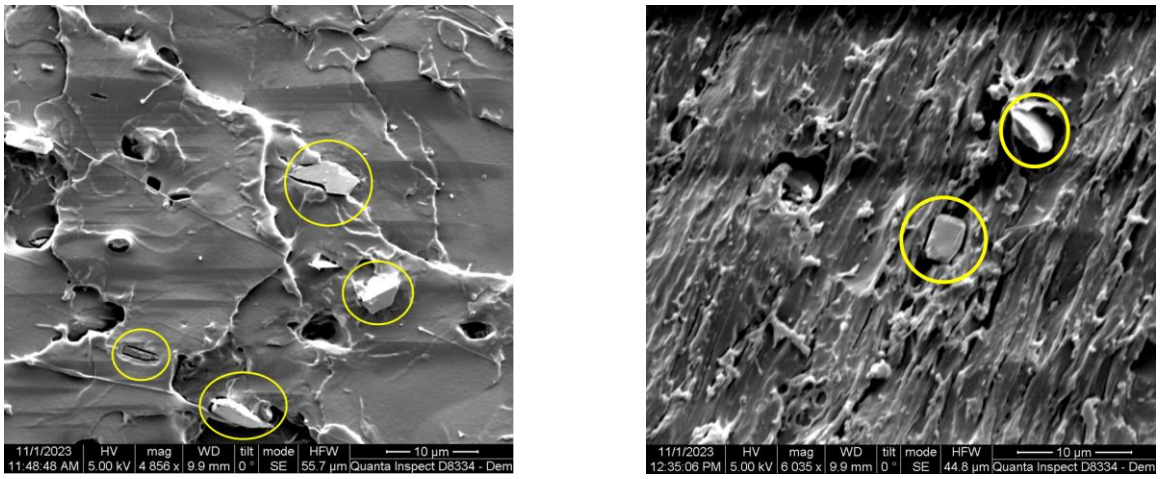

(a) **(b)**

*Figure 4.16 SEM Images for 3% SiC from (a) Fracture Surface from tension with magnitude x*4856 *and (b) after abrasion with* #1000 *SiC paper with magnitude x*6035

An EDX spectrum of a PLA–3%SiC specimen at low (*x*100) magnification is shown in Figure 4.17 where the Si peak is partly covered and slightly obscured by a gold peak.

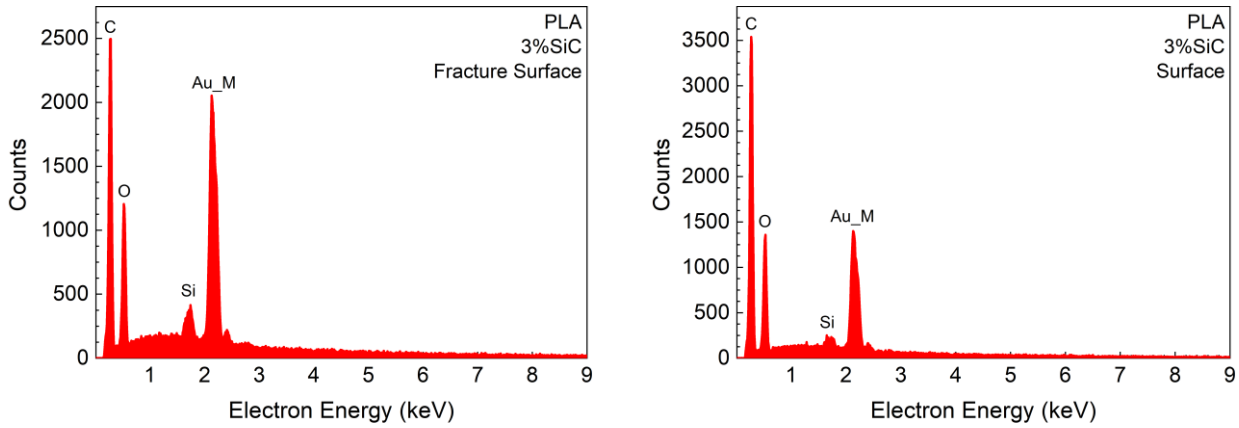

(a) **(b)**

Figure 4.17 EDX spectrum of a 3%SiC specimen (a) for fracture surface and (b) after abrasion with #1000 *SiC paper*

Figure 4.18 shows SEM micrographs of the PLA–3% ZnO specimen after fracture in tension and after abrasion with #1000 SiC paper. We can identify the presence of ZnO nanoparticles. The distribution of the ZnO nanoparticles appears to be uniform.

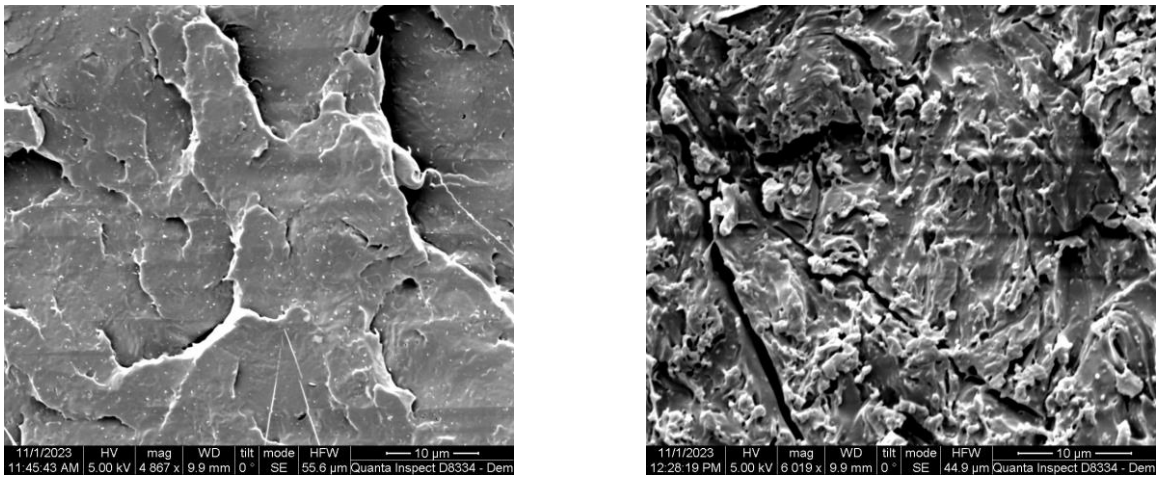

(a) **(b)**

*Figure 4.18 SEM Images for 3% ZnO from (a) Fracture Surface from tension with magnitude x*4867 *and (b) after abrasion with* #1000 *SiC paper with magnitude x*6019

Figure 4.19 presents an EDX spectrum acquired for the 3*wt*% ZnO-doped PLA. We can identify the L and K emission peaks of Zn at 1.011*keV* and 8.61*keV*, verifying the existence of ZnO nanoparticles. The emission peaks at 1.66*keV* and 2.14 *keV* correspond to the thin gold layer that was deposited on the PLA sample prior to SEM imaging, in order to avoid surface charging phenomena.

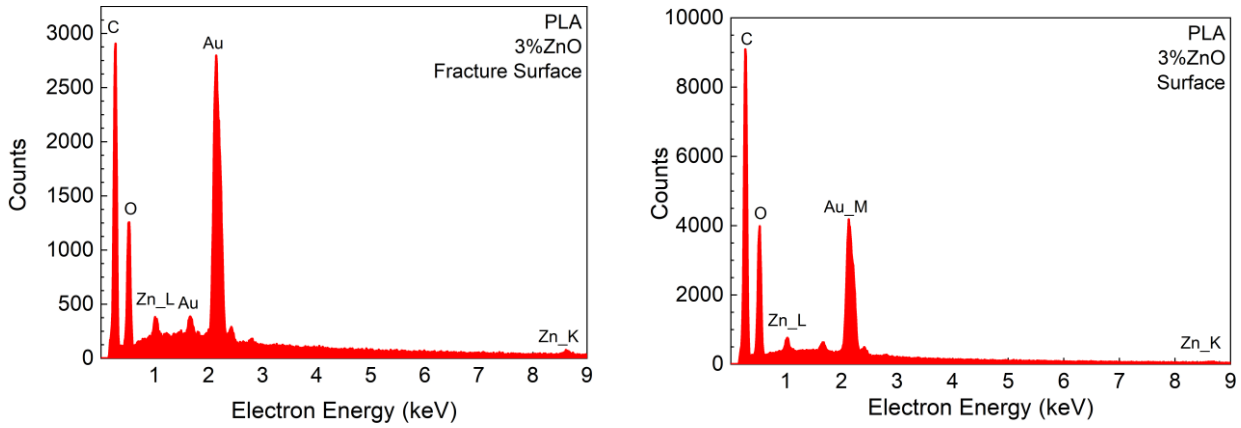

(a) **(b)**

Figure 4.19 EDX spectrum of a 3%ZnO specimen (a) for fracture surface and (b) after abrasion with #1000 SiC paper

4.4.2 Influence of polishing

The microstructure of a 3d printed PLA "virgin" specimen before and after polishing with abrasive #1000 SiC paper is shown in the SEM micrographs in Figure 4.20.

Figure 4.20 (a) and (b) show the specimen's surface as printed. The 3d printed lines can be clearly seen with a width between them about $225 - 235\ \mu m$.

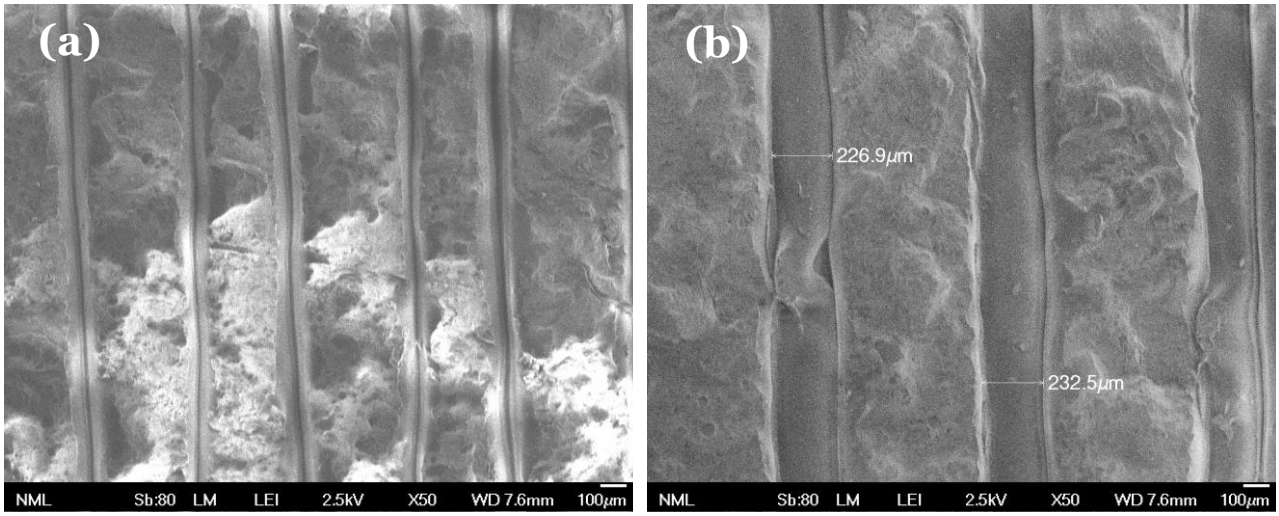

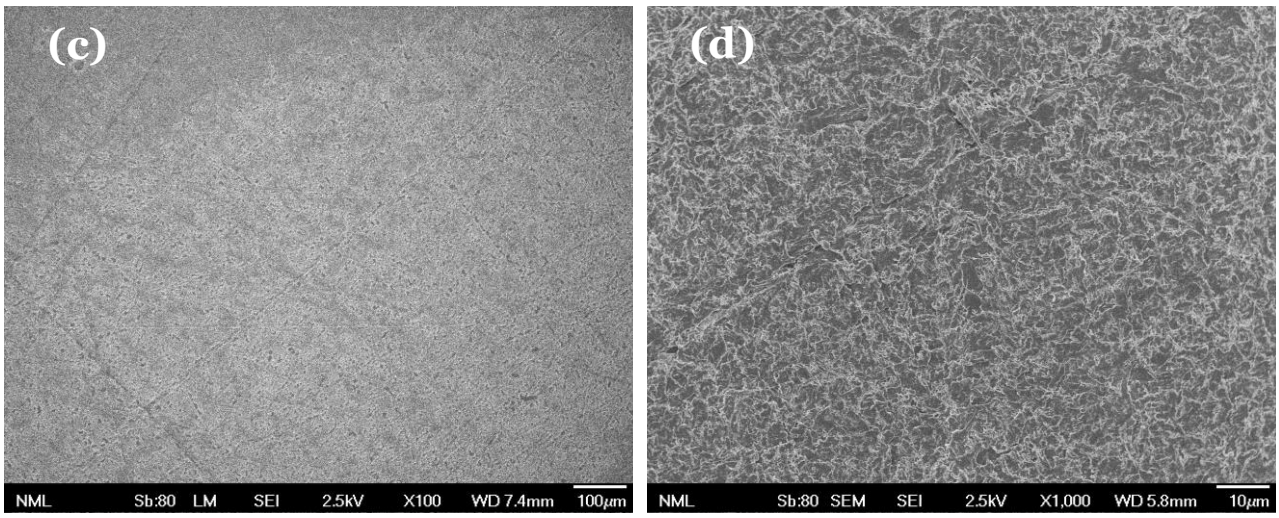

*Figure 4.20 (a) and (b) SEM images of an as printed pure PLA sample with magnitude x*50 *and (c) and (d) after polishing with #1000 SiC paper of a pure PLA sample with magnitude x*100 *and x*1000 *respectively.*

Figure 4.20 (c) and (d) show the specimen's surface after polishing with #1000 SiC abrasive paper. The polishing process with #1000 mesh SiC paper has significantly improved the surface finish of the PLA material. The before image shows a rough surface with visible scratches and irregularities, while the after image shows a much smoother and more uniform surface. The use of #1000 mesh SiC paper is effective in reducing the roughness and irregularities on the PLA surface. This indicates that the polishing process has been successful in smoothing out the surface, which is consistent with the findings in similar studies. Such polishing is commonly used in various industries to enhance the appearance and performance of materials, especially where a smooth surface is necessary, such as in medical devices, optical components, or precision instruments.

4.5 Estimation of surface Roughness

An object's surface roughness can be expressed using a parameter called root mean square height, or Sq. By measuring the average height variations within the designated area of the surface, it quantifies the texture of a surface. Sq is equal to the standard deviation of the heights and is computed as the root mean square value of the ordinate values (heights) inside the defined region. The following is the mathematical formula for Sq:

$$S_q = \sqrt{\frac{1}{A}\iint_A z(x,y)^2 dxdy} \qquad (4.1)$$

Where:

- z(x,y) is the height of the surface at a particular point with coordinates (x,y).
- The double integral indicates that the calculation is performed over the entire area A being evaluated
- The square root is taken of the average of the squared heights, which gives the root mean square value.

Sq is a statistical measure of the surface's departures from a mean plane and is a three-dimensional extension of the two-dimensional root mean square roughness parameter (Rq). It is especially helpful for surface texture characterization in applications where a thorough grasp of surface topography is necessary, including optical surfaces or machined parts where surface interactions are crucial [46], [47].

The Sq parameter does not distinguish between peaks, valleys, and the spacing of distinct texture characteristics since it is indifferent to the direction of the surface texture. This can occasionally be a drawback because two surfaces with identical Sq values but significantly dissimilar functional characteristics may have spatial and height symmetry features. As a result, even while Sq is a helpful general measure of surface roughness, additional parameters might be required to fully comprehend the surface's functional properties [46].

The surface roughness measurements of the fabricated samples doped with SiC and ZnO after polishing, were analyzed via white light interferometry (WLI), using a 3D optical profilometer (Profil3D®, Filmetrics).

The results were analyzed from the online software ProfilmOnline and the measurements for each sample had an area of 250 x 200 μm with fixed height 30 μm as shown below. The color-coding in the images is used to visually represent the differences in surface roughness, with the color scale provided in the bottom left corner indicating the roughness values. Blue represents the smoothest surfaces, green indicates intermediate roughness, and yellow signifies the roughest surfaces.

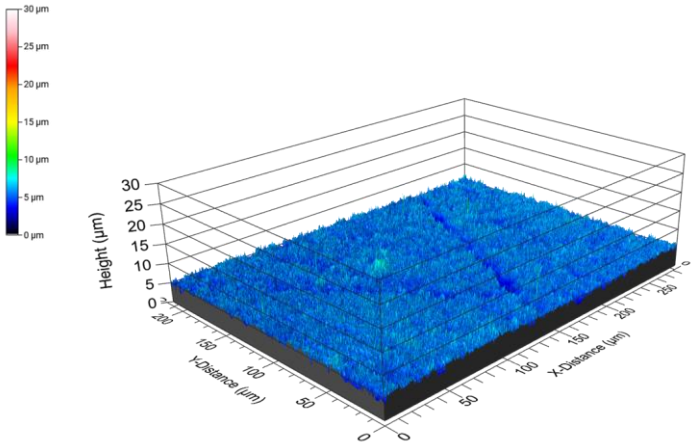

Figure 4.21 3D screenshot of surface roughness of undoped PLA sample.

The 2D screenshots from the surface roughness for SiC doped PLA samples are given in Figure 4.22.

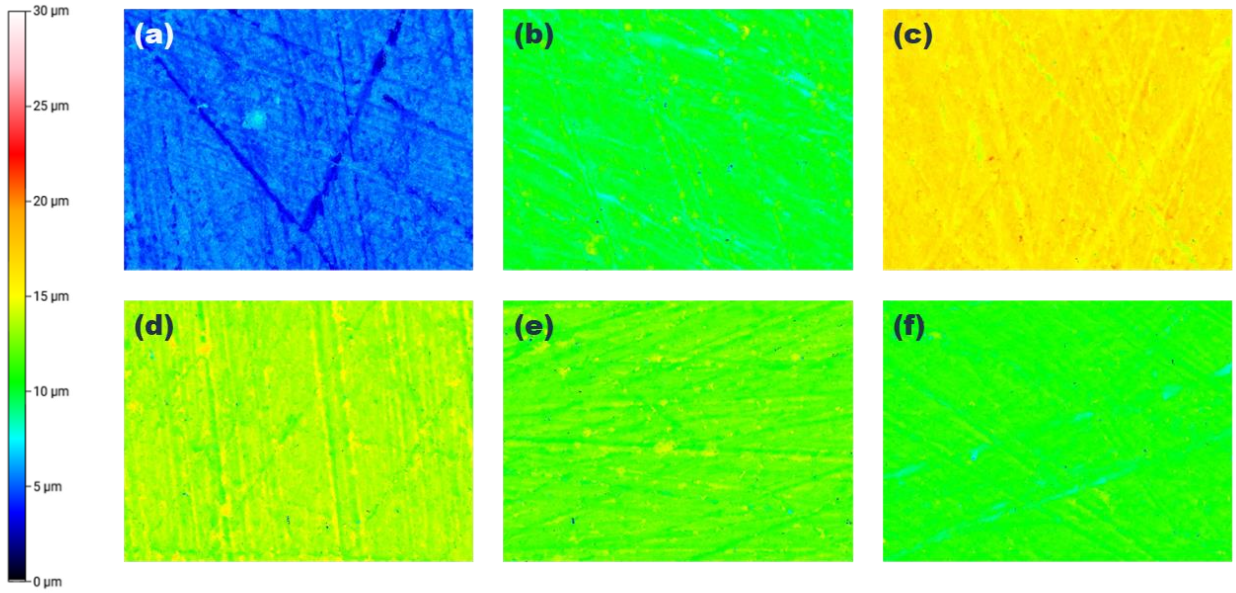

Figure 4.22 Area Roughness in 250x200 µm for PLA with concentrations (a) 0%, (b) 1%, (c) 1.5%, (d) 2%, (e) 2.5% and (f) 3% SiC.

From these images, it can be understood that the roughness increases with the addition of SiC up to 1.5%, but then it appears to decrease slightly at higher concentrations.

The slight decrease in surface roughness after the 1.5% SiC concentration could indeed be due to agglomeration. When SiC particles are added to the PLA matrix, they can enhance the composite's surface roughness due to their abrasive nature and irregular shape. However, at higher concentrations, these particles may start to agglomerate, or clump together, rather than being evenly dispersed throughout the PLA matrix. This agglomeration can lead to a smoother surface in some areas where the particles have clumped, reducing the overall roughness measured.

Agglomeration can occur due to several factors, such as the increased viscosity of the composite material with higher filler content, which can hinder the even distribution of particles during processing. Additionally, the inter-particle forces between SiC particles can become more significant than the forces between the particles and the PLA matrix, leading to clumping.

The 2D screenshots from the surface roughness for SiC doped PLA samples are given in Figure 4.23.

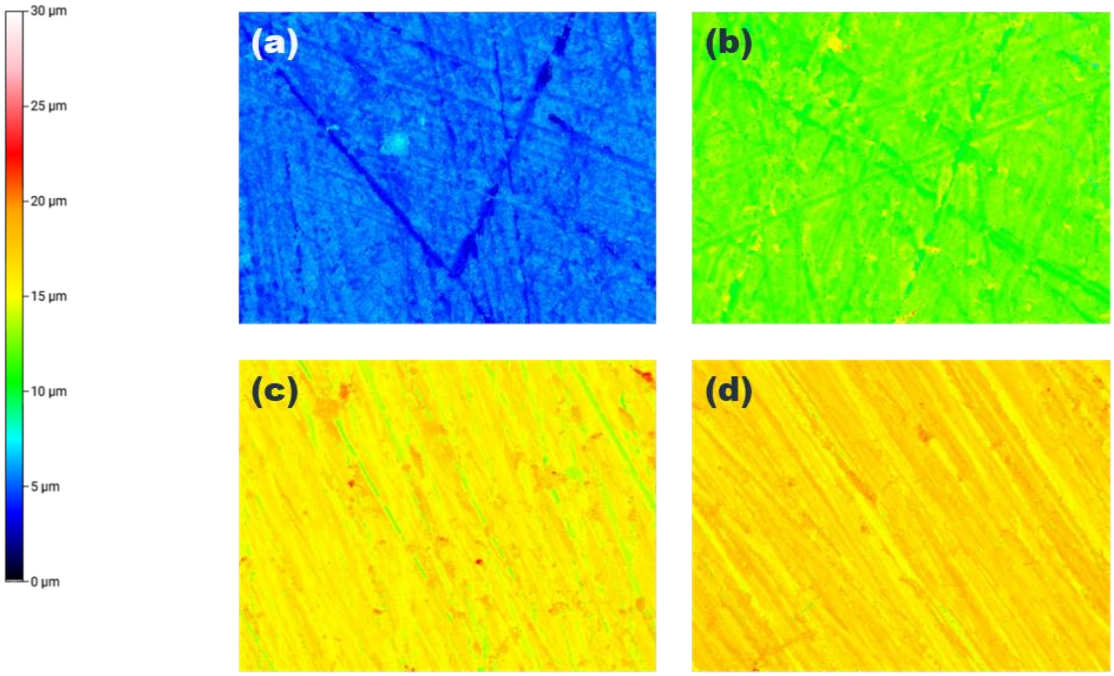

Figure 4.23 Area Roughness in 250x200 µm for PLA with concentrations (a) 0%, (b) 1%, (c)2%, and (d) 3% ZnO.

The increase in surface roughness with higher ZnO concentrations can be attributed to the presence of ZnO particles within the PLA matrix. These particles can create a more abrasive and irregular surface as they are incorporated into the material. The roughness of the surface is important for various applications, as it can affect properties such as adhesion, friction, and wettability.

The Sq values for each sample are given aggregated below.

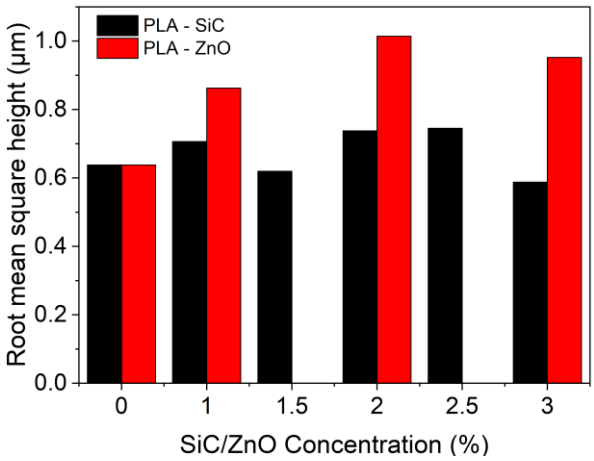

Figure 4.24 Root mean square height (Sq) for the range 0-3% PLA-SiC and 0-3% PLA-ZnO.

5 Mechanical Characterization

The Mechanical Characterization was carried out in the ACCL (Advanced Ceramics and Composites Laboratory) of the INN (Institute of Nanoscience and Nanotechnology) of the National Centre for Scientific Research "Demokritos".

5.1 Measuring Methodology of Mechanical Properties

5.1.1 Tension after Mixed Stress Fatigue

For mechanical testing, the ISO 527 standard serves as a cornerstone for assessing the tensile properties of plastic materials and their composites. The standard specifies the shape of the test specimen, the test speed, and how the results are to be calculated and reported. These tests are essential for understanding the mechanical behavior of the materials, particularly their strength and deformation under tensile loads [42].

In general, the key mechanical characteristics of a material are described by a set of characteristic values. Typical characteristic values are that are observed from the graph of the material during the test as it is shown in[42]:

- Tensile stress: force divided by the initial cross section area of the specimen usually measured in MPa (N/m^2).
- Tensile Extension: total change in length of the specimen, usually measured in mm – it should be equal to the change in gauge length.
- Strain: change in gauge length with respect to the initial gauge-length, expressed as %.
- Tensile modulus: gradient of the curve in the elastic region of the stress-strain diagram, usually measured in GPa.
- Yield point: stress and strain at the curve plot point at which the gradient is zero – this is mainly valid for metallic materials.
- Ultimate Tensile Strength (UTS): maximum stress achieved during tensile loading.
- Point of break: stress (Fracture Strength, often equal to UTS) and strain at the moment of specimen break.
- Poisson's ratio: ratio of transverse strain to axial strain in the elastic region.

If we take a look at a bar of the tensile specimen with its original cross-sectional area, A_0, subjected to equal and opposite force F tugging at the ends, the bar is in tension. The material is undergoing an axial elongation and a stress, which is determined by dividing the force by the bar's cross-sectional area [48].

Engineering Stress $$\sigma = \frac{F}{A_0} \quad (5.1)$$

Engineering Strain $$\varepsilon = \frac{L - L_0}{L_0} = \frac{\Delta L}{L_0} \quad (5.2)$$

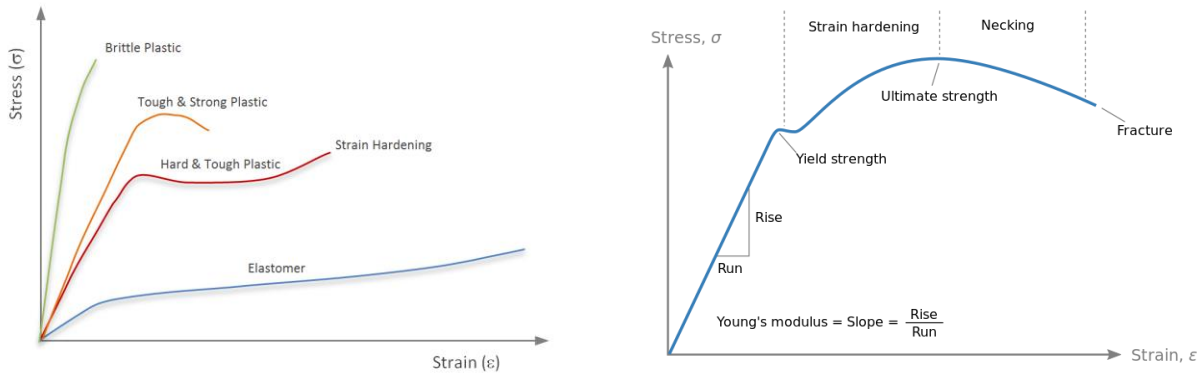

(a) **(b)**

Figure 5.1 5.2 (a) Typical stress/strain curves of brittle material, materials with yield points, and soft rubberlike material [42]. *(b) Stress/Strain curve of a low-carbon steel* [48]. *PLA at room temperature behaves as "brittle" while at slightly higher temperatures (up to the softening temperature, about 58C) it behaves as "tough and strong".*

In the tensile, compression, and flexural tests, the stress intensity increases gradually but steadily until the load eventually breaks the specimen. The strength characteristics obtained from these tests offer helpful values for material selection and component dimensioning, particularly for statically loaded components.

Researchers have shown that components exposed to variable stress can only tolerate lower stress values over time than those subjected to static stress [48]. Over time, fatigue fracture can still happen even if the stress is always lower than the material's yield or fracture strength. The fatigue test is used to evaluate material samples or complete components under dynamically changing stresses.

Standardized specimens and whole components are subjected to cyclic loading during the fatigue test. The sample is clamped in a machine that resembles a tensile testing apparatus for this purpose. Vibrational loading is applied to both complete components and standardized specimens during the fatigue test. For this reason, the sample is clamped in a device that looks like a tensile testing instrument. The upper clamping device is cycled dynamically, while the bottom clamping device is statically coupled to the surroundings. In the most basic scenario, the specimen experiences compressive and tensile stress alternately or cycling between zero and a tensile stress. It is also possible to fatigue test in flexure (bending) between zero and a certain flexure stress.

A load cycle, also known as a stress cycle, is a full cycle through the various stress levels. The letter N is frequently used to represent the total number of oscillations (stress cycles) up to a specific point in time.

In the fatigue test, several identical samples are dynamically loaded with different stress amplitudes and the respective number of cycles to failure is determined. If for each tested sample the respective stress amplitude σ_a is plotted against the number of endured cycles N_f, the so-called stress-cycle curve is obtained as it is shown below.

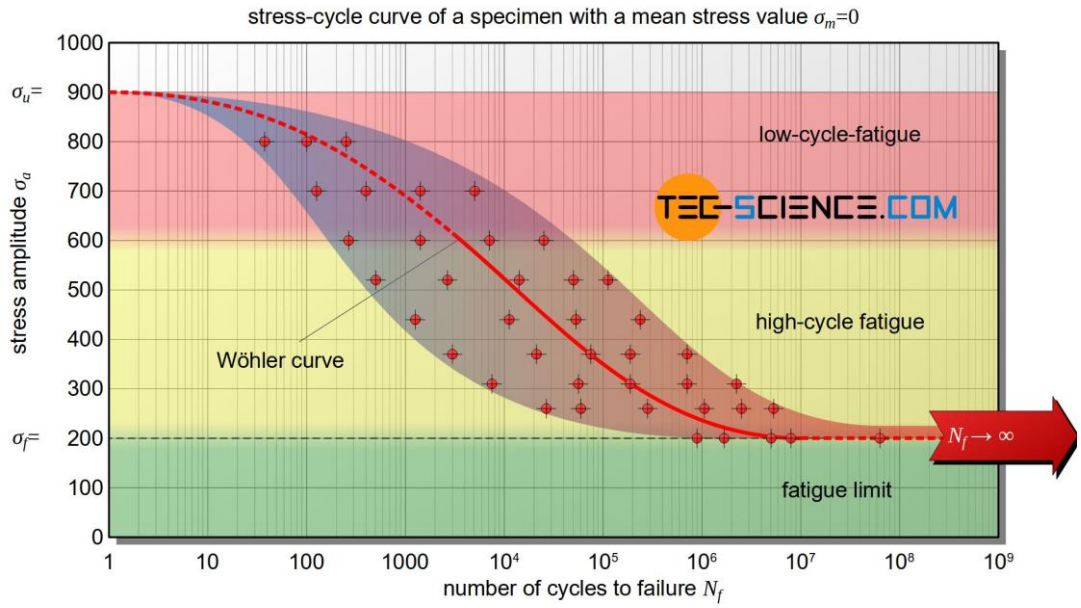

Figure 5.3 Stress – cycle & Wöhler curves of a specimen with a mean stress value $\sigma_m = 0$.

The diagram's obtained curve is frequently referred to as the Wöhler curve. The Wöhler curve should be understood as a probability curve that shows how many load cycles at a specific stress amplitude a sample is anticipated to withstand before breaking [49].

In this work tensile loading tests were conducted adhering to the ISO 527 standard after mixed mode (tensile and flexure) fatigue cycling. The specimens used were flat and "dog-bone" shaped with a nominal gauge length of 40 mm, gauge width of 6 mm and gauge thickness of 2 mm as shown in Figure 5.4 .

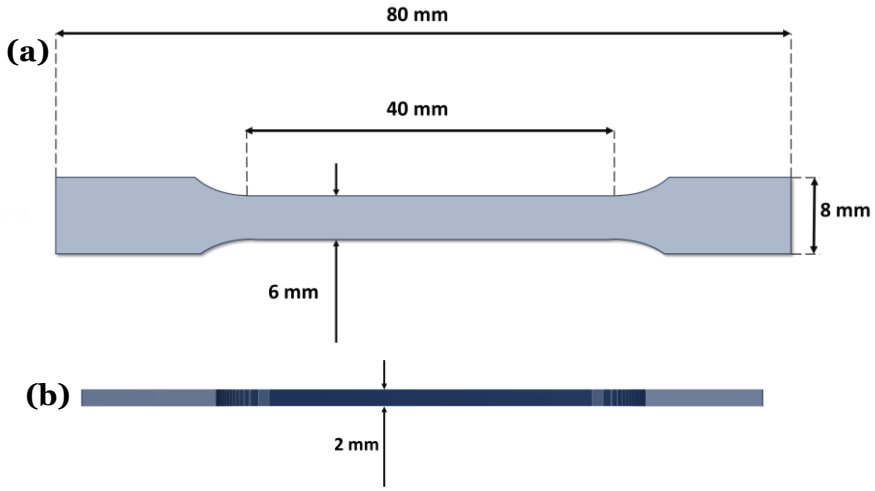

Figure 5.4 Dimensions of tensile specimen printed. The gauge length is 40mm and the thickness is 2mm.

Specimens were tested under tensile loading before and after mixed fatigue cycling to determine remaining strength. Fatigue of the tensile specimens was carried out under a mixed tension-bending mode on a specially built system shown in Figure 5.5. The specimens were cycled between about 50% of maximum expected tensile deformation and about 50% of maximum expected flexure deformation for up to 400 cycles at a rate of about 0.5Hz (2 seconds per cycle).

The load-extension curves obtained were analyzed to obtain the ultimate tensile strength (UTS, stress at maximum load) and the strain at maximum load.

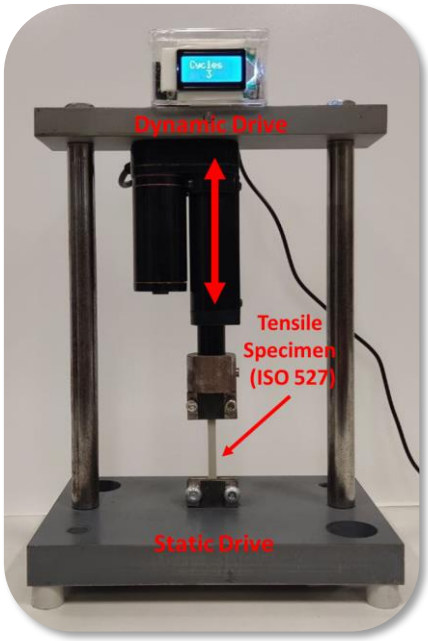

Figure 5.5 In-house mixed-stress Fatigue system.

The tensile tests after fatigue were carried out on an INSTRON 1026 (Figure 5.6) tensile loading frame at a displacement rate of $545 \mu m/min$ using pneumatic grips. Load data were recorded on a computer via a conditioner module with a precision of $0.1N$ while displacement accuracy was estimated at $0.1\ mm$.

(a) **(b)**

Figure 5.6 (a) INSTRON 1026 and (b) A tensile specimen during the tensile test.

During the tests, the force applied to the specimen and the corresponding elongation (extension) are recorded at a rate of about 50 points per second in the computer.

Once the test is completed, the UTS is calculated using the maximum force recorded for each specimen ($Load_{max}$) and the original cross-sectional area of the specimen (A_0). The formula for calculating UTS is:

$$UTS = \frac{Load_{max}}{A_0} \qquad (5.3)$$

Where:

- UTS the Ultimate Tensile Strength.
- $Load_{max}$ the maximum force applied during the test.
- A_0 the original cross-sectional are of the specimen.

And the Strain at maximum Load is calculated as it was refereed at eq. (5.2) as

$$\varepsilon_{max} = \frac{\Delta L}{L_0} \qquad (5.4)$$

Where:

- ε_{max} the strain at maximum load.
- ΔL the change in length of the specimen at maximum load (typically obtained from the testing machine).
- L_0 the original gauge length of the specimen (40mm).

By following these steps, the strain at maximum load and the UTS can be determined in accordance with ISO 527 for tensile testing of plastic.

5.1.2 Shore D Hardness

The hardness of a material using static hardness measurement methods and dynamic methods is determined by measuring the plastic deformation upon a compressive load, after subtracting the elastic recovery of the material [50]. Penetrant methods determine hardness based on the plastic deformation of the material, while dynamic stress methods relate hardness to its elastic response. The most commonly used static hardness measurement method for plastics is the Shore A or D scales where an indenter is pressed onto the surface.

Each scale provides a value from 0 to 100, with the higher value indicating greater hardness.

The Shore D hardness technique measures the depth of penetration of an indenter in relatively hard plastics, generally following the test standards ASTM D2240 [51] or ISO868 [10]. The Shore A scale is primarily suitable for measuring the hardness of soft elastomers and other polymers classified as soft. In contrast, the Shore D scale is used to measure the hardness of hard elastomers and most other hard polymers, such as thermoplastics and thermosets. An instrument called durometer is used for these measurements [52], [53].The Shore hardness measurement procedure involves the use of a hard indenter, a Calibrated Spring, a Graduated Dial with Indicating hand and an Indenter Foot. The Shore hardness measurement is determined by the depth the indenter penetrates under load. Shore hardness values range from 0 to 100, with the maximum penetration being $0.097 - 0.1$ *inches* $(2.5 - 2.54\ mm)$. A minimum Shore hardness corresponds to a maximum penetration, while a maximum hardness value of 100 corresponds to zero penetration [54].

Shore D hardness was measured on various points on the surface of 3D printed disc-shaped specimens with diameter 32 *mm* and thickness 7 *mm* using a hand-held durometer calibrated on the Shore D scale.

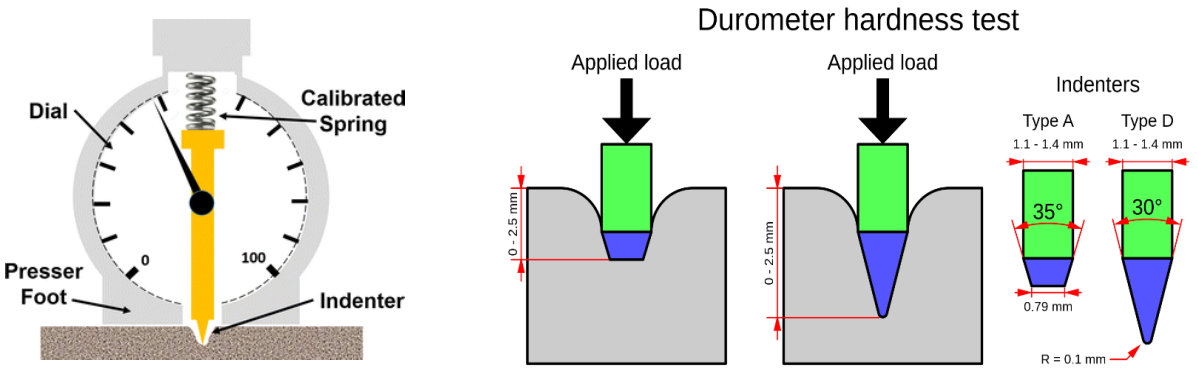

Figure 5.7 (a) Schematic of Shore D durometer with its components and (b) Diagram of a durometer indenter or presser foot used for Shores A and D [52].

The hardness measurement is determined by the depth that the pin penetrates under the load. According to ASTM D 2240 [51], values below 10 or above 90 are not considered reliable, so it is important to use a scale that allows measurements between 10 and 90 units [50].

The Shore D Durometer used in this work is shown below in Figure 5.8.

Figure 5.8 The Shore D durometer used for hardness measurement.

5.1.3 Mechanical Abrasion

Part of the characterization of the mechanical properties of the materials was the investigation of the dependence of material removal during grinding- using SiC abrasive paper with mesh size #1000.

The resistance of the materials to 2-body abrasion was investigated on specimens with diameter 32 mm and thickness 7 mm on an adapted rotating polishing facility, based on a STRUERS DAP-7 grinder/polisher with a PEDEMIN-2 specimen holder at 125rpm for 1 minute. Three specimens were tested together, and each specimen was loaded with 10N load (giving average stress on each specimen = 12kPa) and tested against a fresh #1000 SiC paper for 1 minute with continuous water supply to remove any loose particles and avoid 3-body abrasion. The specimens were dried at room temperature for 24 hours and weighed before and after testing to a precision of 1mg and the abrasion resistance is given by the reciprocal of the weight loss per unit specimen area with units m^2/kg.

The calculation of Abrasion Resistance is calculated as follows:

$$Abrasion\ Resistance\ \left(\frac{m^2}{kg}\right) = \frac{Area}{Mass} \qquad (5.5)$$

$$Abrasion\ Resistance\ \left(\frac{m^2}{kg}\right) = \frac{\pi R^2}{Weight_{Before\ \#1000} - Weight_{After\ \#1000}} \qquad (5.6)$$

Where $Weight_{Before\ \#1000}$ the weight of each sample before grinding with SiC #1000 abrasive paper and $Weight_{After\ \#1000}$the weight after grinding. Once this has been calculated for each sample, for each content we take the average of the change in mass of the three discs tests.

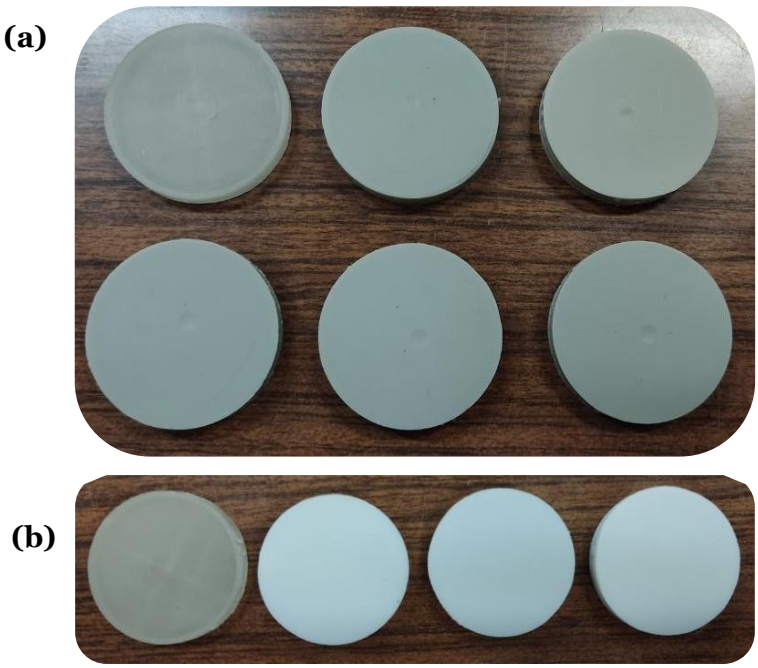

Figure 5.9 Disk-shaped specimens 32x6 mm for hardness test evaluations (a) PLA – 0,1,1.5,2,2.5,3wt% SiC and (b) PLA – 0,1,2,3wt% ZnO.

5.1.4 Hertzian Point Compression

In the mechanical engineering and materials science, the study of how surfaces interact under load is critical for the design and analysis of a myriad of mechanical components and systems. At the heart of this study lies the theory of Hertzian contact mechanics, a cornerstone concept that elucidates the behavior of elastic bodies in contact. The German physicist Heinrich Hertz was the one who formulated the foundational principles in the late 19th century, Hertzian contact mechanics provides the theoretical framework for predicting the stress distributions and deformations that occur when two curved surfaces come into contact under a compressive force[55]. An important observation, however, is that this theory does not consider surface interactions such as those near the point of contact (Van der Waals) [56].

Contact stress can cause surface friction, which is shown in Figure 5.10 . This effect could lead to degradation of accuracy over time and should be considered during the design process. All the calculation can be done using the classical solutions discussed below.

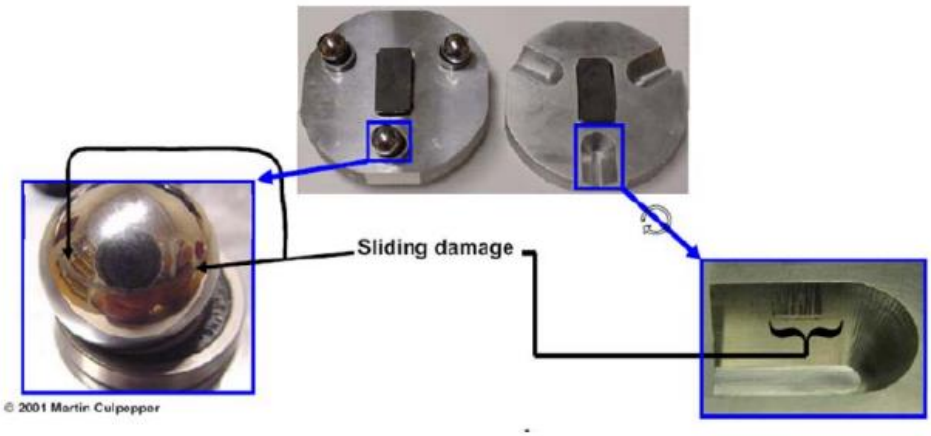

Figure 5.10 Effect of contact stress on kinematic constraint using spheres

An improved version of the aforementioned theory (Hertzian Contact Stress Theory) was the Johnson theory, around 1970, with the designation JKR (Johnson, Kendall, Roberts) theory. In this theory (JKR) the contact point is assumed to be 'stuck'. Therefore, we can conclude that it combines the contact point with the properties of an elastic material but taking into account the interaction force between the surfaces. As with the Hertzian Contact Stress Theory, in JKR Theory the solution is limited to the contact between elastic spheres [56].

In addition to the two theories mentioned above, a more complex theory (the DMT theory) considers the Van der Waals interactions outside the elastic contact point, but these cause some additional charge. This theory simplifies Bradley's van der Waals model if the two surfaces are separated significantly. In Bradley's model any elastic deformations of material because of attractive interaction forces are induced. The Bradley non-contact model and the JKR contact model have very specific limits explained by the Tabor coefficient.

In Figure 5.11 Hertz, JKR, Bradley and DMT are shown as contact stress theories.

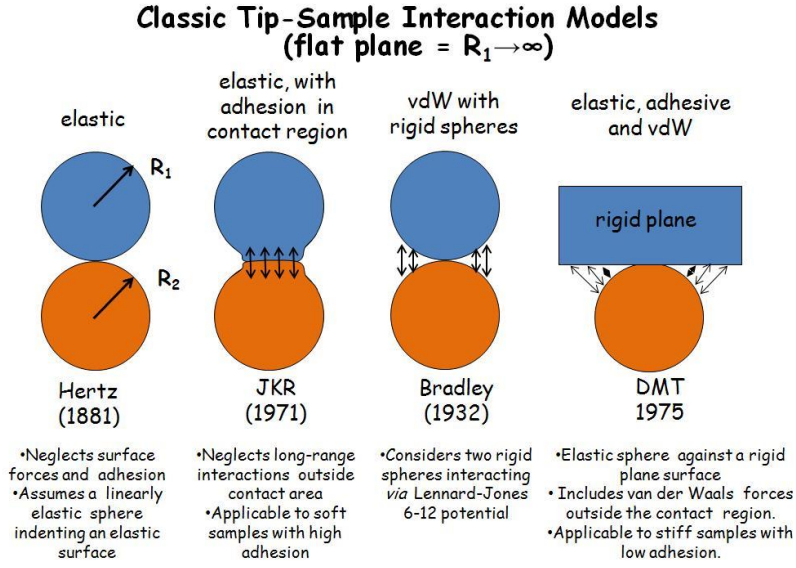

Figure 5.11 a Contact stress theories: Hertz, JKR, Bradley and DMT.

Where Hertz is the fully elastic model, JKR is the fully elastic model considering adhesion in the contact zone, Bradley is the purely Van der Waals model with rigid spheres and DMT is the fully elastic, adhesive and Van der Waals model.

The Hertzian Contact Stress Theory could be said to have some assumptions, focusing on the following [57]:

- Compression stress is generated when two non-conforming surfaces are in induced contact.
- The contact is a point or a line when there are no applied forces.
- The area of contact depends on the force exerted due to elastic deformation.
- Non-adhesive, meaning that the two surfaces do not require force to separate.
- The theory keeps both surfaces frictionless.

When two surfaces come into contact, they initially meet either at a point, defined as the point of contact, or along a line. A visually perceptible area of contact is formed between the two bodies when a small vertical load is applied because of surface deformation in the vicinity of the point of initial contact. This is highlighted due to the very small surface area in relation to the dimensions of the bodies touching. [58].

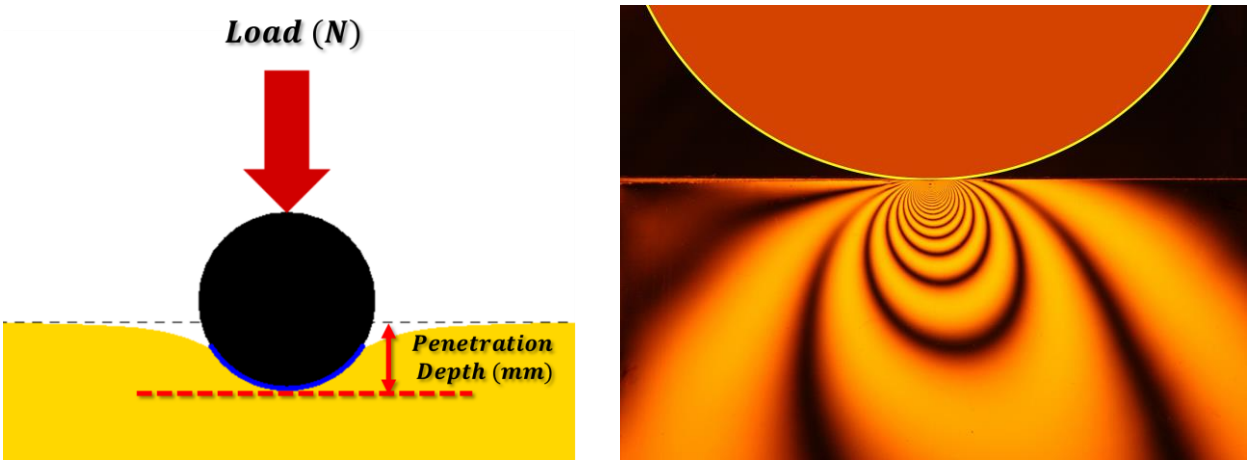

Figure 5.12 (a) Schematic of applied Hertzian Contact Theory and (b) Stresses in a contact area loaded simultaneously with a normal and a tangential force.

By carefully measuring the force and deformation parameters associated with the contact between the indenter and the specimen, as depicted in the Figure 5.13, we can derive insights to determine the hardness, stiffness, and other mechanical properties of the material models that underpin Hertzian contact mechanics. In a Hertzian compression test, the spherical indenter is pressed into the material of the disk to measure the material's response to contact stress.

The resistance of the materials to point loading was measured under “Hertzian point contact” loading conditions using a hardened steel pin with a radius of curvature of 2.5 mm at a displacement rate of 500$\mu m/min$ on an INSTRON 5982 loading frame (Figure 5.13). The specimens tested had a diameter of 32 mm and nominal thickness 7 mm and loading was recorded until the pin had

penetrated to a depth of 0.5 mm. The resistance to Hertzian point loading is given by the slope of the tangent to the load-depth curve at a penetration depth of 0.5 mm in units of N/mm, as shown later.

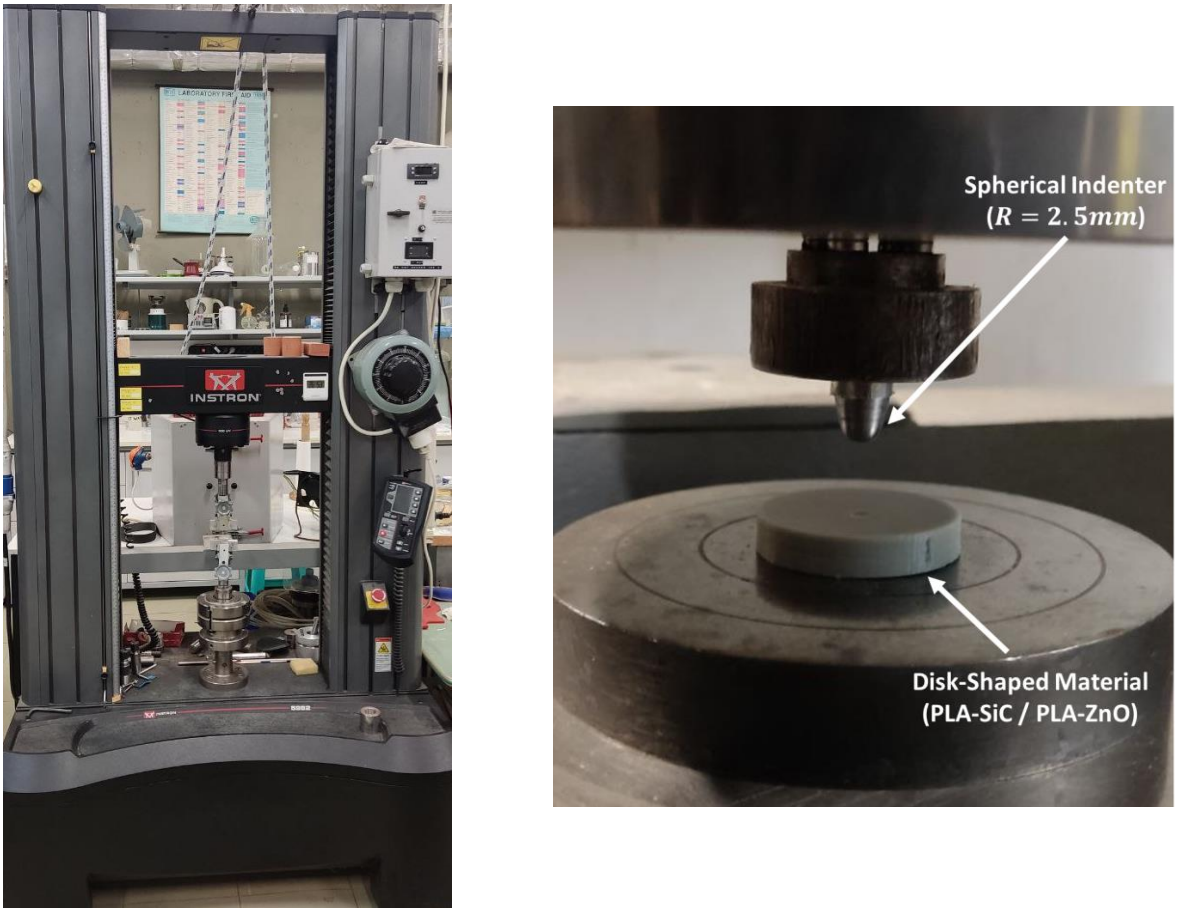

(a) **(b)**

Figure 5.13 (a) The INSTRON 5982 (100kN) and (b) The Hertzian point loading arrangement on it.

5.2 Mechanical Properties of PLA samples

The incorporation of nanoparticles into polylactic acid (PLA) presents an approach to tailor the mechanical properties of polymer composites. This chapter delineates a comparative analysis between silicon carbide (SiC)-doped PLA and zinc oxide (ZnO)-doped PLA, assessing the implications of each on the mechanical attributes such as tensile strength, hardness, abrasion resistance, and Hertzian compression resistance.

5.2.1 Tensile strength after mixed stress fatigue

At least 4 specimens with up to 3wt% SiC were tested under tensile loading before and after mixed-mode fatigue and the results are shown in Figure 5.14 (Raw data of Load and Extension), Figure 5.15 (a) (Ultimate tensile strength , UTS) and Figure 5.15 (b) (Strain at maximum load).

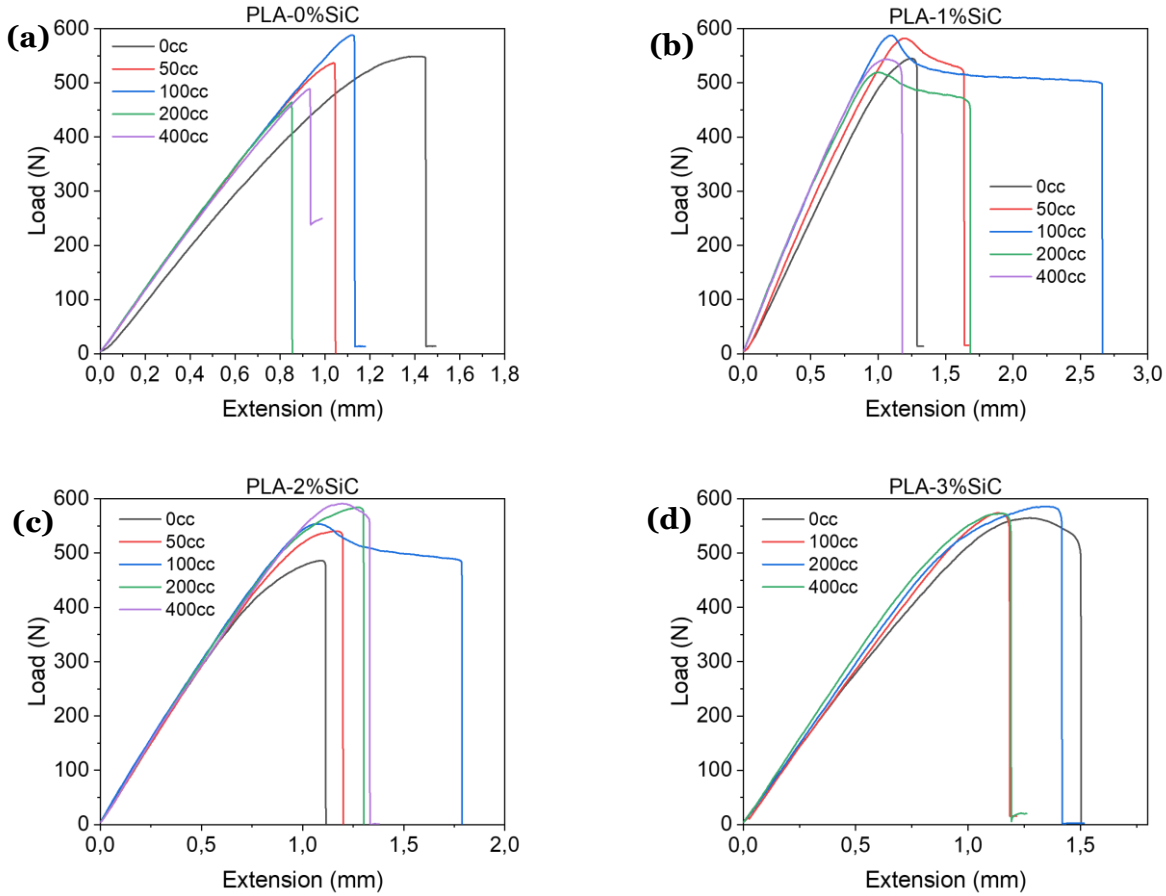

Figure 5.14 Load - Extension Curves after mixed-mode fatigue for 0, 50, 100, 200 *and* 400 *stress cycles for* (*a*) 0%, (*b*) 1%, (*c*) 2%, (*d*) 3% *SiC doped PLA* .

The UTS appears to decrease with number of fatigue cycles by about 10% after about 100 cycles for pure PLA and 1%SiC, probably by the accumulation of fine microcracks which results in localized stress concentrations. On the other hand, UTS appears to increase by about 10% after about 100 cycles when SiC doping increases to 2% or 3%, possibly because of entanglement of microcrack networks with the SiC particles which can reduce the localized stress concentrations by localized blunting. In addition, at SiC contents greater or equal to about 2%, the tangles of SiC particles can act as "anchors" for any microcracks growing during fatigue, delaying their development.

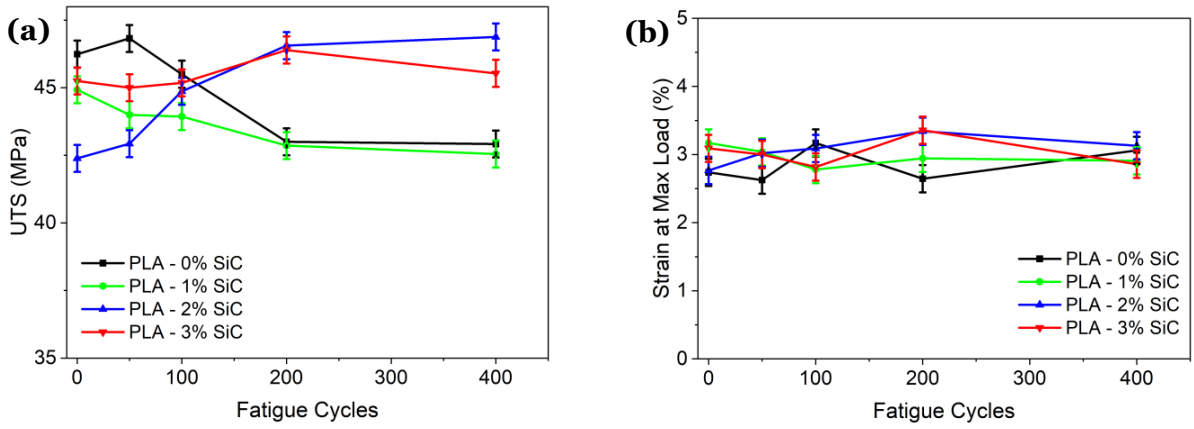

Figure 5.15 (a) Ultimate tensile strength of PLA composite and (b) Strain at max load of SiC-dopped PLA after mixed-mode fatigue for PLA-SiC.

This is an interesting result which shows that SiC content of about 2% has a beneficial effect on both the mechanical and the electrostatic properties, as shown later.

To elucidate the mechanical properties of 3*wt*% ZnO in comparison to pure PLA, at least 4 specimens were subjected to tensile loading without experiencing mixed-mode fatigue. According to Jamnongkan [59], ZnO the tensile strength of the PLA/ZnO biocomposite filaments gradually decreases when increasing the ZnO nanopowder contents. The results for tensile test of 3*wt*% ZnO are shown in Figure 5.16 (Raw data of Load and Extension).

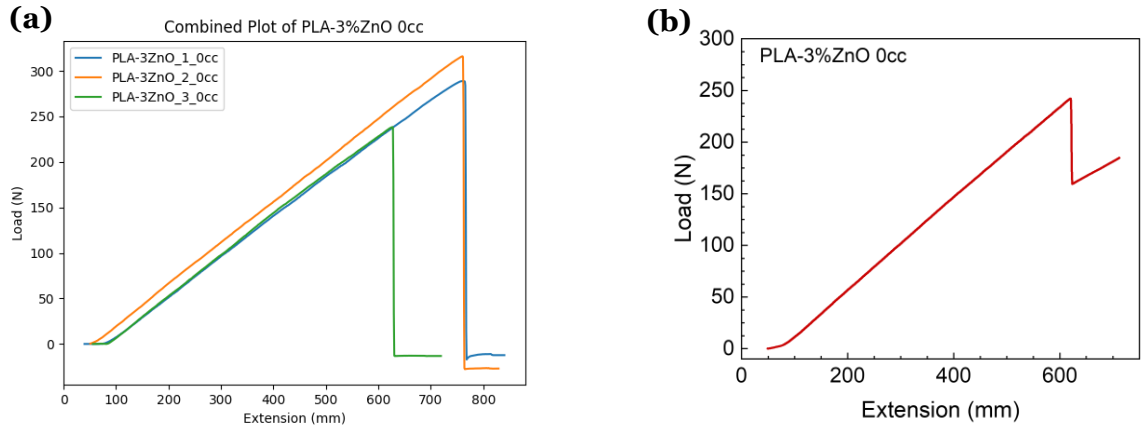

Figure 5.16 Load - Extension Curves without fatigue (a) specimens analytically (b) an average plot of them for PLA-SiC.

One reason where the tensile strength of PLA-ZnO decreases could be the agglomeration of nanoparticles. If ZnO nanoparticles are not evenly dispersed throughout the PLA matrix, they can form agglomerates. These agglomerations act as stress concentration points within the material, which can initiate cracks under tensile load, leading to a decrease in tensile strength.

Another reason could be the poor interfacial adhesion between the PLA pellets and ZnO nano powder. The effectiveness of load transfer between the polymer matrix and the nanoparticles depends on the interfacial adhesion between them. If the adhesion is poor, the nanoparticles cannot effectively reinforce the matrix, leading to a decrease in tensile strength.

5.2.2Shore D Hardness Measurements

The increase in tensile strength observed for SiC doping is confirmed by measurements of Shore D hardness shown in Figure 5.17 (a). Shore D hardness is relatively unaffected up to about 1% SiC but increases sharply thereafter and reaches a potential plateau at about 2.5%SiC.

The decrease in tensile strength but increase in Shore D hardness when adding ZnO nanoparticles to a polymer matrix, such as polylactic acid (PLA), can be attributed to the complex interactions between the nanoparticles and the polymer matrix, as well as the specific characteristics that these nanoparticles impart to the composite material.

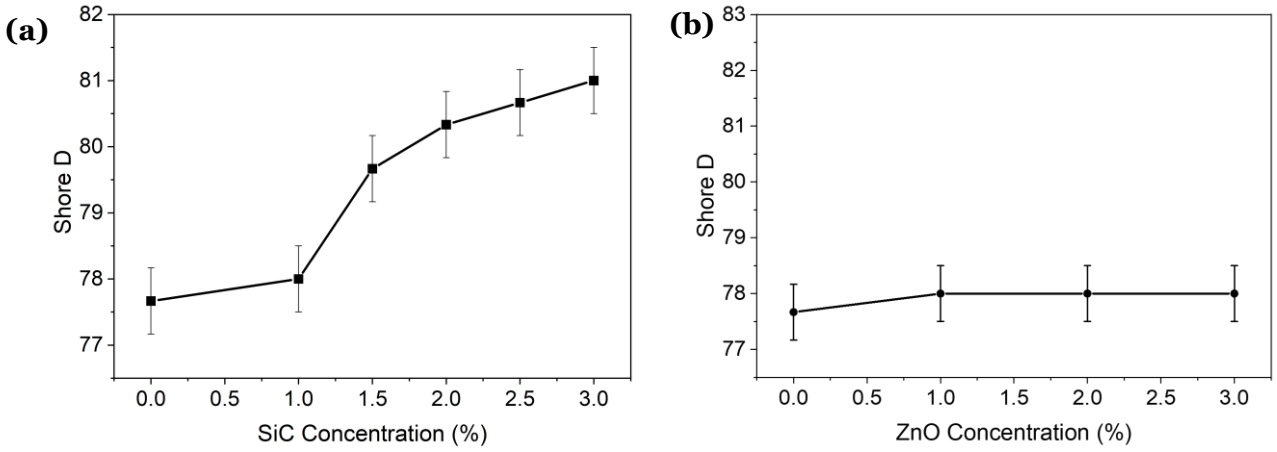

Figure 5.17 Results for Shore D hardness of (a) PLA-SiC and (b) PLA-ZnO.

ZnO nanoparticles decrease somewhat the stiffness of the PLA matrix. This stable stiffness results from the high modulus of ZnO particles compared to the polymer matrix, makes the composite material more susceptible to deformation and decreases its Shore D hardness.

5.2.3Abrasion Resistance

Significally, abrasion resistance increases sharply even with as little as 1% SiC since SiC is much harder than PLA and shields the PLA matrix from the abrading grains as shown in Figure 5.18 (a).

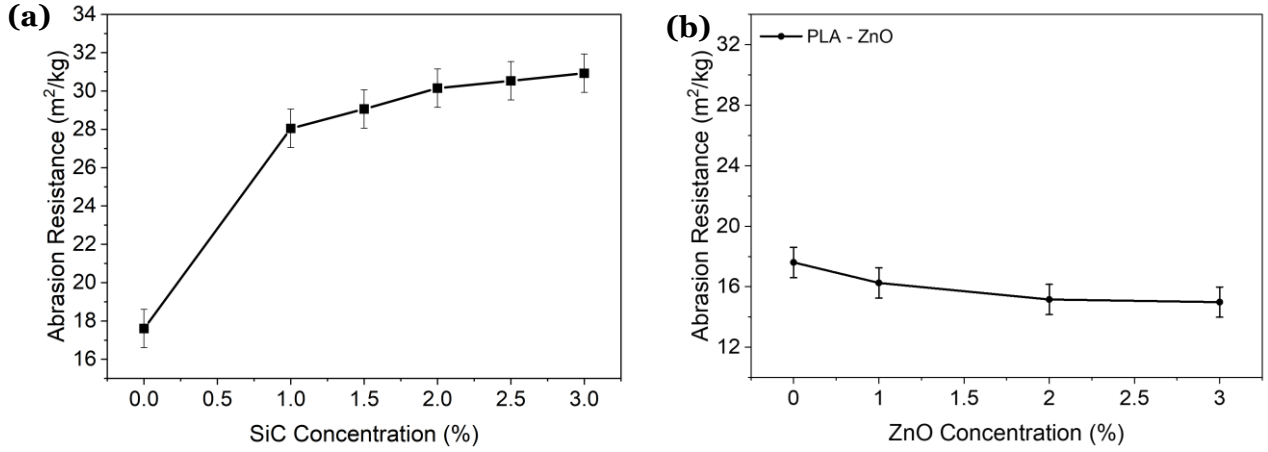

Figure 5.18 Results for Abrasion resistance of (a) PLA-SiC and (b) PLA-ZnO.

For PLA-ZnO, the decrease in mechanical properties (UTS) suggests potential negative effects on abrasion resistance, and this was confirmed by these tests. ZnO nanopowder was added, and it was discovered that this somewhat reduced the abrasion resistance as it is shown in Figure 5.18 (b).

5.2.4Hertzian Point Compression Measurements

The results obtained for Hertzian ball compression for SiC composites are shown in Figure 5.19 (a) (average load-depth curves) and Figure 5.19 (b) (average gradients). The gradient (slope, calculated between 0.3 and 0.45 *mm* penetration depth for all curves) of the load-depth curves can be considered as a measure of "effective hardness", i.e. plastic deformation and the results indicate

that the effective hardness increases after about 1 – 1.5% SiC reaching a plateau at about 2*wt*% SiC, about 40% above the value for pure PLA.

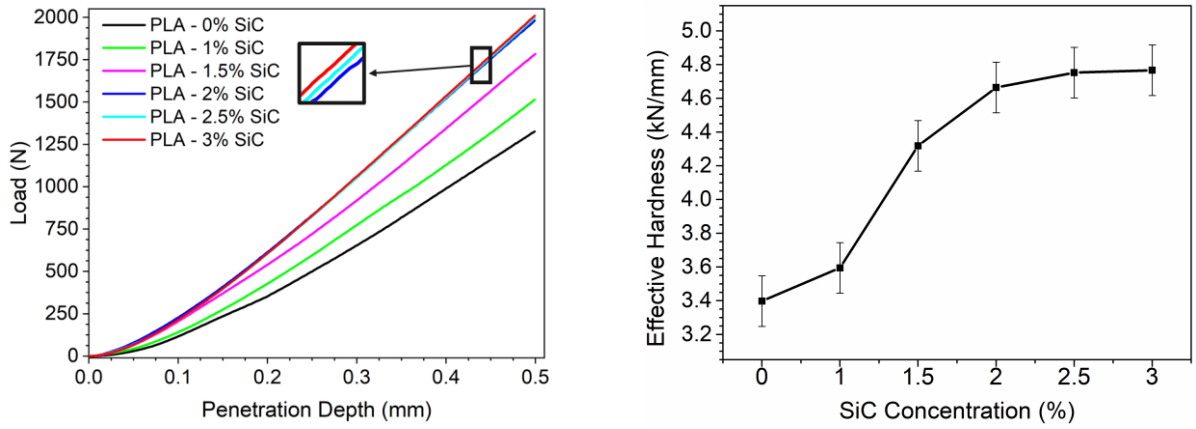

(a) **(b)**

Figure 5.19 Results for specimens with 1–3wt% SiC for (a) Hertz contact force with the compression test data and (b) effective hardness.

The increase in effective hardness after about 1 – 1.5% SiC is probably due to the obstacles presented by the networks of SiC particles to the plastic deformation of the PLA matrix. At only 1% the SiC particles are possibly too far from each other to form continuous networks, but by 1.5% the particles are close enough to each other to pre-sent relative barriers to further plastic deformation, increasing hardness.

The results obtained for Hertzian ball compression for ZnO composites are shown in Figure 5.20 (a) (average load-depth curves) and Figure 5.19 (b) (average gradients). ZnO nanoparticles, when added to PLA, tend to decrease both the tensile strength and the effective hardness of the material. The reduction in tensile strength could be due to factors such as particle agglomeration, as previously discussed, which can create weak points in the composite. The decrease in effective hardness suggests that the presence of ZnO particles alters the composite's response to compression, making it more susceptible to deformation.

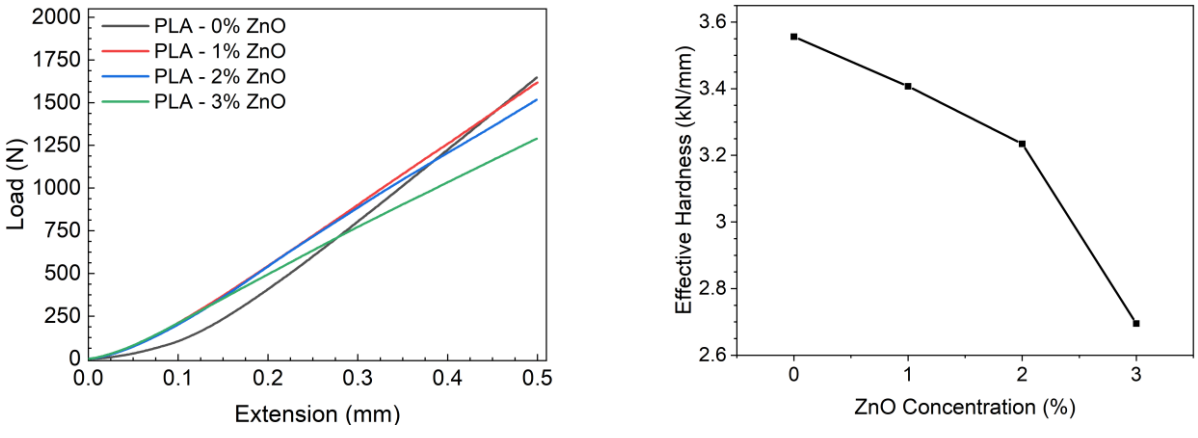

(a) **(b)**

Figure 5.20 Results for specimens with 1–3wt% ZnO for (a) Hertz contact force with the compression test data and (b) effective hardness.

The comparative analysis elucidates that SiC doping in PLA composites generally results in enhanced mechanical properties, improving tensile strength, hardness, and abrasion resistance, particularly at higher contents. The introduction of SiC appears to provide a structural benefit that fortifies the composite against various modes of mechanical stress.

In contrast, ZnO doping, while increasing the material's stiffness and hardness, does not positively influence the tensile strength or abrasion resistance.

5.3 Analysis & Discussion of Mechanical Characterization

In this chapter we investigated the influence of SiC microparticles and ZnO nanoparticles on the mechanical properties of SiC/ZnO-doped PLA. PLA composites were characterized using measurements of their tensile strength before and after fatigue, abrasion resistance, Shore D hardness and resistance to Hertzian ball loading.

The findings delineate that while both SiC and ZnO nanoparticles can be used to modify the properties of PLA, the overall impact on mechanical performance is highly contingent upon the nature of the filler, its interaction with the PLA matrix, and the resulting microstructural changes. These insights can guide the selection and optimization of nanoparticle reinforcements in PLA for specific applications where tailored mechanical properties are desired.

The summarized results for both SiC-doped PLA and ZnO-doped PLA are shown in Figure 5.21.

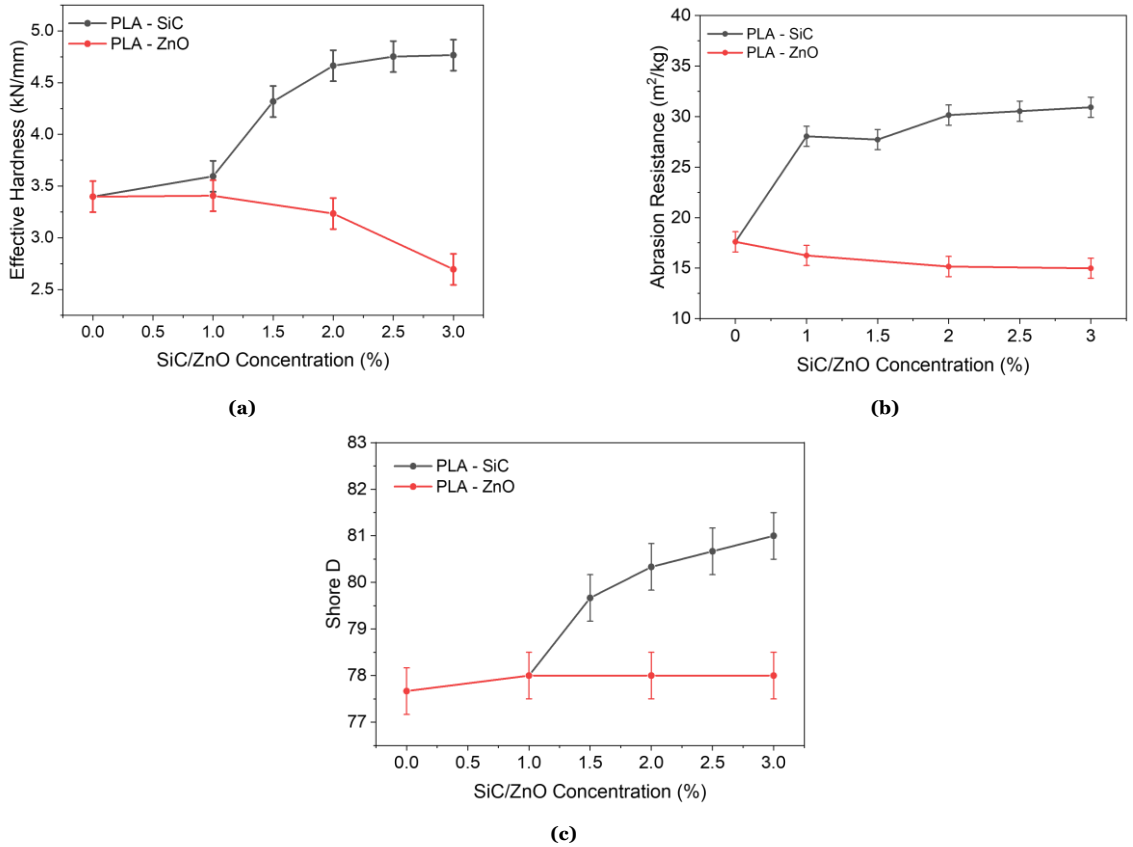

Figure 5.21 Comparison between SiC and ZnO doping on PLA-based samples for the mechanical characterization.

Our results show that by adding SiC microparticles in pure PLA enhances its mechanical properties. Hertzian ball compression experiments showed that the effective hardness increases after about 1% SiC reaching a plateau at about 2 *wt*% SiC, which is about 40% above the value for pure PLA. This increase in effective hardness is probably due to the obstacles presented by the networks of SiC particles to the plastic deformation of the PLA matrix. These results for the influence of SiC doping are confirmed by measurements of Shore D hardness as well as abrasion resistance experiments.

However, our findings show that the effective hardness of pure PLA drops when ZnO nanoparticles are added. Agglomeration of ZnO nanoparticles at high concentrations might result in the creation of weak spots in the material. It is difficult to disperse ZnO nanoparticles uniformly within the PLA matrix, particularly at high concentrations. A loss in total strength may arise from localized areas with inferior mechanical characteristics due to non-uniform dispersion. There was no need to test ZnO concentrations greater than 3*wt*% because it was found that the ZnO-doped PLA filament was extremely fragile and breaking at higher concentrations.

6 Electrical Characterization of Doped PLA

The Electrical Characterization was carried out in the Electrical Characterization Laboratory of the Institute of Nanoscience and Nanotechnology (INN) of the National Centre for Scientific Research "Demokritos".

6.1 Fabrication of Capacitors

For the fabrication of the capacitors used in the electrical characterization, cylindrical samples of 32 *mm* in diameter were 3D printed with the settings that described in chapter 4.2.2 and then polished for each different material with a #1000 SiC paper. The measured thickness for the SiC composites is given in Table 2 and for ZnO composites is given in Table 3. Thickness measurements were performed using a micrometer in different areas of each capacitor with a minimum graduation of 10 *μm*. For the electrical characterization, 200 *nm* thick Al contacts were deposited through a mechanical shadow mask on both sides of the samples, creating cylindrical parallel plate capacitors of 25 *mm* in diameter.

Figure 6.1 Photo of a PLA-3% SiC capacitor.

Table 2 Thickness measurements of the circular samples PLA-SiC used for the electrical characterization.

Sample	***Thickness* (*μm*)**	***δ Thickness* (*μm*)**
0% *SiC*	400	10.0
1% *SiC*	390	10.0
2% *SiC*	420	10.0
3% *SiC*	420	10.0

and

Table 3 Thickness measurements of the circular samples PLA-ZnO used for the electrical characterization.

Sample	***Thickness* (*μm*)**	***δ Thickness* (*μm*)**
0% *ZnO*	380	10.0

1% *ZnO*	385	10.0
2% *ZnO*	420	10.0
3% *ZnO*	415	10.0

6.2 Electrical Measurement Methodology

6.2.1 I-V Measurements

The measurements of the I-V characteristics in the samples of the experiment were performed using a probe station (probe station or prober) and with the help of an automated measurement system including the computer-controlled 4140B pA METER - DC Voltage Source of the Hewlett Packard company.

The control and acquisition of measurements is done through a computer which is connected to the measuring instruments via a shielded GPIB protocol cable. The measurements are obtained with the help of programs developed with the LabView software.

The prober has four probes, an optical microscope with four different magnification possibilities of the sample, a mechanical system to move the metal base in relation to the microscope and the pins in the x and y axes and a micrometric system to move the pins in the x, y and z axes. As shown in figure 8, one probe was utilized for the upper surface of each sample, and a copper chuck probe was used for the sample's other side.

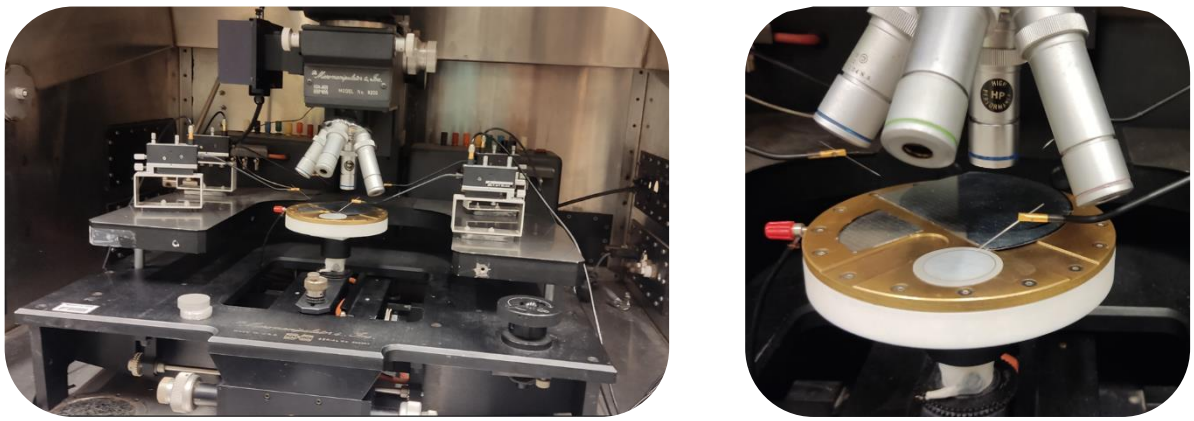

(a) **(b)**

Figure 6.2 The probe station used for the electrical characterization of the samples

First, we carefully place the spike on the aluminum surface of the sample and close the Faraday Dark Box of the station to avoid any dirt from the external environment. The electrical interface between the instrument and the sample is made using BNC coaxial cables which are electrically connected to the external terminals of the test probe station which are connected to the test probe used.

The settings for all the measurements implemented were performed for a range from -2 to 2V with a step of 100 mV, with V_A I limit set to 10 μA and voltage source mode set to single staircase. Finally, the program was used to obtain the measurements of the current intensity I versus voltage.

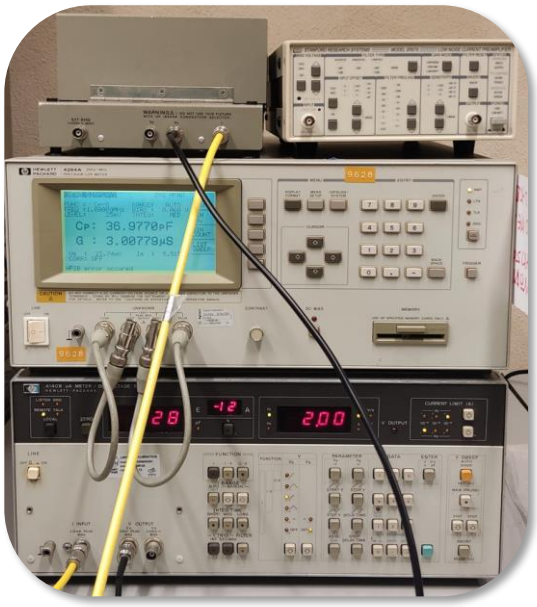

Figure 6.3 HP 4140B pA METER and HP 4284A LCR METER

6.2.2C-V Measurements

C-V measurement is a way to find the electrical characteristics of the device being studied such as its capacitance, dielectric constant, and conductivity. LCR instruments operate by applying an AC voltage to the device under test (DUT) and measuring the resulting current, both in terms of amplitude and phase, with respect to the AC voltage signal. With this applied voltage a variation in the device load ΔQ occurs and through this the capacitance of the device is calculated.

Capacitance measurements were used to calculate each specimen's dielectric constant using the equation (6.1) :

$$C_x = \frac{\varepsilon_o \cdot \varepsilon_x \cdot A}{d} \qquad (6.1)$$

where C_x is the measured capacitance, $\varepsilon_o = 8.854 \cdot 10^{-12} CV^{-1}m^{-1}$ is the dielectric permittivity of vacuum, ε_x is the composite material dielectric constant, A is the capacitor area ($\pi \cdot 12.5^2 mm^2$) and d is the material thickness. So, the dielectric constant for each sample is calculated as

$$\varepsilon_X = \frac{C_X \cdot d}{\varepsilon_0 \cdot A} \qquad (6.2)$$

as it is shown in Figure 6.4.

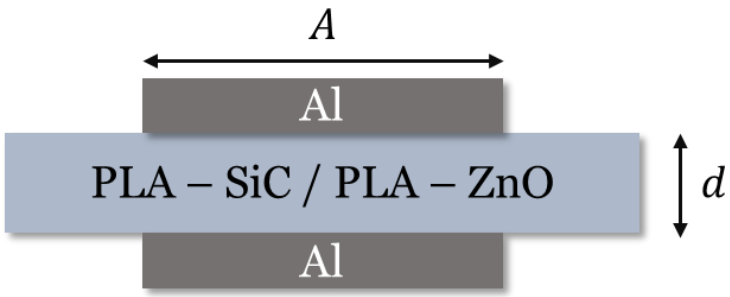

Figure 6.4 Illustration of capacitor.

The HP 4284A LCR METER from Hewlett Packard and the prober spike station were used for the C-V measurements. Measurements at 100 Hz contain a lot of noise, as the signal forwarding network operates at 60 Hz and the devices connected to it cause interference to the C-F and C-V measurements.

The settings for all measurements implemented were done through the HP4284A Bias Step Measurement1.vi program with a voltage range of -2 to 2V with 100 mV step, with Trigger Source External and the frequencies of 100 Hz, 1 kHz, 10 kHz, 100 kHz, 1 MHz were tested.

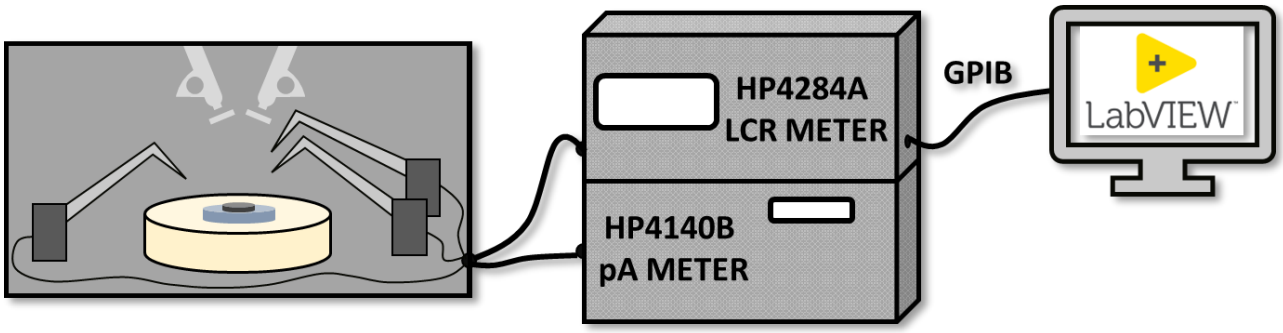

Figure 6.5 Electrical Measurement's process: from prober to HP4284A & HP4140B via coaxial cables and from them to computer via GPIB cable.

6.2.3C-F Measurements

The data required for the investigation of a material's conductive and dielectric characteristics was supplied by C-F measurements. C-F measurements evaluate how the capacitance of the MIM capacitor changes with frequency. This can provide insights into the dielectric relaxation processes and the response time of the dielectric material. The C-F curve is analyzed to determine the frequency response of the dielectric material, which can reveal information about the polarization mechanisms and the dielectric relaxation time.

The HP 4284A LCR METER from Hewlett Packard and the prober spike station were used for the C-F measurements. The connectivity is the same as that included in the C-V measurement methodology.

The settings for all the measurements implemented were with logarithmic adjustment in the frequency range from $100Hz$ to $1MHz$, with Trigger Source External and a range from $-2V$ to $2V$. Finally, through the program the measurements of capacitance, conductance versus voltage is taken.

6.3 Characterization of Capacitors

6.3.1 I-V measurements

The leakage current (I) as a function of applied voltage (V) for all samples is presented in Figure 6.6. The current was measured for voltage ramps starting at $0V$ and going to $+10V$ and back to $0V$ and then to $-10V$ and back to $0V$. The results presented in Figure 6.6 reveal that the magnitude of the leakage current is at the noise floor of our measurement system which is almost $5 \cdot 10^{-13}A$. We can then use our samples' dimensions to calculate the resistivity of the PLA composites examined. By doing so, we conclude that the resistivity is larger than $6 \cdot 10^{14}\Omega cm$ for all composites. This value is consistent with reports on the volume resistivity of pure PLA ranging from $5 \cdot 10^{14}\Omega \cdot cm$ [11] up to $4 \cdot 10^{17}\Omega cm$ [12].

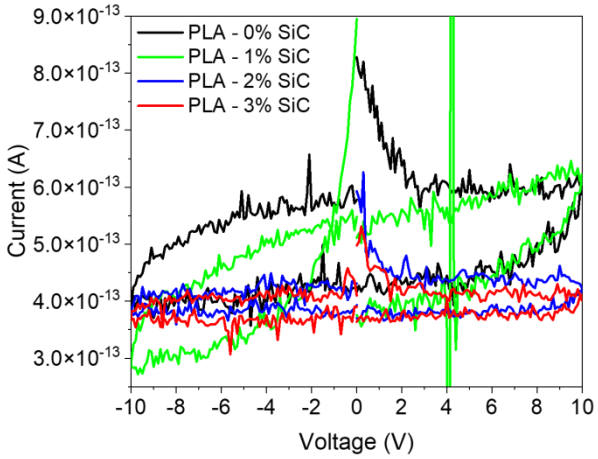

Figure 6.6 Leakage current as a function of applied voltage for all samples. The measurements were performed using voltage ramps going from +10V to 0V to -10V to 0V.

Another interesting observation concerning the leakage current is that there is a hysteresis of the current voltage curves with respect to applied bias. This hysteresis must be due to charge trapping within the PLA material. Interestingly, the addition of SiC, seems to reduce the perceived trapping without increasing the leakage current and, thus, the volume resistivity of the composite material. In fact, the resistivity seems to decrease with increasing SiC content, even though the measurements are very close to the noise floor of our instrumentation and the SiC content is smaller than usually reported additive contents [11], [12]. We need to stress at this point that SiC is not a conducting material, which is a significant difference between these cases and other reported additives in PLA in the literature.

6.3.2C-V measurements

A characteristic example of a capacitance versus voltage measurement at voltage range from -2V to 2V for all samples appears in Figure 6.7 for SiC doped PLA samples. As would be predicted given the voltage range of the observations, the capacitance is nearly constant. More significantly, though, there is a noticeable variation in the capacitance values between the samples.

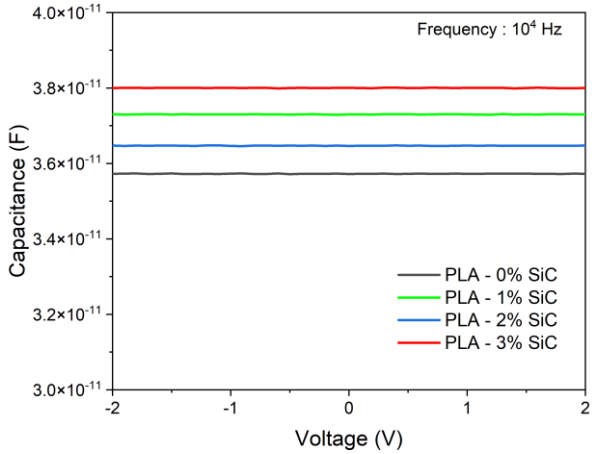

Figure 6.7 Capacitance vs Voltage at 10^4Hz frequency for all samples PLA-SiC.

The dielectric constant from the C-F measurements will be computed for all samples from 0 to 3*wt*% SiC in the upcoming chapter and it will also be observed that data from C-F and C-V agree.

Figure 6.8 shows a typical example of a capacitance versus voltage measurement for all samples at a voltage range of -2*V* to 2*V* for ZnO doped PLA samples. The dielectric constant from the C-F measurements will be computed for all samples from 0 to 3*wt*% ZnO in the upcoming chapter and it will also be observed that data from C-F and C-V agree.

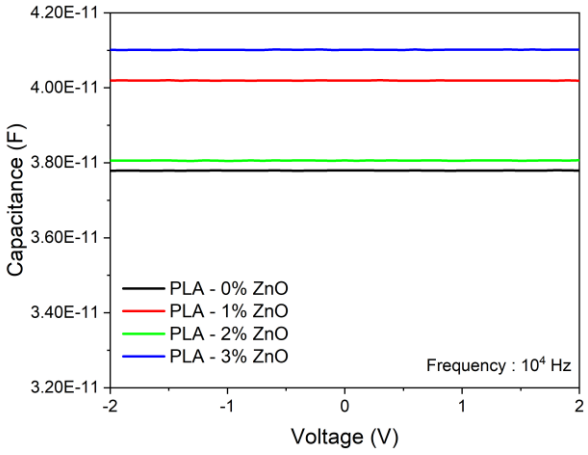

Figure 6.8 Capacitance vs Voltage at 10^4Hz frequency for all samples PLA-ZnO.

6.3.3C-F measurements

A characteristic example of a capacitance versus frequency measurement at 0 bias voltage for all samples appears in Figure 6.9 (a). It can be seen that the capacitance is almost constant, as expected

for the frequency range of the measurements. Small variations of the capacitance of each sample are most probably due to the presence of interface charge traps between the PLA and Al. More importantly, though, a distinct difference in measured capacitance exists between the samples.

Using the measured capacitance at 10 *kHz*, the dielectric constant for each sample was calculated using eq. (6.1). The results are presented in Figure 6.9 (b). The error bars have been calculated using the error associated with the material thickness measurement.

A clear increase in dielectric constant with SiC concentration can be seen from Figure 6.9 (b). The dielectric constant of PLA with 0% SiC is measured to be 3.2, which is a little higher than previously reported values ranging from 2.5 to 3.11 [7], [8]. This value increases monotonically with SiC concentration, to 3.87 for the PLA with 3% SiC sample. Considering that the SiC has a dielectric constant of almost 15 [9], in its powder form, the observed increase in dielectric constant with SiC concentration is not surprising. In fact, this type of effect has been shown in the literature for a variety of material shapes [10].

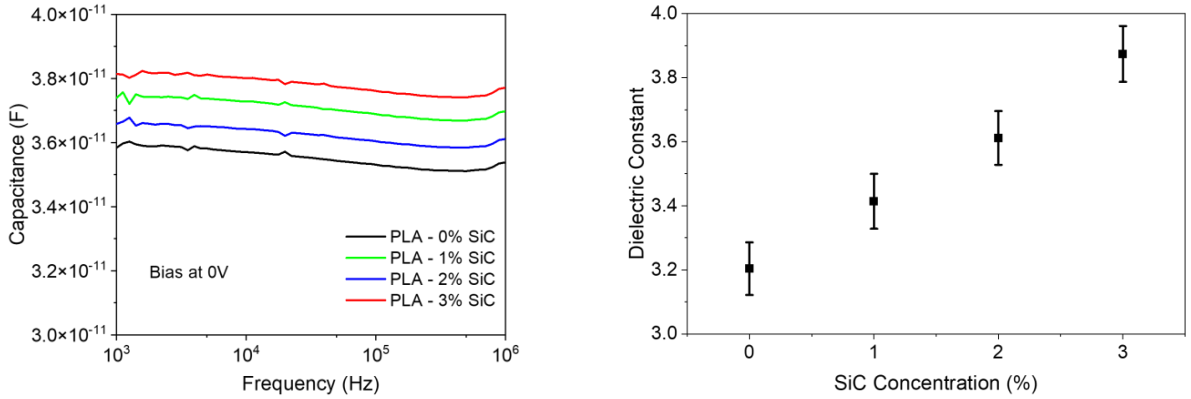

Figure 6.9 (a) Capacitance vs frequency at zero bias voltage for all samples PLA-SiC and (b) Dielectric constant of the PLA-SiC composite material as a function of SiC concentration

A measurement of a capacitance versus frequency measurement at 0 bias voltage for all samples PLA-ZnO appears in Figure 6.10 (a). The capacitance is almost constant, as it was noticed for PLA-SiC samples, as expected for the frequency range of the measurements.

Using the measured capacitance at 10 *kHz*, the dielectric constant for each sample was calculated using eq. (6.1) and the results are presented in Figure 6.9 (b). The error bars have been calculated using the error associated with the material thickness measurement.

Figure 6.10 (a) shows the capacitance as a function of the frequency at zero bias for the ZnO-doped samples. We notice that the capacitance is almost constant for all frequencies, with small variations that can be attributed to Al/PLA interface charges. The variation in the capacitance values can be attributed to variations in capacitor thickness (Table 3) as well as the dielectric constant.

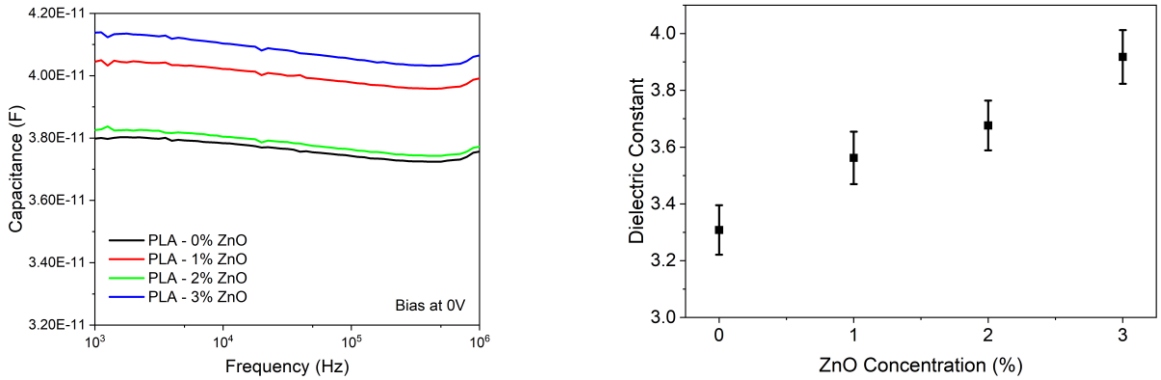

(a) (b)

Figure 6.10 (a) Capacitance vs frequency at zero bias voltage for all samples PLA-ZnO and (b) Dielectric constant of the PLA-ZnO composite material as a function of ZnO concentration

Taking the measured thickness values and the capacitance values at 10 kHz into account, we can calculate, by using eq. (6.1), the dielectric constant as a function of ZnO doping. The results are shown in Figure 6.10 (b). We notice that the dielectric constant of the ZnO-doped PLA increases monotonically from 3.3 for undoped PLA to 3.9 for 3%ZnO-doped PLA. Such behavior has been reported in the literature when materials of various shapes are immersed in a matrix [10] if the dielectric constant of the inclusions is higher compared to the host matrix. This applies to our case, since the dielectric constant of ZnO nanoparticles is about 10 [18] , much higher compared to the dielectric constant of PLA.

6.4 Analysis & Discussion

Regarding the influence of SiC microparticles on the electrical properties of PLA composite a clear increase in the dielectric constant was observed. The dielectric constant of PLA increased monotonically with SiC from 3.2, for pure PLA, to 3.8 and with ZnO to 3.9, for PLA doped with 3% SiC/ZnO.

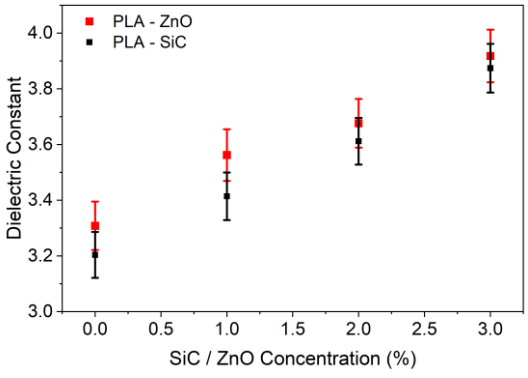

Figure 6.11 Dielectric Constant of PLA composites with various concentrations of SiC and ZnO.

Moreover, the resistivity of all composites is larger than $6 \cdot 10^{14} \Omega cm$, indicating that the addition of SiC does not deteriorate the insulating properties of PLA. An hysteresis of the current voltage curves with respect to applied bias was observed. This is maybe due to charge trapping within the PLA material. The addition of SiC and ZnO appears to decrease this charge trapping without increasing the observed leakage current and thus the dielectric properties of the PLA material.

7 Assembly and Characterization of Tribogenerators

The Triboelectric Characterization was carried out in the Energy Harvesting and Autonomous Sensors Laboratory of the Institute of Nanoscience and Nanotechnology (INN) of the National Centre for Scientific Research "Demokritos".

7.1 Construction of tribogenerators

The triboelectric nanogenerators used in this study operate according to the contact-separation mode. Cylindrical samples, with a diameter of 32 mm, were 3d printed using a CREALITY CR20 Pro 3D printer and the aforementioned doped PLA filaments. The specimens that were used in this study were fabricated with the produced filament. A grinder/polisher (STRUERS DAP-7) was used to polish the 3D printed samples using #1000 SiC paper until they reached a thickness of about 390 μm. A constant water supply was used to eliminate any remaining particles. Following that, the samples were cleaned with absolute alcohol and dried.

As a reference triboelectric surface, a 75 μm-thick Kapton® layer (DuPont™) was cut from a large sheet at a dimension of $2x2\ cm^2$. Each triboelectric surface was mounted on hexagonal PCB sample carriers using double-sided aluminum conductive tape, completing a triboelectric pair, shown in Figure 7.1. The PCB carrier boards contain a contact pad on the backside providing the electrical contact for the triboelectric surfaces.

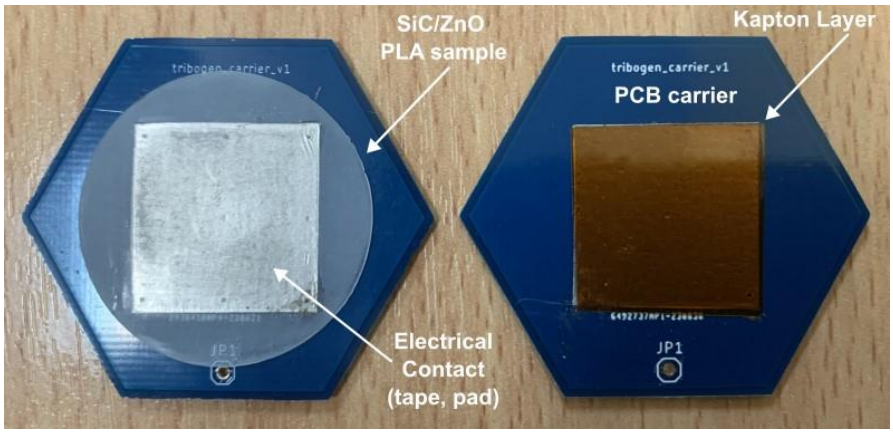

Figure 7.1 PCB carrier for mounting the fabricated materials and the Kapton films, used as the reference surface, for the triboelectric characterization.

7.2 Description of experimental set-ups

7.2.1 Horizontal Contact-Separation

For the periodic motion of the triboelectric surfaces two in-house systems were used as shown in Figure 7.2 (c).

This in-house experimental setup used for triboelectric characterization of the produced pure PLA, SiC-doped PLA and ZnO-doped PLA samples at horizontal contact-separation mode works with a motor that starts and moves the dynamic holder towards the static holder. The motor's rotation is converted into linear motion through a screw system. The dynamic holder contacts the specimen placed in the static holder. The pressure applied during this contact can be controlled and measured. After the initial contact, the system waits for a predefined delay (in this case, 250 ms). During this time, the physical and electrical effects of the contact are taking place—generating a triboelectric charge. After the delay, the dynamic holder retracts, separating from the static holder. The separation can also generate tribological or triboelectric effects. This press-and-release process can be repeated multiple times with a frequency 2 Hz to simulate wear over time or to generate more electrical charge through continuous contact and separation.

In this setup, using a load cell and the oscilloscope it may be recorded various data points such as force, displacement and electrical charge during each contact and separation cycle. The collected data is obtained from LabView software and then analyzed to understand the characteristics of the materials or to optimize the energy generation through the triboelectric effect.

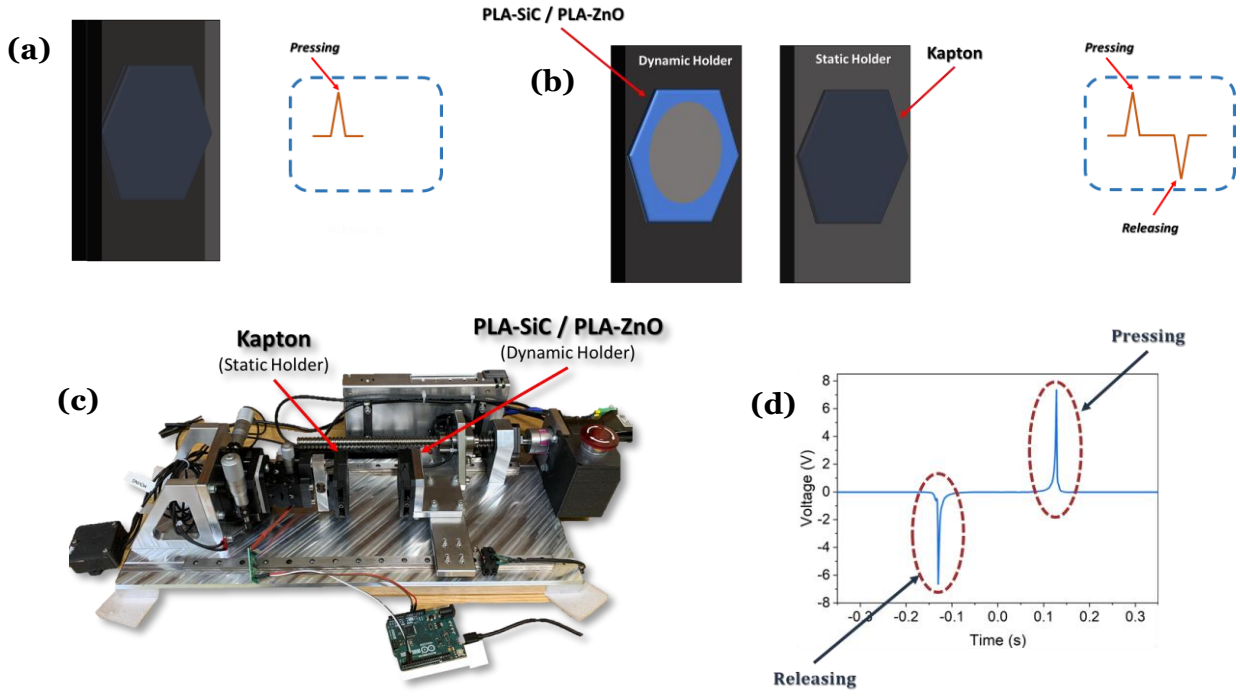

Figure 7.2 (a) Tribogenerator's pressing and (b) releasing signal and (c) the in-house horizontal contact separation system and (d) direct signal from the in-house system.

7.2.1.1 Triboelectric Signal Optimization

For tribo tapping, it is necessary to set which is the relative zero of contact of the two parallel plates. Initially, we place a sheet of paper with a thickness of approximately 100 μm between the two plates and assume that they come into contact when the sheet is securely maintained.

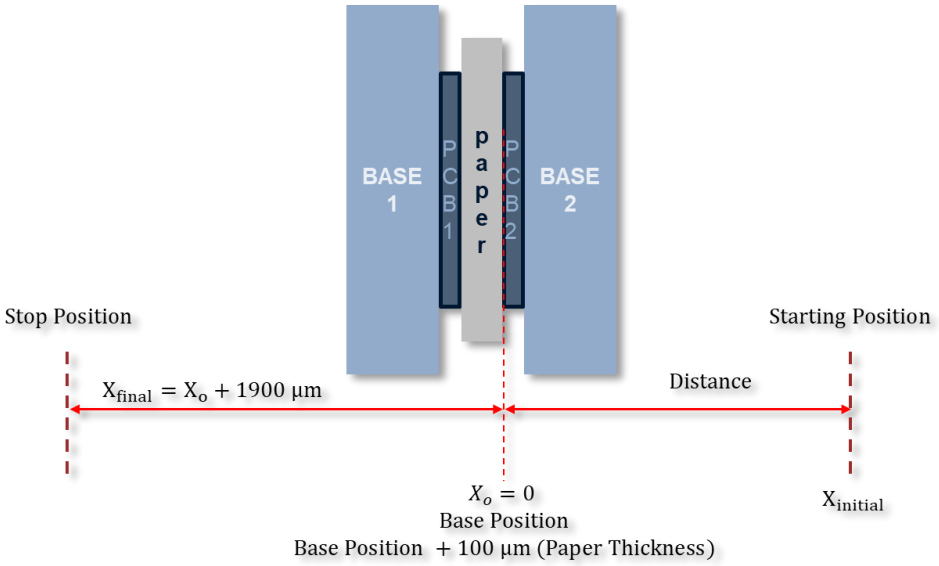

Figure 7.3 Schematic of contact of two plates.

After investigation, when the dynamic plate shifts +1900 μm after the relative zero, as previously mentioned, the two plates can hold the paper sheet. At that moment, the oscilloscope records the maximum triboelectric signal.. (see Figure 7.4). The measurements were made adding each time +100 μm to that distance.

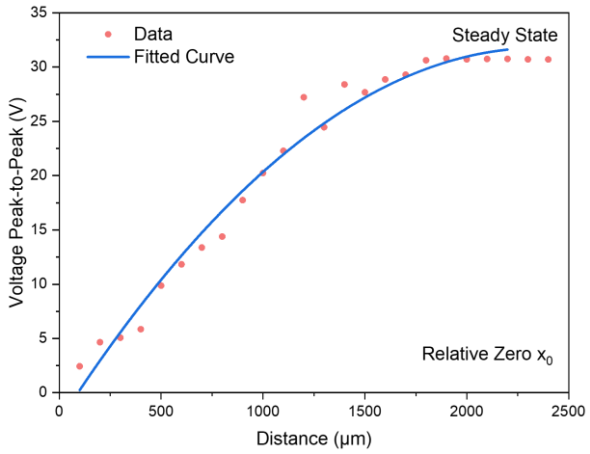

Figure 7.4 Triboelectric signal dependence on the stop position of tapping.

This can be explained by the fact that when the force between the two plates increases the triboelectric signal increases as well. However, at force values greater than this, the triboelectric signal stabilizes, leading to a steady state.

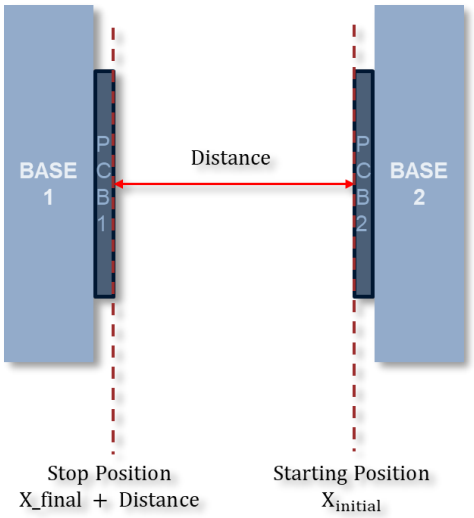

Figure 7.5 Schematic when the two PCBs are in their initial positions.

The triboelectric signal optimization's reliance on the separation between the two PCBs for tapping is another thing to note. When the tapping distance is more than 3000 μm, the triboelectric signal is in a steady state.

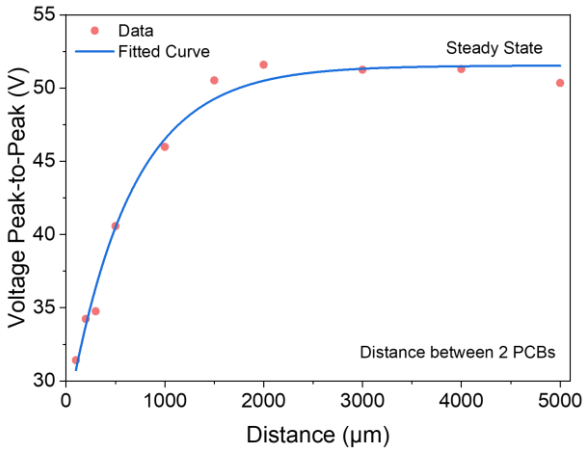

Figure 7.6 Triboelectric signal dependence on the tapping distance.

7.2.2 Vertical Contact-Separation

Capacitor charging was performed with the system shown in Figure 7.7 (b).

The setup includes a motor that is responsible for driving the movement of the dynamic holder. It can move the holder vertically to contact the material on the static holder. The dynamic holder, attached to the motor, moves downward to press the material against the static holder and then retracts, following the motor's motion. This is the part that taps with a frequency 2,5 Hz. The static holder holds the material in place as the dynamic holder taps it.

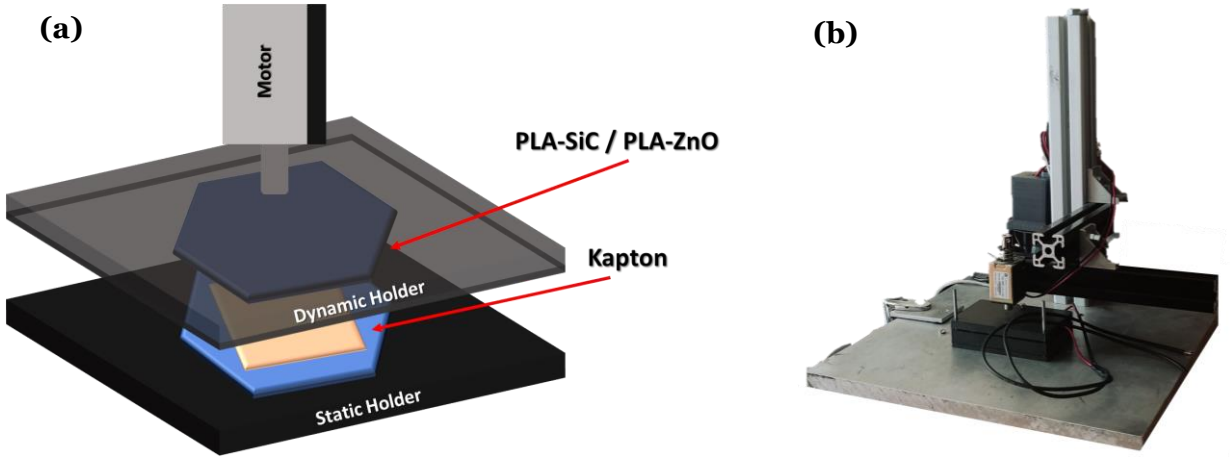

Figure 7.7 (a) Schematic of tribogenerator and (b) the in-house vertical contact separation system.

7.2.3 Instantaneous Electrical Signal Measurement

The instantaneous electrical signal for each sample was measured using the horizontal contact separation system as shown in Figure 7.2.

The voltage was measured by the laboratory InfiniiVision DSO7104A oscilloscope (Agilent Technologies) for about 20 minutes with frequency 2 Hz for each composite material to capture the instant signal of triboelectric effect and data was obtained from LabView and analyzed using python program.

7.2.4 Capacitor Charging

The development of energy-generating microstructures opens the door to the potential for self-sufficient electronic devices. Therefore, the development of circuit devices that gather electrical signals and convert them into usable form for charging devices or storage systems becomes necessary. When triboelectric nanogenerators are used, the voltage-current that is produced takes the form of an alternating signal since the peaks have opposite polarity. Direct current [60] is needed to charge electronics. A passive rectification circuit was built to store the energy generated by the triboelectric generators. The following circuit components were utilized to build the rectifier bridge circuit:

- 4 x Silicon diodes: $1N4148$, forward voltage, $V = 0.7\ V$
- 1 x Capacitor Storage, $C = 0.47\ \mu F$

The energy harvesting device's whole connection is depicted in the Figure 7.8. Similar to how the storage capacitor was linked to the rectification circuit's output, the triboelectric nanogenerator was connected in parallel to the quad bridge rectifier circuit' input.

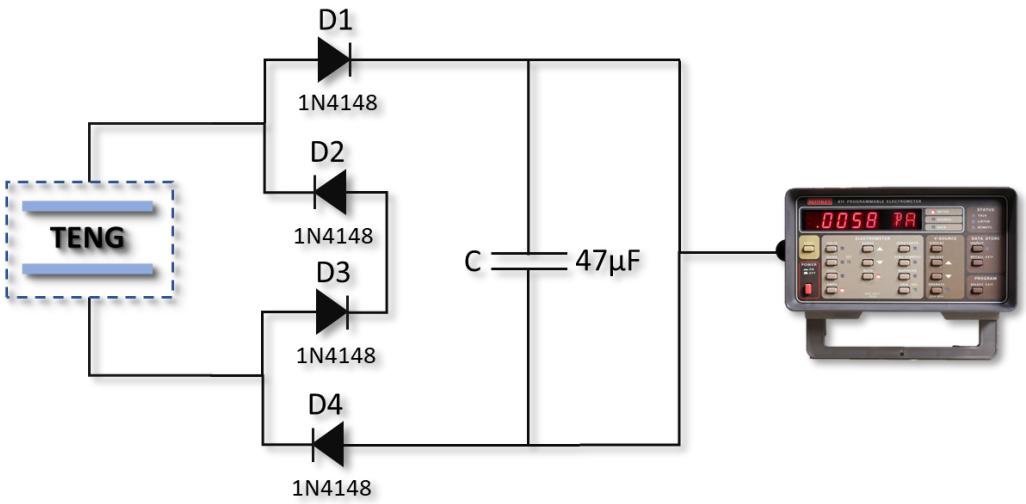

Figure 7.8 Energy harvesting circuit schematic: tribo-generator, rectifier bridge circuit, storage capacitor, Keithley 617 electrometer.

The selected system for the capacitance voltage measurements is depicted in Figure 7.7, with the selected mode being vertical contact separation as appeared in Figure 7.7.

The quad bridge rectifier circuit is the intermediate stage between the tribogenerator and the energy storage capacitor. To derive the characteristic capacitor charging curve for each of the dielectrics, the tribogenerator was set in vertical contact mode. The voltage was measured by the laboratory Keithley 617 electrometer for about 20 minutes for each composite material.

The capacitor is charging itself from ambient noise if the value on the display changes. The rectifier is covered in metal just in case, protecting the grounds and preventing noise.

The measuring data was obtained via LabView software from Keithley 617 and every measurement was made with frequency of 5 *Hz* (200ms on-off time).

7.2.5 Open Circuit Voltage Measurement

For the estimation of the open circuit voltage as a function of an external load, the Open Circuit Voltage the methodology developed by Jayasvasti et al. [13] was applied.

This method was created to deal with the measurement issue that arises when an oscilloscope operates as an open circuit measuring device too much less than optimally. Thus, Kirchhoff voltage law might be used to calculate the electrical metrics of the setup (see Figure 7.9) of our method for measuring the voltage across a resistor divider inserted parallelly [13].

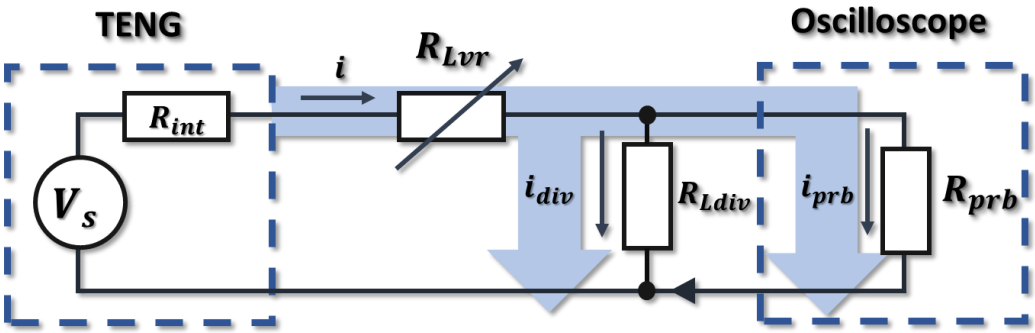

Figure 7.9 Schematic diagram of the conventional measuring technique.

Where:

- R_{Lvr} is Variable load resistor.
- R_{Ldiv} is Voltage-divider load resistor.
- i_{div} is Voltage-divider load current.

With this technique, the voltage across the divider resistor, Vread, was the actual voltage that the oscilloscope measured. In order to determine the theoretical voltage that the TENG produces across the load resistor, V_{out}, equation (7.1) was derived from Kirchhoff law [13]:

$$\mathrm{V_{out}} = \frac{V_{read}\ x\ R_L}{R_{Ldiv} // R_{prb}} \qquad (7.1)$$

$$\mathrm{V_{out}} = \frac{V_{read}\ x\ (R_{Lvr} + (R_{Ldiv} // R_{prb}))}{R_{Ldiv} // R_{prb}} \qquad (7.2)$$

The hands-on wiring of the Figure 7.9 is shown in Figure 7.10 :

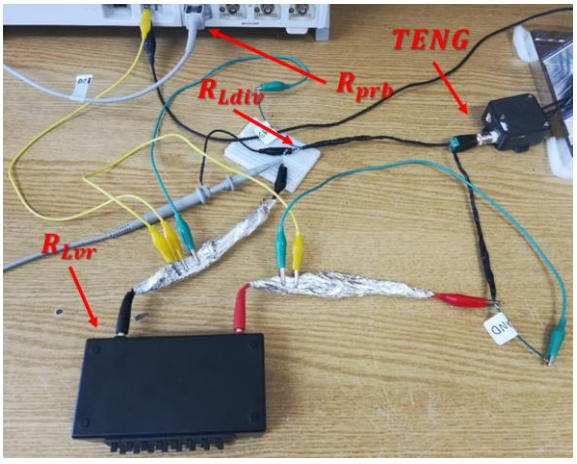

Figure 7.10 Voltage divider circuit wiring after the extra grounds.

The output (black wire) of the variable resistance box is connected to one end of the 1 $M\Omega$ resistor that is placed on a breadboard. The 1 $M\Omega$ is the R_{Ldiv} of the Figure 7.9.

7.2.6 Short Circuit Current Measurement

The Short Circuit current was measured with an in-house-assembled current preamplifier comprising of a simple current-to-voltage converter circuit (transimpedance amplifier, TIR) [61] .

The short circuit current measurement circuit is called transimpedance and is given by the following schematic Figure 7.11 (a):

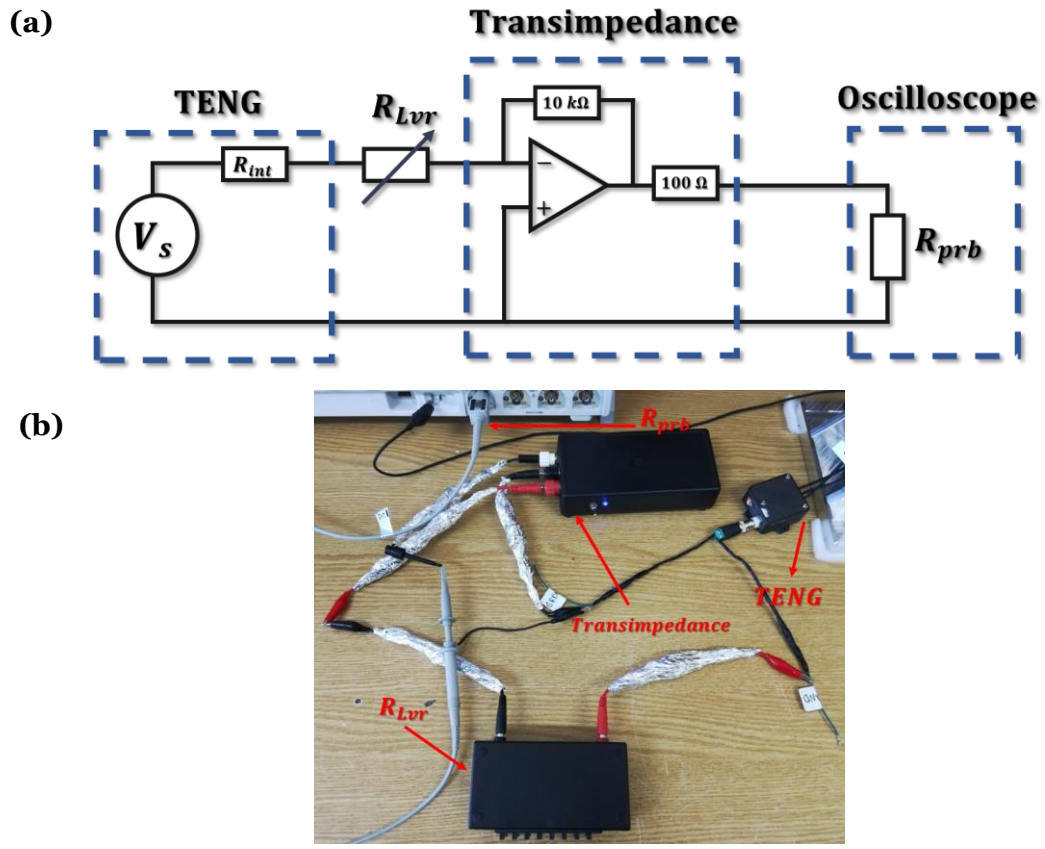

Figure 7.11 (a) Short Circuit Current Circuit diagram using transimpedance and (b) Short Circuit Current Measurement's wiring.

The transimpedance circuit is then activated and measurements are made using the variable load resistance range from 0 up to 100 $M\Omega$ with a step 1 $M\Omega$ for the first 10 $M\Omega$ values and then with a step 10 $M\Omega$ up to the maximum of R_{Lvr} (100 $M\Omega$). The hands-on wiring is shown in Figure 7.11 (b) .

Then, the current is converted to voltage through the analogy that corresponds to wiring of transimpedance circuit. Using the method given in Figure 7.11, the TENG's output voltage of open circuit was calculated with sensitivity 10 $mV/\mu A$.

According to Mallimeni [62] the performance of the use of transimpedance box is similar to that of the expensive SR570 instrumentation as shown in Figure 7.12 that is presently in use within the TENG community. As demonstrated in this study, the transimpedance circuit as shown in Figure 7.11 is a simple and cost-effective precision current preamplifier for measuring low-amplitude, dynamic current signals generated by TENGs.

Figure 7.12 Schematic illustration to measure electrical currents generated by TENG device using SR570.

This study was confirmed experimentally, and data calculated with sensitivity 1000 $mV/\mu A$. However, the final short current measurements were performed using the system appeared in Figure 7.11 .

7.2.7 Estimation of Maximum Power Output

For the estimation of the power as a function of an external load as well as the Open Circuit Voltage the methodology developed by Jayasvasti et al. [13] was applied.

Let's consider that P_L is the electrical power across the load resistance and R_L is the load resistance. Their dependence on each other is expressed by equation (7.7) . The load current value is calculated from the voltage generated by TENG across the load resistance ($R_{int}, R_{Lvr}, R_{Ldiv}, and\ R_{prb}$), which is based on Kirchhoff's law, as shown in equation (7.4). The key voltage-divider resistor R_{Ldiv} value is considered in equation (7.8), based on the application of Kirchhoff's law to the configuration of our technique,

$$\mathrm{P}_L = i^2 x\, R_L \qquad (7.3)$$

$$P_L = \left(\frac{V_s}{(R_{int} + (R_{Lvr} + (R_{Ldiv} // R_{prb}))}\right)^2 x\, (R_{Lvr} + (R_{Ldiv} // R_{prb}) \qquad (7.4)$$

If we consider the TENG voltage is V_{out}, the estimated electrical output power by the TENG energy harvester is described from the equation:

$$\mathrm{P_L} = \frac{V_{out}^2}{R_L} \qquad (7.5)$$

$$P_L = \frac{V_{out}^2}{(R_{Lvr} + (R_{Ldiv} // R_{prb}))} \qquad (7.6)$$

The data was obtained from LabView and the analysis using Origin and Python.

7.3 Electrical Characterization of Tribogenerators

To investigate the output performance of PLA-based TENGs four different types of measurements were performed: a) time-dependent output voltage (transient), b) capacitor charging and c) Open Circuit Voltage (V_{oc}) and d) short circuit current (I_{sc}).

For the transient measurements an InfiniiVision DSO7104A oscilloscope (Agilent Technologies) was used while for the capacitor charging ($C = 0.47\mu F$) measurement a full, quad bridge rectifier circuit with was used. The capacitor voltage was monitored by a Keithley 617 electrometer.

Figure 7.13 shows the triboelectric signal as a function of time for the various TENGs doped with SiC. We notice that initially the triboelectric signal increases from $11.3V$ for pristine PLA to $14.4V$ for PLA doped with $1.5wt\%$ SiC. However, as the SiC concentration increases to $3wt\%$ the triboelectric signal is reduced to $10.5V$, which is comparable to the value obtained for the undoped PLA.

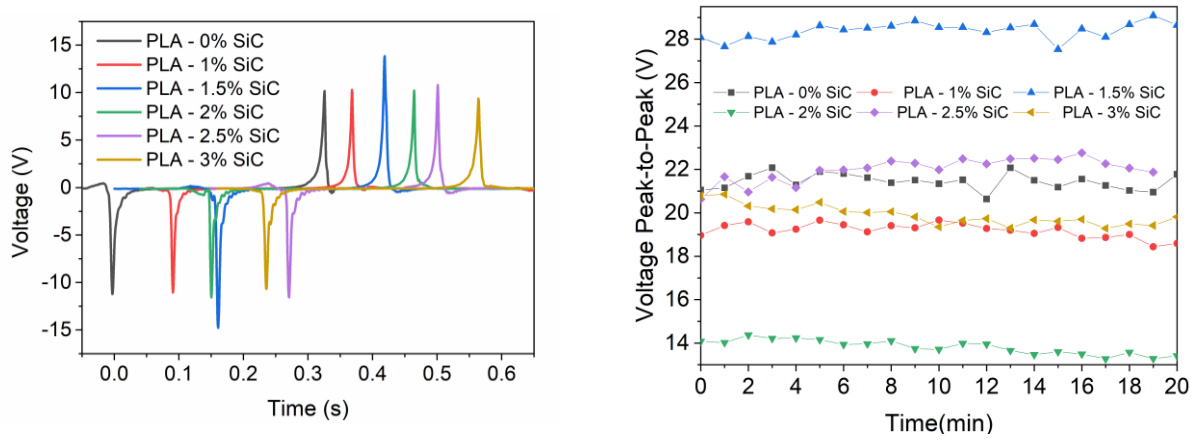

(a) **(b)**

Figure 7.13 Time-dependent triboelectric (a) instant voltage signal and (b) Voltage peak to peak for tribogenerators with different SiC concentrations.

Figure 7.14 shows the triboelectric signal as a function of time for the various TENGs doped with ZnO. We notice that the triboelectric signal increases as the concentration of ZnO increases reaching a value of $40V$ when the concentration of ZnO is $3wt\%$.

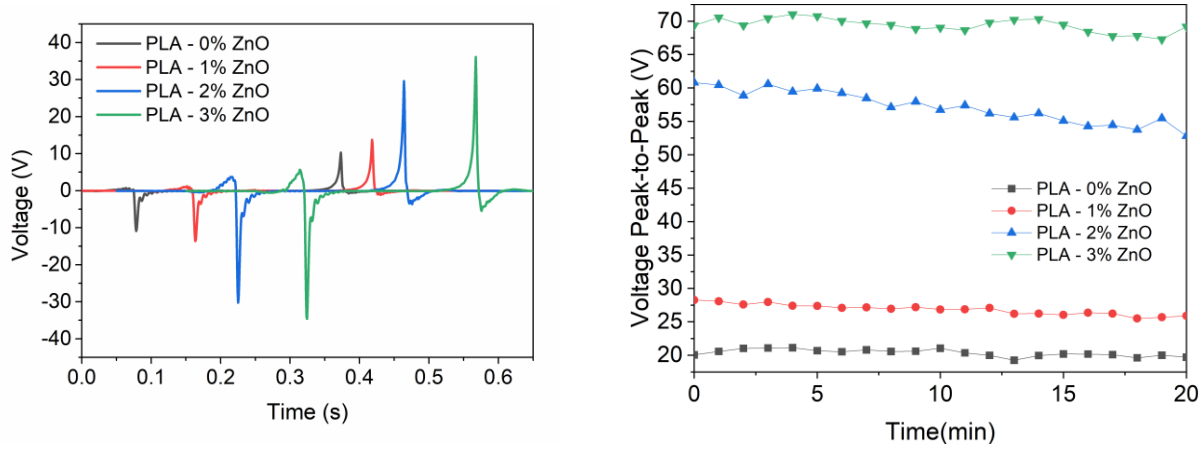

(a) **(b)**

Figure 7.14 Time-dependent triboelectric (a) instant voltage signal and (b) Voltage peak to peak for tribogenerators with different ZnO concentrations.

The results from the previous chapter are confirmed by the capacitor charging experiments. Figure 7.15 shows the capacitor voltage as a function of time for SiC-doped PLA and Figure 7.16 for ZnO-doped PLA TENGs.

For SiC-doped PLA it is noticed that the maximum capacitor charging is achieved for TENG with 1.5% SiC with charging Voltage at 15.35 *Volts*. Also, it is observed that the charging voltage is stabilized after approximately 5 *minutes* of tapping.

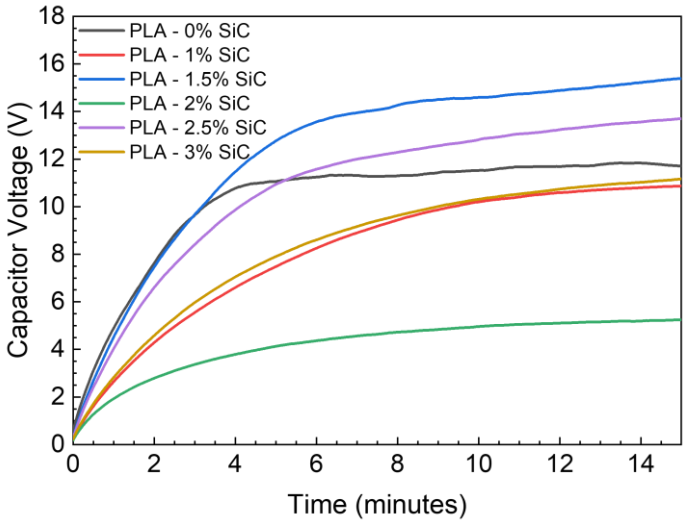

Figure 7.15 Capacitor voltage as a function for tribogenerators with different SiC concentration.

For ZnO-doped PLA it is noticed that the maximum capacitor charging is achieved for TENG with 3% ZnO with charging Voltage at 45.85 *Volts*. It has been shown that the charging voltage increases as ZnO content in PLA increases. Also, it is observed that the charging voltage is stabilized after approximately 5 *minutes* of tapping.

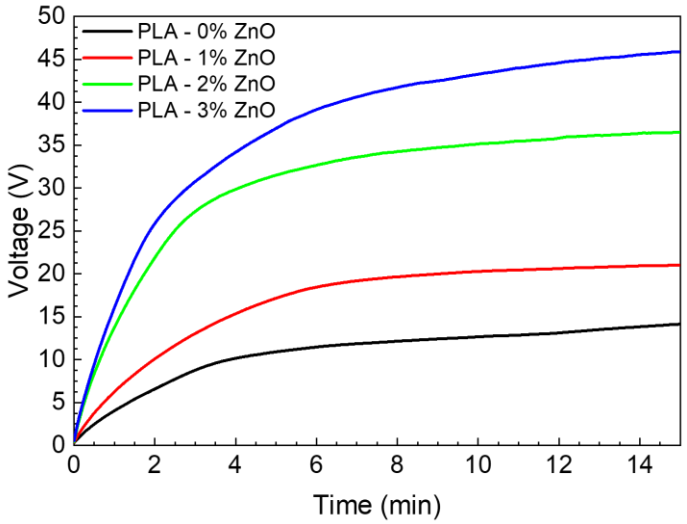

Figure 7.16 Capacitor voltage as a function for tribogenerators with different ZnO concentration.

Figure 7.17 shows the voltage output of SiC-doped PLA as a function of the external load. We notice that the 1.5wt% doped SiC exhibits the highest open circuit voltage reaching a value of 26V.

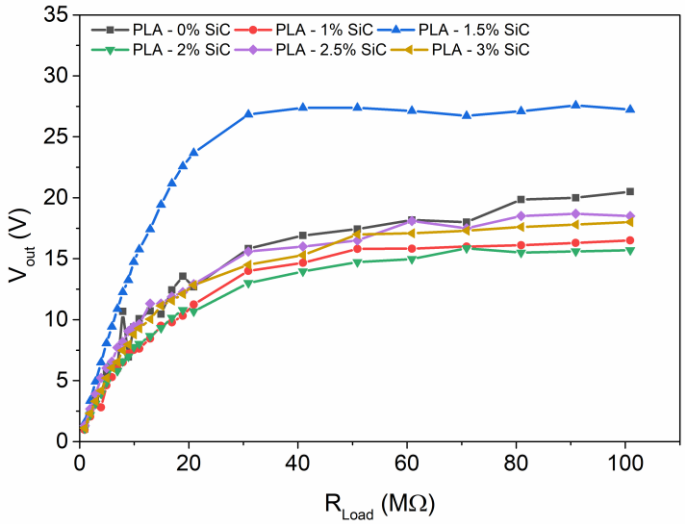

Figure 7.17 Open Circuit Voltage (Voc) for tribogenerators with different SiC concentration.

Figure 7.18 shows the voltage output as a function of the external load. We notice that the 3wt% doped ZnO exhibits the highest open circuit voltage reaching a value of 50V.

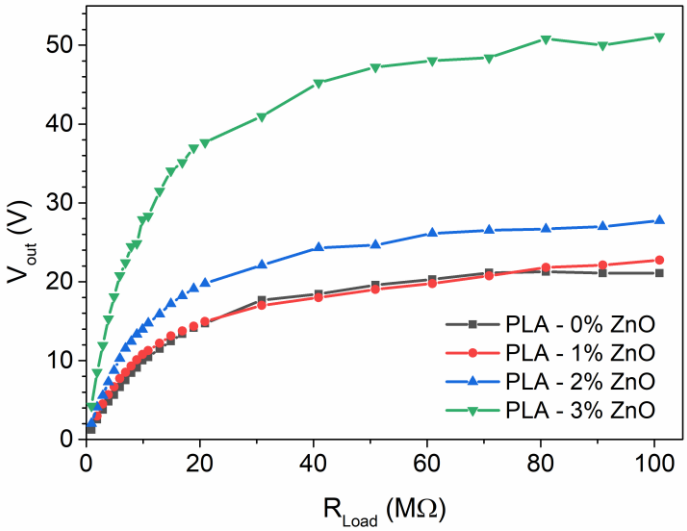

Figure 7.18 Open Circuit Voltage (Voc) for tribogenerators with different ZnO concentration.

Similar conclusion for SiC composites can be obtained from Figure 7.19, where the tribogenerator current is shown a function of the external load. We observe that the short circuit current (at zero external load) for the 1.5wt% SiC doped PLA reaches 2μA (500nA/cm^2), which is higher compared to all other samples.

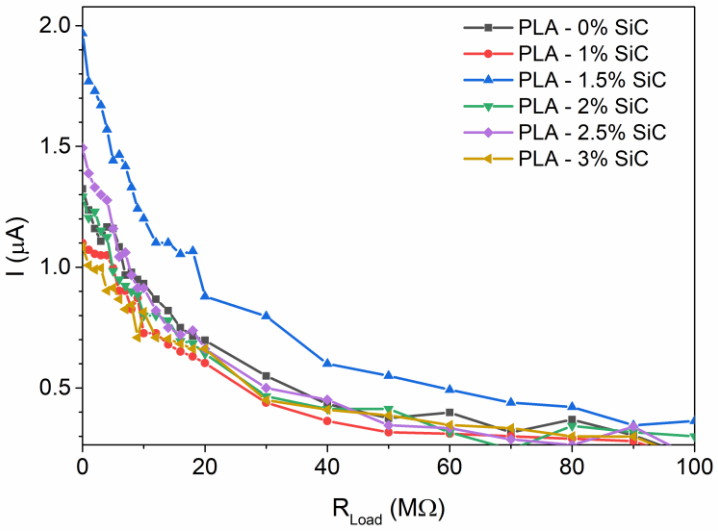

Figure 7.19 Short Circuit Current (Isc) for tribogenerators with different SiC concentration.

Similar results to the chapter 7.2.5 can be obtained from Figure 7.20, where the tribogenerator current is shown as a function of the external load. We notice that the short circuit current for the $3wt\%$ ZnO doped PLA reaches $2.2\mu A$ ($550nA/cm^2$), which is higher compared to all other samples.

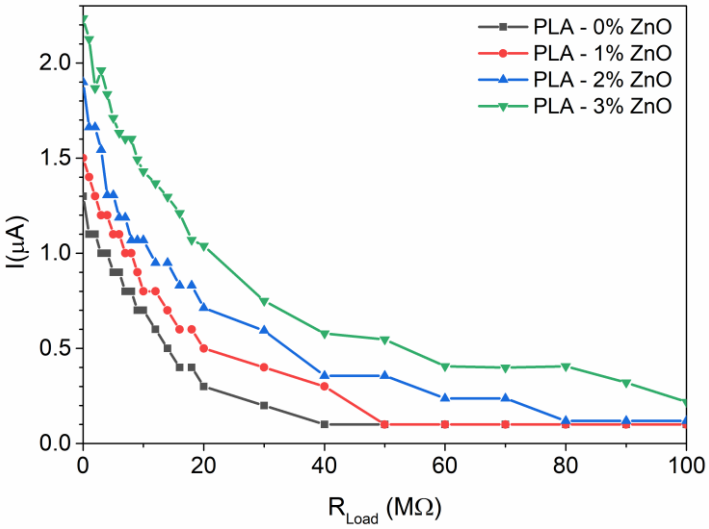

Figure 7.20 Short Circuit Current (Isc) for tribogenerators with different ZnO concentration.

Similar results for SiC composites can be extracted from Figure 7.21 where the dependence of the generated power is shown as a function of the external load. We notice that the maximum power obtained for the 1.5wt% SiC doped PLA is $26\mu W$ ($6.5\mu W/cm^2$), considering that the surface area of the samples is $4cm^2$), which presents 2.5 times increase compared to all other samples.

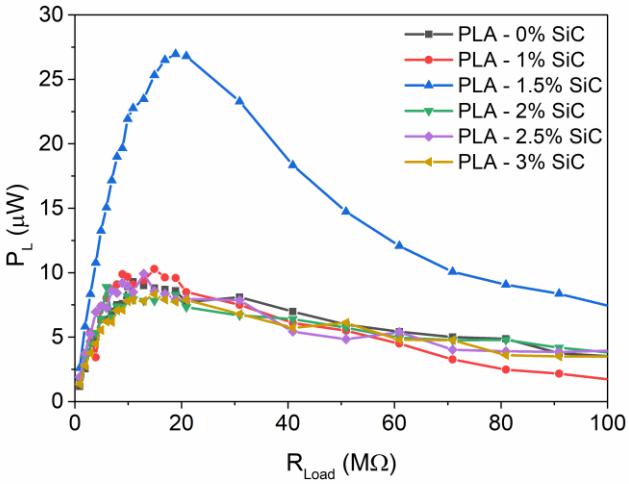

Figure 7.21 Power as a function of the external load for tribogenerators with different SiC concentrations.

For ZnO composites, similar results can be extracted from Figure 7.22 where the dependence of tribogenerator power is shown as a function of the external load. We notice that the maximum power obtained for the $3wt\%$ ZnO doped PLA is $80\mu W$ $(20\mu W/cm^2)$, which is about 8 times higher compared to the undoped PLA.

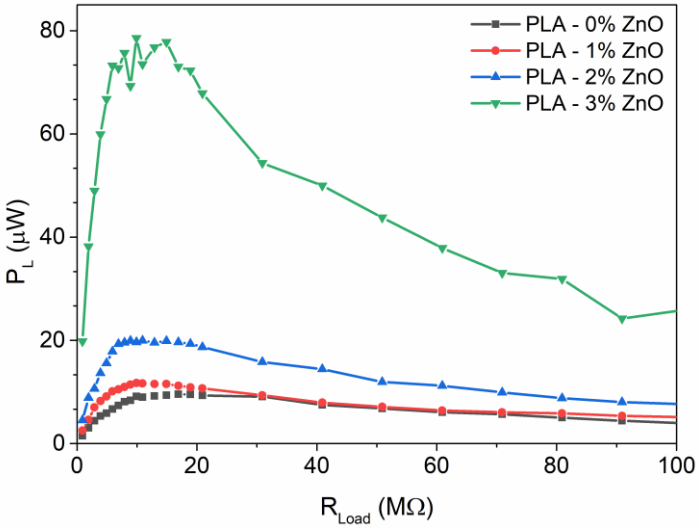

Figure 7.22 Power as a function of the external load for tribogenerators with different ZnO concentration.

7.4 Analysis & Discussion of the Results

To better understand the results, we refer to the theoretical analysis of Niu et al. [14]. Figure 7.23 shows a schematic of a tribogenerator composed of two dielectric surfaces and the electrodes attached at the back side of the dielectrics. The TENG operates in the contact-separation mode. When the two triboelectric surfaces are in contact electric charges of opposite polarities appear on the surfaces of the dielectrics, due to charge transfer between the two materials. In our case the surface of PLA is charged positive where the surface of Kapton is charged negatively, due to the differences in the electronegativities of the two materials.

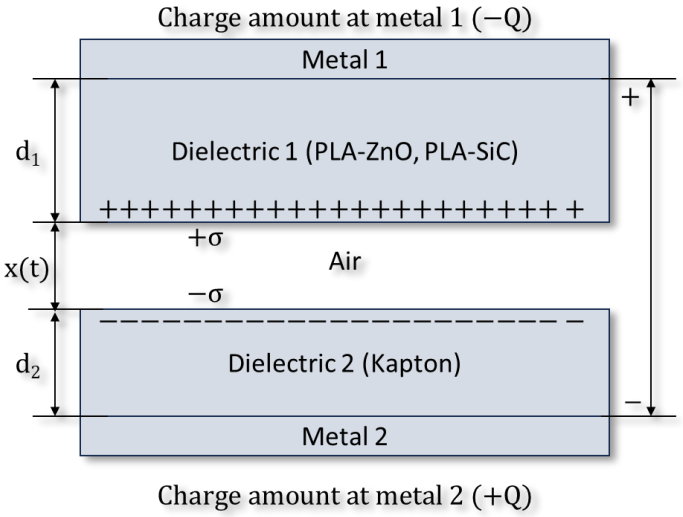

Figure 7.23 Schematic of the triboelectric generator in contact-separation mode.

The voltage that develops across the device is given by the V-Q-x relationship:

$$V(t) = -\frac{Q}{S\varepsilon_0}[d_0 + x(t)] + \frac{\sigma x(t)}{\varepsilon_0} \qquad (7.7)$$

where Q is the amount of charge at the metal contact, σ is the surface charge density on the surface of the dielectrics, ε_0 is the permittivity of vacuum, S is the contact area between the triboelectric pair and d_0 is given by the equation:

$$d_0 = \frac{d_1}{\varepsilon_{r1}} + \frac{d_2}{\varepsilon_{r2}} \qquad (7.8)$$

where d_1, d_2 and $\varepsilon_{r1}, \varepsilon_{r2}$ are the thicknesses and relative dielectric constants of the dielectric layers 1 and 2 respectively. In our case where Kapton® is used as the reference electrode and composite PLA is used as the active electrode the values are: $d_1 = 75\mu m, \varepsilon_{r1} = 3, d_2 = 390\mu m$. The value for ε_{r2} depends on the composite doping.

Alternatively, equation (7.7) can be written in the form:

$$V(t) = -\frac{Q}{C_{TENG}} + V_{oc} \qquad (7.9)$$

where CTENG is the total capacitance of the TENG given by the equation (7.10)

$$C_{TENG} = \frac{S\varepsilon_0}{[d_0 + x(t)]} \qquad (7.10)$$

and V_{oc} is the open circuit voltage as defined in equation (7.11)

$$V_{oc} = \frac{\sigma \cdot x(t)}{\varepsilon_o} \qquad (7.11)$$

Figure 7.25 (a) shows a comparison of the open circuit voltage V_{oc} and the short circuit current Isc of the TENGs with the various concentrations of SiC and ZnO. We see that as the concentration of SiC and ZnO increases Voc and Isc are enhanced in both cases. In fact, for the SiC-doped PLA, V_{oc} and I_{sc} are increased by 42% and 48% respectively compared to undoped PLA as the concentration

increases to 1.5wt%, while for ZnO-doped PLA the increase is 44% and 69% respectively as the concentration increases to 2%. Similar behavior is observed for the maximum power with the increase being 280% and 188% respectively.

Such a behavior can be attributed to the improvement of the capacitance/dielectric constant of doped-PLA due to the introduction of fillers (micro/nanoparticles) with higher dielectric constant compared to the PLA [15]. It has been demonstrated that the inclusion of fillers within a dielectric can enhance the triboelectric signal. This is because nanoparticles with higher dielectric constant compared to the host, when dispersed in the matrix, will act as microcapacitors. Upon the presence of an electric field, charge will accumulate at the interface of the particles, leading to interfacial polarization and an enhancement of the surface charge density of the dielectric layer [16] as shown in Figure 7.24.

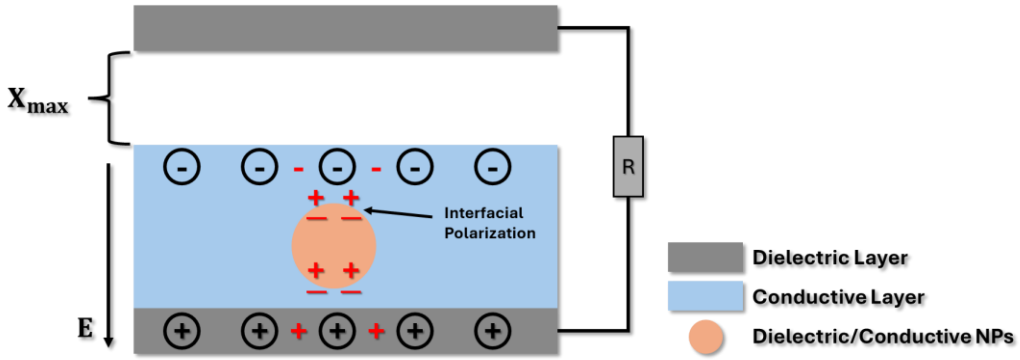

Figure 7.24 Schematic diagram of internal interface polarization in TENG dielectric layer thin films doped with dielectric/conductive nanoparticles, inspired from [16].

Moreover, the presence of these particles will increase the dielectric properties of the composite material. It has been shown theoretically that the inclusion of particles with higher dielectric constant than the host matrix, will increase the dielectric constant, regardless of the shape of the particles [17]. The reported values for the dielectric constant of PLA range from 2.5 to 3.11 [7], [8], which is much lower compared to the dielectric constant of SiC which is almost 15 in its powder form [9] and for ZnO nanoparticles which is about 10 [18]. From chapter 6.2.2 we have demonstrated that the inclusion of SiC particles monotonically increases the dielectric constant of the composite material reaching a value of 3.9 for the 3wt% SiC doped PLA. Similar results are expected for ZnO doped PLA. This increase in the dielectric constant significantly increased the density of the charges that can be accumulated on the copolymer during physical contact [19]. From Figure 7.25 (a) and considering equation (7.10) we can conclude that the surface charge density for the 1.5wt% SiC-doped samples and the 3wt% ZnO-doped samples is increased compared to the undoped PLA reaching a value of 2.65$\mu C/m^2$ and 4.86$\mu C/m^2$ respectively.

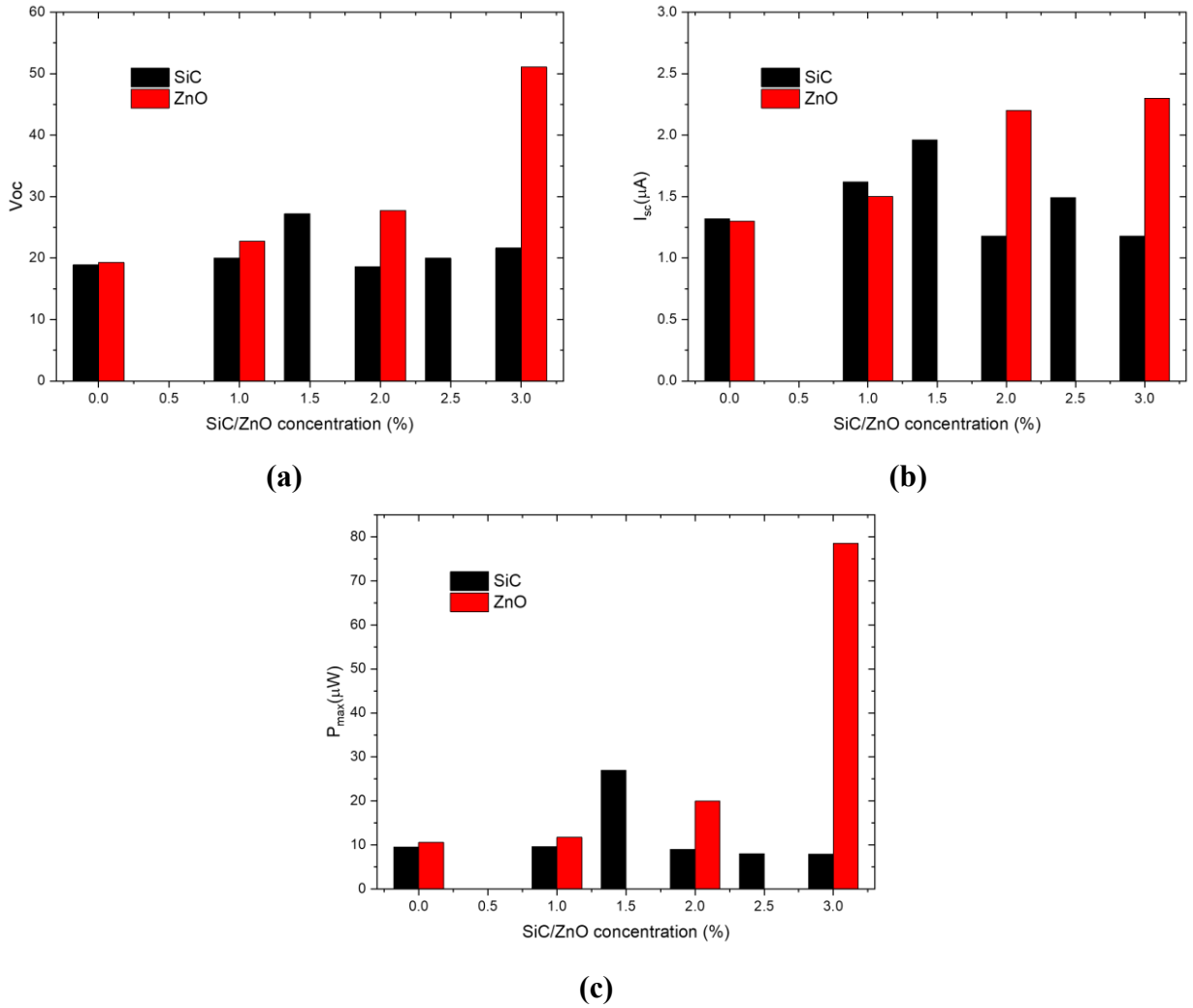

Figure 7.25 (a) Open circuit voltage and (b) Short Circuit current and (c) power of the TENGs with the various concentrations of SiC and ZnO.

Another point that we notice from Figure 7.25 is the different behavior between the PLA-doped materials. We observe that for the ZnO-doped samples the triboelectric signal continues to increase as the concentration increases to 3*wt*%. In fact, the open circuit voltage, short circuit current and power output are increased by 265%, 177% and 741% respectively, compared to the undoped PLA.

However, the SiC-doped PLA behaves in a different way. The triboelectric signal reaches a maximum (at 1.5*wt*% in our case) and then it is reduced as the concentration is increased to 3*wt*%. To better comprehend this behavior, we take the mechanisms that influence the triboelectric signal into consideration. For the doped PLA samples, there are two competing mechanisms that determine the triboelectric signal: (a) the doping with the SiC to ZnO particles, which lead to an increase in the triboelectric signal due to increased dielectric constant/capacitance of the doped PLA samples, as we have analyzed above; and (b) an increase in surface roughness, which leads to a decrease in the triboelectric signal due to the reduction in the active contact area between the two triboelectric surfaces. As we have mentioned, during preparation the samples were polished with a SiC polishing paper to reduce the surface roughness of the 3D printed surface. This results in a relatively low value of surface roughness. From optical profiler measurements, we estimate the root mean square height

is less than 0.3 μm. However, as the concentration of SiC in the PLA matrix to increases 3wt%, the surface roughness increases by 33%, reaching a value of 0.41 μm. This results in a reduction in the surface contact area leading to a decrease in the triboelectric signal. In contrast, for the ZnO-doped PLA, optical profiler measurements indicate that the incorporation of ZnO particles in the PLA does not influence the surface roughness. This can be attributed to the smaller size of ZnO nanoparticles as well as the fact that ZnO is much softer compared to the SiC grinding paper.

The reduction in the triboelectric signal due to the increased surface roughness agrees with literature results. Kumar et al. [20] investigated the impact of random multiscale surface roughness on the triboelectric signal of TENGs. These researchers developed TENGs based on transparent mica in contact with polyvinyl siloxane (PVS) with modulated surface roughness. With the aid of a novel in situ optical technique, they were able to directly estimate the contact surface area as a function of the roughness. They observed that, as the roughness increased, the triboelectric signal as well as the output performance of the TENG did as well, due to the decrease in the real contact area. Similar results were obtained from Wen et al. [21] who investigated, both theoretically and experimentally, a conductor–dielectric contact separation TENG for sensing the roughness of material surfaces. The reduction in the triboelectric signal for PVDF-doped SiC has also been reported in the literature by Shafeek et al. [22]. Those researchers investigated the influence of SiC nanoparticles on the triboelectric properties of a polyvinylidene fluoride (PVDF)/silicon carbide (SiC) nanocomposite. They showed that the triboelectric signal can be greatly enhanced compared to pristine PVDF as the concentration of SiC increased up to 6%. However, for higher concentrations (9%) the device output tends to decrease. They attributed this decrease to the agglomeration of SiC nanoparticles on the surface of the PVDF films resulting in reduced contact area between the PVDF and the polyamide that was used as a reference material.

7.5 Data Analysis using Python

The data analysis of all kinds of measurement was implemented with Python 3.9.13 in the programming environment Visual Studio Code. During this thesis, it was necessary to create User Interfaces (UIs) to directly make the analysis from LabView measurements to final data. The repository that includes all the scripts for UIs and analysis of the results are located on GitHub:

- GitHub Profile: stefaniaskorda (Stefania Skorda)
- Link to thesis' repository: https://github.com/stefaniaskorda/Diploma-Thesis-PLA-based-Tribogenerators

The goal of these scripts was to handle the thousands of lvm/csv files from each kind of measurement.

8 Conclusions and Future Perspectives

In this thesis, we have explored the effects of incorporating micron-sized SiC particles and nano-sized ZnO particles into PLA composites, examining their impact on mechanical, electrical, and triboelectric properties.

Our findings reveal that SiC particles can significantly improve the mechanical strength and dielectric constant of PLA composites at optimal concentrations. Specifically, a 1.5wt% SiC concentration in PLA enhances the triboelectric output power by 284% compared to pure PLA. However, increasing SiC content to 3wt% diminishes these gains, aligning with similar observations in PVDF composites doped with silicon carbide nanoparticles, likely due to reduced contact area between triboelectric surfaces. Conversely, the addition of ZnO particles to PLA composites has a diminishing effect on mechanical properties, with both tensile strength and hertzian compression load decreasing as ZnO content increases. Despite this, the triboelectric performance of PLA-ZnO composites improves with higher ZnO concentrations, culminating in a remarkable 741% increase in output power at a 3wt% ZnO concentration.

These contrasting outcomes underscore the nuanced role that filler concentration plays in the multifaceted performance of PLA composites. The strategic selection of SiC and ZnO concentrations can tailor the balance between mechanical robustness and triboelectric efficiency, offering valuable insights for the development of advanced materials in applications where specific property enhancements are desired.

However, the long-term performance of PLA-based TENGs is a concern, as the aging of PLA could potentially degrade its triboelectric performance. It was observed from our experiments that a PLA-based sample's triboelectric performance was declining over time. Physical aging in PLA is primarily attributed to the rearrangement of polymer chains towards a more thermodynamically stable state. This process is influenced by factors such as temperature and humidity and can lead to changes in the material's mechanical and electrical properties. The glass transition temperature (Tg) of PLA is a critical parameter, as aging processes accelerate at temperatures near Tg. Another significant aspect of PLA aging is the formation of nanopores within the polymer matrix. These structural changes, possibly resulting from the loss of volatile components or environmental stress, can adversely affect the material's triboelectric performance by altering its ability to generate and maintain triboelectric charges. The aging of PLA can lead to a decrease in the triboelectric output of TENGs. This reduction in performance is partly due to changes in the crystallinity and mechanical properties of PLA as it ages. Studies have indicated that the triboelectric output is correlated with the material's crystallinity, suggesting that aging-induced alterations in crystallinity could diminish the efficiency of PLA-based TENGs.

Further investigations are necessary to fully understand the long-term effects of aging on PLA-based TENGs under real-world conditions. The development of new composite materials and the exploration of alternative biodegradable polymers with enhanced aging resistance could pave the way for the next generation of sustainable and reliable TENGs. Additionally, advanced characterization techniques for monitoring the aging process in situ will provide valuable insights into the material's behavior over time, facilitating the design of more durable and efficient TENGs.

One other of the key areas for future research include the investigating tribogenerators with novel structural designs, such as incorporating additional surfaces or non-linear, curved surfaces, could significantly enhance energy output. This exploration could lead to breakthroughs in maximizing the efficiency of mechanical-to-electrical energy conversion. Transitioning from simple passive circuits to sophisticated active systems and integrated energy management solutions can substantially improve the efficiency of converting harvested energy into usable power for external loads. This advancement is pivotal for developing self-sustaining systems that ensure maximum reliability, especially during periods of ambient energy scarcity. While some solutions have transitioned into commercial products, there remains a vast potential for tribogenerators in various sectors, including wearable electronics, smart textiles, and renewable energy harvesting. Future research should focus on bridging the gap between laboratory prototypes and commercial applications, addressing challenges related to scalability, durability, and integration with existing technologies.

The exploration of tribogenerator technology, as discussed in this thesis, is crucial for advancing renewable energy solutions. The simplicity and cost-effectiveness of constructing tribogenerators, coupled with versatile energy management and storage solutions, lay a solid foundation for further innovation.

Journal Publications

1. **Skorda, S.**; Bardakas, A.; Segkos, A.; Chouchoumi, N.; Hourdakis, E.; Vekinis, G.; Tsamis, C. Influence of SiC doping on the mechanical, electrical, and optical properties of 3D-printed PLA. J. Compos. Sci. 2024, 8, 79. https://doi.org/10.3390/jcs8030079. [63]

2. **Skorda, S.**; Bardakas, A.; Vekinis, G.; Tsamis, C. Influence of SiC and ZnO Doping on the Electrical Performance of Polylactic Acid-Based Triboelectric Nanogenerators. Sensors 2024, 24, 2497. https://doi.org/10.3390/s24082497.[64]

Bibliography

[1] Z. L. Wang, L. Lin, J. Chen, S. Niu, and Y. Zi, *Triboelectric Nanogenerators*. Cham: Springer International Publishing, 2016. doi: 10.1007/978-3-319-40039-6.

[2] W. G. Kim, D. W. Kim, I. W. Tcho, J. K. Kim, M. S. Kim, and Y. K. Choi, "Triboelectric Nanogenerator: Structure, Mechanism, and Applications," *ACS Nano*, vol. 15, no. 1, pp. 258–287, Jan. 2021, doi: 10.1021/ACSNANO.0C09803/ASSET/IMAGES/MEDIUM/NN0C09803_0020.GIF.

[3] Y. Yu *et al.*, "Material's selection rules for high performance triboelectric nanogenerators," *Materials Today*, vol. 64, pp. 61–71, Apr. 2023, doi: 10.1016/J.MATTOD.2023.03.008.

[4] E. Delgado-Alvarado *et al.*, "Recent Progress of Nanogenerators for Green Energy Harvesting: Performance, Applications, and Challenges," *Nanomaterials*, vol. 12, no. 15, Aug. 2022, doi: 10.3390/NANO12152549.

[5] K. Kanishka and B. Acherjee, "Revolutionizing manufacturing: A comprehensive overview of additive manufacturing processes, materials, developments, and challenges," *J Manuf Process*, vol. 107, pp. 574–619, Dec. 2023, doi: 10.1016/J.JMAPRO.2023.10.024.

[6] B. Chen, W. Tang, and Z. L. Wang, "Advanced 3D printing-based triboelectric nanogenerator for mechanical energy harvesting and self-powered sensing," *Materials Today*, vol. 50, pp. 224–238, Nov. 2021, doi: 10.1016/J.MATTOD.2021.05.017.

[7] R. Colella, F. P. Chietera, and L. Catarinucci, "Analysis of FDM and DLP 3D-Printing Technologies to Prototype Electromagnetic Devices for RFID Applications," *Sensors 2021, Vol. 21, Page 897*, vol. 21, no. 3, p. 897, Jan. 2021, doi: 10.3390/S21030897.

[8] B. Behzadnezhad, B. D. Collick, N. Behdad, and A. B. Mcmillan, "Dielectric properties of 3D-printed materials for anatomy specific 3D-printed MRI coils," 2018, doi: 10.1016/j.jmr.2018.02.013.

[9] H.-J. Yang *et al.*, "Silicon carbide powders: Temperature-dependent dielectric properties and enhanced microwave absorption at gigahertz range," 2013, doi: 10.1016/j.ssc.2013.03.004.

[10] B. Sareni *et al.*, "Effective dielectric constant of periodic composite materials," *Cite as: Journal of Applied Physics*, vol. 80, no. 3, p. 1688, 1996, doi: 10.1063/1.362969ï.

[11] R. Guo, Z. Ren, H. Bi, Y. Song, and M. Xu, "Effect of toughening agents on the properties of poplar wood flour/poly (lactic acid) composites fabricated with Fused Deposition Modeling," 2018, doi: 10.1016/j.eurpolymj.2018.07.035.

[12] D. Froš and I. Králová, “Conductive FDM Filament: Electrical Resistivity Assessment and Sensor Applications,” *Proceedings of the International Spring Seminar on Electronics Technology*, vol. 2023-May, 2023, doi: 10.1109/ISSE57496.2023.10168513.

[13] S. Jayasvasti, P. Thainiramit, P. Yingyong, and D. Isarakorn, “Technique for Measuring Power across High Resistive Load of Triboelectric Energy Harvester,” *Micromachines 2021, Vol. 12, Page 766*, vol. 12, no. 7, p. 766, Jun. 2021, doi: 10.3390/MI12070766.

[14] S. Niu *et al.*, “Theoretical study of contact-mode triboelectric nanogenerators as an effective power source †”, doi: 10.1039/c3ee42571a.

[15] L. Jin *et al.*, “Manipulating Relative Permittivity for High-Performance Wearable Triboelectric Nanogenerators,” *Nano Lett*, vol. 20, no. 9, pp. 6404–6411, Sep. 2020, doi: 10.1021/ACS.NANOLETT.0C01987.

[16] X. Suo *et al.*, “Dielectric layer doping for enhanced triboelectric nanogenerators,” 2023, doi: 10.1016/j.nanoen.2023.108651.

[17] B. Sareni *et al.*, “Effective dielectric constant of periodic composite materials,” *Cite as: Journal of Applied Physics*, vol. 80, no. 3, p. 1688, 1996, doi: 10.1063/1.362969ï.

[18] D. Kaur, A. Bharti, T. Sharma, and C. Madhu, “Dielectric Properties of ZnO-Based Nanocomposites and Their Potential Applications,” 2021, doi: 10.1155/2021/9950202.

[19] J. W. Lee *et al.*, “Robust nanogenerators based on graft copolymers via control of dielectrics for remarkable output power enhancement,” *Sci Adv*, vol. 3, no. 5, May 2017, doi: 10.1126/SCIADV.1602902/SUPPL_FILE/1602902_SM.PDF.

[20] C. Kumar *et al.*, “Multiscale in-situ quantification of the role of surface roughness and contact area using a novel Mica-PVS triboelectric nanogenerator,” *Nano Energy*, vol. 107, p. 108122, Mar. 2023, doi: 10.1016/J.NANOEN.2022.108122.

[21] J. Wen, H. He, C. Niu, M. Rong, Y. Huang, and Y. Wu, “An improved equivalent capacitance model of the triboelectric nanogenerator incorporating its surface roughness,” *Nano Energy*, vol. 96, p. 107070, Jun. 2022, doi: 10.1016/J.NANOEN.2022.107070.

[22] S. Shafeek *et al.*, “Exalting energy scavenging for triboelectric nanogenerator using silicon carbide particles doped polyvinylidene difluoride nanocomposite,” *Nano Energy*, vol. 107, p. 108146, 2023, doi: 10.1016/j.nanoen.2022.108146.

[23] “Renewable Energy Market Size to Hit USD 2182.99 Billion by 2032.” Accessed: Mar. 17, 2024. [Online]. Available: https://www.precedenceresearch.com/renewable-energy-market

[24] H. ; Zeb *et al.*, “Zero Energy IoT Devices in Smart Cities Using RF Energy Harvesting,” *Electronics 2023, Vol. 12, Page 148*, vol. 12, no. 1, p. 148, Dec. 2022, doi: 10.3390/ELECTRONICS12010148.

[25] A. Eunice Akin-Ponnle, N. Borges Carvalho, A. Poniszewska-Maranda, and W. Maranda, "Energy Harvesting Mechanisms in a Smart City—A Review," *Smart Cities 2021, Vol. 4, Pages 476-498*, vol. 4, no. 2, pp. 476–498, Apr. 2021, doi: 10.3390/SMARTCITIES4020025.

[26] R. Salama and F. Al-Turjman, "Sustainable Energy Production in Smart Cities," *Sustainability 2023, Vol. 15, Page 16052*, vol. 15, no. 22, p. 16052, Nov. 2023, doi: 10.3390/SU152216052.

[27] C. Zhang *et al.*, "Evolution of Micro-Nano Energy Harvesting Technology—Scavenging Energy from Diverse Sources towards Self-Sustained Micro/Nano Systems," *Nanoenergy Advances 2023, Vol. 3, Pages 101-125*, vol. 3, no. 2, pp. 101–125, Apr. 2023, doi: 10.3390/NANOENERGYADV3020006.

[28] R. Caliò *et al.*, "Piezoelectric Energy Harvesting Solutions," *Sensors 2014, Vol. 14, Pages 4755-4790*, vol. 14, no. 3, pp. 4755–4790, Mar. 2014, doi: 10.3390/S140304755.

[29] Khushboo and P. Azad, "Triboelectric nanogenerator based on vertical contact separation mode for energy harvesting," *Proceeding - IEEE International Conference on Computing, Communication and Automation, ICCCA 2017*, vol. 2017-January, pp. 1499–1502, Dec. 2017, doi: 10.1109/CCAA.2017.8230037.

[30] G. Zhu *et al.*, "Triboelectric-generator-driven pulse electrodeposition for micropatterning," *Nano Lett*, vol. 12, no. 9, pp. 4960–4965, Sep. 2012, doi: 10.1021/NL302560K/SUPPL_FILE/NL302560K_SI_001.PDF.

[31] Z. L. Wang, J. Chen, and L. Lin, "Progress in triboelectric nanogenerators as a new energy technology and self-powered sensors," *Energy Environ Sci*, vol. 8, no. 8, pp. 2250–2282, 2015, doi: 10.1039/C5EE01532D.

[32] H. Ryu *et al.*, "Self-rechargeable cardiac pacemaker system with triboelectric nanogenerators," *Nature Communications 2021 12:1*, vol. 12, no. 1, pp. 1–9, Jul. 2021, doi: 10.1038/s41467-021-24417-w.

[33] J. P. Lee *et al.*, "Encoding of multi-modal emotional information via personalized skin-integrated wireless facial interface," *Nature Communications 2024 15:1*, vol. 15, no. 1, pp. 1–13, Jan. 2024, doi: 10.1038/s41467-023-44673-2.

[34] S. Gao *et al.*, "Self-powered system by a suspension structure-based triboelectric-electromagnetic-piezoelectric hybrid generator for unifying wind energy and vibration harvesting with vibration attenuation function," *Nano Energy*, vol. 122, p. 109323, 2024, doi: 10.1016/j.nanoen.2024.109323.

[35] Y. Gao, Y. Zhang, L.-B. Huang, X. Hua, and B. Dong, "Converting wave scouring damage into opportunities: Advancing marine structure protection through a wave-energy harvesting protective layer," *Nano Energy*, vol. 123, 2024, doi: 10.1016/j.nanoen.2024.109367.

[36] "PRODUCT DATA SHEET LUMINY ® L175 Product Data Sheet Luminy® L175," 2017, Accessed: Mar. 09, 2024. [Online]. Available: www.total-corbion.com

[37] S. Bergaliyeva, D. L. Sales, F. J. Delgado, S. Bolegenova, and S. I. Molina, "Manufacture and Characterization of Polylactic Acid Filaments Recycled from Real Waste for 3D Printing," *Polymers (Basel)*, vol. 15, no. 9, May 2023, doi: 10.3390/POLYM15092165.

[38] T. Muringayil Joseph *et al.*, "3D printing of polylactic acid: recent advances and opportunities," *The International Journal of Advanced Manufacturing Technology*, vol. 1, p. 3, doi: 10.1007/s00170-022-10795-y.

[39] S. Sömiya and Y. Inomata, "Silicon Carbide Ceramics—1," *Silicon Carbide Ceramics—1*, 1991, doi: 10.1007/978-94-011-3842-0.

[40] H. Abderrazak and E. S. B. Hadj Hmi, "Silicon Carbide: Synthesis and Properties," *Properties and Applications of Silicon Carbide*, Apr. 2011, doi: 10.5772/15736.

[41] S. Raha and M. Ahmaruzzaman, "ZnO nanostructured materials and their potential applications: progress, challenges and perspectives," *Nanoscale Adv*, vol. 4, no. 8, pp. 1868–1925, Apr. 2022, doi: 10.1039/D1NA00880C.

[42] "Tensile test on plastics ISO 527-1 | ISO 527-2 | ZwickRoell." Accessed: Feb. 21, 2024. [Online]. Available: https://www.zwickroell.com/industries/plastics/thermoplastics-and-thermosetting-molding-materials/tensile-test-iso-527-1-2/

[43] M. Abd Mutalib, M. A. Rahman, M. H. D. Othman, A. F. Ismail, and J. Jaafar, "Scanning Electron Microscopy (SEM) and Energy-Dispersive X-Ray (EDX) Spectroscopy," *Membrane Characterization*, pp. 161–179, Jan. 2017, doi: 10.1016/B978-0-444-63776-5.00009-7.

[44] "Sputter deposition - Wikipedia." Accessed: Feb. 14, 2024. [Online]. Available: https://en.wikipedia.org/wiki/Sputter_deposition

[45] "Sputter coating for SEM: how this sample preparation technique assists your imaging - GR", Accessed: Feb. 14, 2024. [Online]. Available: https://www.thermofisher.com/tr/en/home/global/forms/industrial/sputter-coating-sem.html

[46] "Surface Roughness Measurement—Parameters | Olympus." Accessed: Mar. 15, 2024. [Online]. Available: https://www.olympus-ims.com/en/metrology/surface-roughness-measurement-portal/parameters/

[47] "Root Mean Square Roughness - Michigan Metrology." Accessed: Mar. 15, 2024. [Online]. Available: https://michmet.com/glossary-term/root-mean-square-roughness/

[48] "Stress–strain curve - Wikipedia." Accessed: Feb. 21, 2024. [Online]. Available: https://en.wikipedia.org/wiki/Stress%E2%80%93strain_curve

[49] “Fatigue test - tec-science.” Accessed: Feb. 21, 2024. [Online]. Available: https://www.tec-science.com/material-science/material-testing/fatigue-test/

[50] H. J. Qi, K. Joyce, and M. C. Boyce, “DUROMETER HARDNESS AND THE STRESS-STRAIN BEHAVIOR OF ELASTOMERIC MATERIALS”, Accessed: Jan. 02, 2024. [Online]. Available: http://meridian.allenpress.com/rct/article-pdf/76/2/419/1945045/1_3547752.pdf

[51] “Standard Test Method for Rubber Property-Durometer Hardness 1”, doi: 10.1520/D2240-15.

[52] “Shore durometer - Wikipedia.” Accessed: Jan. 02, 2024. [Online]. Available: https://en.wikipedia.org/wiki/Shore_durometer

[53] “Shore D Hardness Test (Durometer Scale) - Hardness of Plastic Materials.” Accessed: Jan. 02, 2024. [Online]. Available: https://omnexus.specialchem.com/polymer-property/hardness-shore-d

[54] “ISO 48-4:2018 - Rubber, vulcanized or thermoplastic — Determination of hardness — Part 4: Indentation hardness by durometer method (Shore hardness).” Accessed: Jan. 02, 2024. [Online]. Available: https://www.iso.org/standard/74969.html

[55] ▶ Hemiarthroplasty and T. Imanishi, “Hertz Theory: Contact of Spherical Surfaces,” *Encyclopedia of Tribology*, pp. 1654–1662, 2013, doi: 10.1007/978-0-387-92897-5_492.

[56] X. Zhu, “Tutorial on Hertz Contact Stress,” 2012.

[57] K. L. Johnson and J. A. Greenwood, “An Adhesion Map for the Contact of Elastic Spheres,” *J Colloid Interface Sci*, vol. 192, no. 2, pp. 326–333, Aug. 1997, doi: 10.1006/JCIS.1997.4984.

[58] B. Taylor, “Tutorial-Hertz Contact Stress”.

[59] T. Jamnongkan *et al.*, “A Comprehensive Evaluation of Mechanical, Thermal, and Antibacterial Properties of PLA/ZnO Nanoflower Biocomposite Filaments for 3D Printing Application,” *Polymers 2022, Vol. 14, Page 600*, vol. 14, no. 3, p. 600, Feb. 2022, doi: 10.3390/POLYM14030600.

[60] W. Li, B. Leng, S. Hu, and X. Cheng, “Improving the Output Efficiency of Triboelectric Nanogenerator by a Power Regulation Circuit,” *Sensors*, vol. 23, no. 10, p. 4912, May 2023, doi: 10.3390/S23104912/S1.

[61] S. S. K. Mallineni, H. Behlow, R. Podila, and A. M. Rao, “A low-cost approach for measuring electrical load currents in triboelectric nanogenerators,” *Nanotechnol Rev*, vol. 7, no. 2, pp. 149–156, Apr. 2018, doi: 10.1515/NTREV-2017-0178/ASSET/GRAPHIC/J_NTREV-2017-0178_FIG_005.JPG.

[62] S. S. K. Mallineni, H. Behlow, R. Podila, and A. M. Rao, “A low-cost approach for measuring electrical load currents in triboelectric nanogenerators,” *Nanotechnol Rev*, vol. 7, no. 2, pp.

149–156, Apr. 2018, doi: 10.1515/NTREV-2017-0178/ASSET/GRAPHIC/J_NTREV-2017-0178_FIG_005.JPG.

[63] S. Skorda *et al.*, "Influence of SiC Doping on the Mechanical, Electrical, and Optical Properties of 3D-Printed PLA," *Journal of Composites Science 2024, Vol. 8, Page 79*, vol. 8, no. 3, p. 79, Feb. 2024, doi: 10.3390/JCS8030079.

[64] S. Skorda, A. Bardakas, G. Vekinis, and C. Tsamis, "Influence of SiC and ZnO Doping on the Electrical Performance of Polylactic Acid-Based Triboelectric Nanogenerators," *Sensors 2024, Vol. 24, Page 2497*, vol. 24, no. 8, p. 2497, Apr. 2024, doi: 10.3390/S24082497.